Doklady Physics, Vol. 46, No. 7, 2001, pp. 453–458. Translated from Doklady Akademii Nauk, Vol. 379, No. 1, 2001, pp. 33–37.
Original Russian Text Copyright © 2001 by Alexandrov.

PHYSICS

The Effect of Concentrational Supercooling on the Morphological Stability of Self-Similar Solidification with a Planar Front

D. V. Alexandrov

Presented by Academician N.A. Vatolin December 21, 2000

Received January 9, 2001

It is well known that a region of metastable supercooling, i.e., the zone of concentrational supercooling, can be formed if certain relationships exist between the thermal characteristics of a melt ahead of the crystallization front. Such a region modifies fundamentally the pattern of the solidification process. In front of a planar boundary between the pure solid and liquid phases, an intense growth of solid-phase elements can take place in the supercooling region, as well as a morphological growth of individual protrusions of the front due to perturbations that always exist in the system. The morphological instability of quasisteady solidification with a planar front was first analyzed in the classical study of V. Mullins and R. Sekerka [1]. The criterion for instability obtained in this study completely determines the solidification conditions under which the planar shape of the front is collapsed due to perturbations of a certain nature.

On the basis of the results obtained in [1], a weakly nonlinear analysis of stability was done in [2–4]. This analysis made possible the calculation of amplitudes of oscillatory perturbations and, consequently, of the size of cells and the mean spacing between the impurity layers in the solid phase. Thus, in terms of the stability analysis, it is possible to predict internal characteristics of the solid phase obtained by directional solidification.

Because the real processes of solidification do not proceed at a constant rate, it is of interest to study the instability of solidification under unsteady motion of the solid–melt interface. The first attempt at such an analysis in the self-similar case was made in [5]. However, in this study, the linear analysis of dynamical instability, i.e., the instability that retains the planar front, was carried out. Moreover, in their numerical calculations, the authors of [5] did not take into account the effect of impurity displacement deep into the melt, which is caused by the moving front. The last circumstance is fundamental to the formation of the region of concentrational supercooling.

In this paper, we consider the problem of the morphological instability of an unsteady process which attains a self-similar mode of solidification. This means, virtually, that the phase interface is reasonably far from the walls of the ingot mold. As the main mode, we consider the self-similar regime of solidification with a rate inversely proportional to the square root of time. As is shown below, for this solidification scenario, the appearance of a region of concentrational supercooling ahead of the planar front is possible. Of course, this region can be favorable for the growth of individual morphologically salient sections of the front deep into the metastable zone and can cause the collapse of the frontal mode of solidification. In this case, the morphological perturbations evolve in time relative to an unsteady (self-similar) process of solidification (such evolution was experimentally observed in [6]). To establish the conditions of instability for the self-similar solidification, we carried out linear analysis of the stability, which showed that the appearance of protrusions of preferential growth was possible under the conditions of unsteady solidification. This last fact means that, in these cases, the use of the classical model of solidification can lead to inadequate results.

It should also be noted that the theory of morphological instability of unsteadily moving boundaries, which is proposed in this study and exemplified by directional solidification, can be used to investigate other processes with phase transitions (for example, freezing of mixtures in porous media, filtration, burning, etc.).

We consider a directional solidification process in a binary melt along the x-axis. In the solid phase and the melt, the following equations of thermal conductivity and impurity diffusion are fulfilled:

$$\frac{\partial T_S}{\partial t} = \kappa_S \Delta_{xy} T_S, \quad \frac{\partial C_S}{\partial t} = D_S \Delta_{xy} C_S, \quad x < X(t, y), \quad (1)$$

$$\frac{\partial T_L}{\partial t} = \kappa_L \Delta_{xy} T_L, \quad \frac{\partial C_L}{\partial t} = D_L \Delta_{xy} C_L, \quad x > X(t, y). \quad (2)$$

Ural State University,
pr. Lenina 51, Ekaterinburg, 620083 Russia

1028-3358/01/4607-0453$21.00 © 2001 MAIK “Nauka/Interperiodica”

Here, T_S and T_L are the temperatures in the solid and liquid phases, κ_S and κ_L are the coefficients of thermal conductivity in these phases, C_L and C_S are the concentrations of impurity in the melt and solid phase, D_L and D_S are the coefficients of diffusion for an impurity, t is the time, y is the spatial coordinate perpendicular to the axis of solidification, $X(t, y)$ is the position of the crystallization front, and $\Delta_{xy} = \frac{\partial^2}{\partial x^2} + \frac{\partial^2}{\partial y^2}$ is the Laplace operator.

At the phase interface $x = X(t, y)$, the condition of equality of temperatures to the phase-transition temperature and the condition of balance for heat and mass are fulfilled:

$$T_S = T_L = T_M + mC_L + \Gamma T_M K, \quad (3)$$

$$L_V \frac{dX}{dt} = K_S \frac{\partial T_S}{\partial x} - K_L \frac{\partial T_L}{\partial x}, \quad (4)$$

$$(1-k)C_L \frac{dX}{dt} + D_L \frac{\partial C_L}{\partial x} - D_S \frac{\partial C_S}{\partial x} = 0, \quad (5)$$

where T_M is the phase-transition temperature for a pure melt, m is the slope of the liquidus line, Γ is the coefficient of surface tension, K is the surface curvature equal to $\frac{d^2X}{dy^2}$ in the linear approximation, L_V is the latent heat of solidification referred to a unit volume, and K_S and K_L are the coefficients of thermal conductivity in the solid and liquid phases, respectively.

Furthermore, we assume that an impurity concentration in the solid phase is proportional to the impurity concentration at the melt front; i.e.,

$$C_S = kC_L, \quad x = X(t, y). \quad (6)$$

Here, k is the equilibrium coefficient of impurity distribution.

The asymptotic behavior of the distributions of temperatures and impurity concentration are assumed to be given; i.e.,

$$T_S \longrightarrow T_{S\infty}, \quad C_S \longrightarrow C_{S\infty}, \quad x \longrightarrow -\infty, \quad (7)$$

$$T_L \longrightarrow T_{L\infty}, \quad C_L \longrightarrow C_{L\infty}, \quad x \longrightarrow \infty. \quad (8)$$

Following study [5], we introduce the self-similar variables

$$\eta = \frac{x}{\sqrt{t}} - \lambda, \quad \Xi(y, \tau) = \frac{X(y, t)}{\sqrt{t}} - \lambda, \quad \tau = \sqrt{t}. \quad (9)$$

When the self-similar mode of solidification is established, the planar front is in the position $X = \lambda\sqrt{t}$, i.e., $\Xi = 0$, and all the functions depend only on a single variable η. Thus, λ specifies the self-similar rate of solidification $\frac{dX}{dt} = \frac{\lambda}{2\sqrt{t}}$, while the variable τ specifies the time deviations from the self-similar mode. Equations (1) and (2) with boundary conditions (3)–(6) in variables (9) take the form

$$\frac{\tau}{2}\frac{\partial T_S}{\partial \tau} = \frac{1}{2}(\eta + \lambda)\frac{\partial T_S}{\partial \eta} + \kappa_S\left(\frac{\partial^2 T_S}{\partial \eta^2} + \tau^2\frac{\partial^2 T_S}{\partial y^2}\right), \quad \eta < \Xi,$$

$$\frac{\tau}{2}\frac{\partial C_S}{\partial \tau} = \frac{1}{2}(\eta + \lambda)\frac{\partial C_S}{\partial \eta} + D_S\left(\frac{\partial^2 C_S}{\partial \eta^2} + \tau^2\frac{\partial^2 C_S}{\partial y^2}\right), \quad \eta < \Xi, \quad (10)$$

$$\frac{\tau}{2}\frac{\partial T_L}{\partial \tau} = \frac{1}{2}(\eta + \lambda)\frac{\partial T_L}{\partial \eta} + \kappa_L\left(\frac{\partial^2 T_L}{\partial \eta^2} + \tau^2\frac{\partial^2 T_L}{\partial y^2}\right), \quad \eta > \Xi,$$

$$\frac{\tau}{2}\frac{\partial C_L}{\partial \tau} = \frac{1}{2}(\eta + \lambda)\frac{\partial C_L}{\partial \eta} + D_L\left(\frac{\partial^2 C_L}{\partial \eta^2} + \tau^2\frac{\partial^2 C_L}{\partial y^2}\right), \quad \eta > \Xi;$$

$$T_L = T_S = T_M + mC_L + \Gamma T_M \tau \frac{\partial^2 \Xi(y, \tau)}{\partial y^2}, \quad \eta = \Xi(y, \tau); \quad (11)$$

$$\frac{L_V}{2}\left[\Xi(y, \tau) + \lambda + \tau\frac{\partial \Xi(y, \tau)}{\partial \tau}\right] = K_S\frac{\partial T_S}{\partial \eta} - K_L\frac{\partial T_L}{\partial \eta}, \quad \eta = \Xi(y, \tau); \quad (12)$$

$$\frac{(1-k)C_L}{2}\left[\Xi(y, \tau) + \lambda + \tau\frac{\partial \Xi(y, \tau)}{\partial \tau}\right] + D_L\frac{\partial C_L}{\partial \eta} - D_S\frac{\partial C_S}{\partial \eta} = 0, \quad \eta = \Xi(y, \tau), \quad (13)$$

while conditions (7) and (8) are fulfilled for $\eta \longrightarrow -\infty$ and $\eta \longrightarrow \infty$, respectively.

The self-similar solutions $T_{SS}(\eta)$, $C_{SS}(\eta)$, $T_{LS}(\eta)$, and $C_{LS}(\eta)$ to the set of equations cited have the form

$$T_{SS}(\eta) = T_{S\infty} + (T_M + mC_{LI} - T_{S\infty})\frac{\operatorname{erfc}(-(\eta + \lambda)/\sqrt{4\kappa_S})}{\operatorname{erfc}(-\lambda/\sqrt{4\kappa_S})},$$

$$C_{SS}(\eta) = C_{S\infty} + (kC_{LI} - C_{S\infty})\frac{\operatorname{erfc}(-(\eta + \lambda)/\sqrt{4D_S})}{\operatorname{erfc}(-\lambda/\sqrt{4D_S})}, \quad (14)$$

$$T_{LS}(\eta) = T_{L\infty} + (T_M + mC_{LI} - T_{L\infty})\frac{\mathrm{erfc}((\eta+\lambda)/\sqrt{4\kappa_L})}{\mathrm{erfc}(\lambda/\sqrt{4\kappa_L})},$$

$$C_{LS}(\eta) = C_{L\infty} + (C_{LI} - C_{L\infty})\frac{\mathrm{erfc}((\eta+\lambda)/\sqrt{4D_L})}{\mathrm{erfc}(\lambda/\sqrt{4D_L})}.$$

In study [7], the expressions for the impurity concentration C_{LI} at the front and for the "rate" of solidification λ as functions of thermal characteristics of the melt and the values $T_{L\infty}$, $T_{S\infty}$, $C_{L\infty}$, and $C_{S\infty}$ governing the solidification process were found. The plot of the function $\lambda(T_{L\infty})$ is shown in the figure (the thermal characteristics of the calculated melt are listed in the table).

The stability of self-similar solutions can be destroyed, in particular, by concentrational supercooling, which was first described by Ivantsov [8]. The condition for the occurrence of such supercooling in a certain zone ahead of the solidification front can be represented as

$$m\frac{\partial C_{LS}}{\partial x} > \frac{\partial T_{LS}}{\partial x}, \quad x = \lambda\sqrt{t}$$

or (15)

$$m\frac{dC_{LS}}{d\eta} > \frac{dT_{LS}}{d\eta}, \quad \eta = 0.$$

If condition (15) is not fulfilled, the solidification proceeds in terms of the classical problem with a planar front. Substituting the functions $C_{LS}(\eta)$ and $T_{LS}(\eta)$ from relationships (14) into the last inequality, we obtain the criterion for the concentrational supercooling for the self-similar mode of solidification:

$$\frac{U(\lambda/\sqrt{4\kappa_L})}{U(\lambda/\sqrt{4D_L})} < \frac{m(C_{L\infty} - C_{LI})}{T_{L\infty} - T_M - mC_{LI}}\sqrt{\frac{\kappa_L}{D_L}}, \qquad U(\xi) = \frac{2\exp[-\xi^2]}{\sqrt{\pi}\,\mathrm{erfc}[\xi]}. \tag{16}$$

In obtaining criterion (16), we took into account that $U(\xi) > 0$ and $T_{L\infty} - T_M - mC_{LI} > 0$. Inequality (15) specifies the values of the rate λ for which the melt solidifies with the supercooling zone in front of the interface between the solid phase and the two-phase zone. Making the left-hand side of inequality (16) equal to the right-hand side, we plot the $\lambda(T_{L\infty})$ dependence, which is shown in the figure by the dashed line. The calculations show that the supercooling zone is located above this curve, whose intersection with the plot of the function $\lambda(T_{L\infty})$ gives the critical value of the rate $\lambda = \lambda_*$. Thus, for $\lambda < \lambda_*$, self-similar solidification occurs, while for $\lambda > \lambda_*$, there is a metastable zone before the planar front. As a consequence, the description of solidification seems to be, in this case, not always well-posed in terms of the classical model with a planar front.

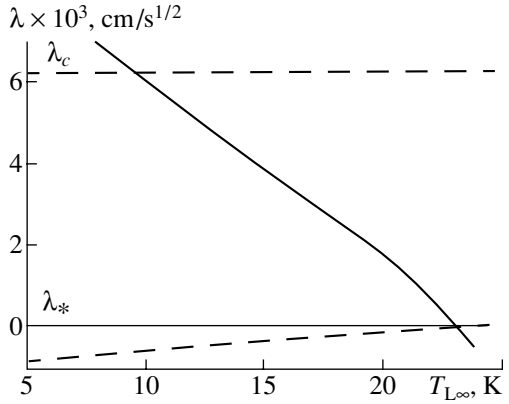

Self-similar rate λ of solidification (solid curve) as a function of temperature $T_{L\infty}$ of a melt at $T_{S\infty} = -30$ K. All the temperatures are measured relative to the phase-transition temperature of a pure melt; i.e., $T_M = 0$. $C_{L\infty} = 3$ wt % and $C_{S\infty} = 2.5$ wt %. The upper dashed line is the neutral stability curve; the instability region is above the curve. The lower dashed line is the curve of the concentrational supercooling that is plotted in correspondence with inequality (16); the region of concentrational supercooling is above the curve.

Further, we show that the evolution of morphological perturbations is possible in the supercooling region under certain conditions.

We consider that the planar phase interface exhibits small perturbations Ξ' with respect to the position $\eta = 0$. This leads to perturbations of the concentrational fields $C'_L = C_L - C_{LS}$, $C'_S = C_S - C_{SS}$ and the temperature fields $T'_L = T_L - T_{LS}$, $T'_S = T_S - T_{SS}$ relative to their self-similar values. Expanding boundary conditions (11)–(13) and (6) in Taylor series in the neighborhood of the point

Thermal properties of the calculated alloy (according to [5])

Parameter	Value	Units
K_L	0.159	J/(cm s K)
K_S	0.297	J/(cm s K)
κ_L	0.108	cm^2/s
κ_S	0.202	cm^2/s
D_L	3×10^{-5}	cm^2/s
D_S	6×10^{-7}	cm^2/s
L_V	256	J/cm^3
m	–2.33	K/wt %
k	0.3	–

$\eta = 0$ and restricting our consideration to only the linear terms in perturbations, we obtain

$$\frac{\tau}{2}\frac{\partial T'_L}{\partial \tau} = \frac{1}{2}(\eta + \lambda)\frac{\partial T'_L}{\partial \eta} + \kappa_L\left(\frac{\partial^2 T'_L}{\partial \eta^2} + \tau^2\frac{\partial^2 T'_L}{\partial y^2}\right),$$
$$\eta > \Xi'(y, \tau),$$

$$T'_L - T'_S + H_1\Xi' = 0, \quad H_1 = \frac{dT_{LS}}{d\eta} - \frac{dT_{SS}}{d\eta}, \quad \eta = 0, \quad (17)$$

$$T'_L - mC'_L + H_2\Xi' - \Gamma T_M\tau\frac{\partial^2 \Xi'(y, \tau)}{\partial y^2} = 0, \quad (18)$$
$$\eta = 0,$$

$$K_S\frac{\partial T'_S}{\partial \eta} - K_L\frac{\partial T'_L}{\partial \eta} + H_3\Xi' - \frac{L_V}{2}\tau\frac{\partial \Xi'(y, \tau)}{\partial \tau} = 0, \quad (19)$$
$$\eta = 0,$$

$$\frac{1-k}{2}\left[\lambda C'_L + C_{LS}\tau\frac{\partial \Xi'(y, \tau)}{\partial \tau}\right] + D_L\frac{\partial C'_L}{\partial \eta}$$
$$-D_S\frac{\partial C'_S}{\partial \eta} + H_4\Xi' = 0, \quad \eta = 0, \quad (20)$$

$$kC'_L - C'_S + H_5\Xi' = 0, \quad \eta = 0, \quad (21)$$

where the following designations are introduced:

$$H_2 = \frac{dT_{LS}}{d\eta} - m\frac{dC_{LS}}{d\eta},$$

$$H_3 = K_S\frac{d^2 T_{SS}}{d\eta^2} - K_L\frac{d^2 T_{LS}}{d\eta^2} - \frac{L_V}{2}, \quad \eta = 0,$$

$$H_4 = D_L\frac{d^2 C_{LS}}{d\eta^2} - D_S\frac{\partial^2 C_{SS}}{\partial \eta^2}$$
$$+ \frac{1-k}{2}C_{LS} + \frac{1-k}{2}\lambda\frac{dC_{LS}}{d\eta}, \quad \eta = 0,$$

$$H_5 = k\frac{dC_{LS}}{d\eta} - \frac{dC_{SS}}{d\eta}, \quad \eta = 0.$$

In order to save room no values of T_{SS}, T_{LS}, C_{SS}, and C_{LS} are substituted from expressions (14). In addition, with the same purpose, we wrote out only a single equation for perturbations of a temperature T'_L in the liquid phase. From conditions (7) and (8) it follows that the perturbations must satisfy the conditions $T'_L \longrightarrow 0$ and $C'_L \longrightarrow 0, \eta \longrightarrow \infty$; $T'_S \longrightarrow 0$ and $C'_S \longrightarrow 0, \eta \longrightarrow -\infty$.

Using the method of separation of variables, it is easy to show that the solutions satisfying these conditions are expressed in terms of the parabolic-cylinder functions $D_\nu(z)$ [9]:

$$T'_S = h_1\exp\left[-\frac{(\eta + \lambda)^2}{8\kappa_S}\right]$$
$$\times D_{-2\mu-1}\left[-\frac{\eta + \lambda}{\sqrt{2\kappa_S}}\right]\tau^{2\mu}\exp[\kappa_S\alpha_1^2\tau^2 + \alpha_1 y],$$

$$T'_L = h_2\exp\left[-\frac{(\eta + \lambda)^2}{8\kappa_L}\right]$$
$$\times D_{-2\mu-1}\left[\frac{\eta + \lambda}{\sqrt{2\kappa_L}}\right]\tau^{2\mu}\exp[\kappa_L\alpha_2^2\tau^2 + \alpha_2 y],$$

$$C'_L = h_3\exp\left[-\frac{(\eta + \lambda)^2}{8D_L}\right]$$
$$\times D_{-2\mu-1}\left[\frac{\eta + \lambda}{\sqrt{2D_L}}\right]\tau^{2\mu}\exp[D_L\alpha_3^2\tau^2 + \alpha_3 y],$$

$$C'_S = h_4\exp\left[-\frac{(\eta + \lambda)^2}{8D_S}\right]$$
$$\times D_{-2\mu-1}\left[-\frac{\eta + \lambda}{\sqrt{2D_S}}\right]\tau^{2\mu}\exp[D_S\alpha_4^2\tau^2 + \alpha_4 y].$$

Here, h_1, h_2, h_3, and h_4 are the amplitudes of perturbations and α_1, α_2, α_3, and α_4 are the constants of separation of variables that play the role of wave numbers.

The exponent of the time variable τ was chosen to be identical and equal to 2μ everywhere because it represents the increment of dynamical perturbations (when the front retains a planar shape). This case was investigated in [5]. For the cited solutions for perturbations to satisfy boundary conditions (17)–(21), it is possible to seek solutions $\Xi'(y, \tau)$ for perturbations of the self-similar front by expanding them into time series with respect to the variable τ, as in study [5], where such an analysis was done for investigating kinetics. However, we present here considerations that enable us to evade this laborious procedure.

Let α_j (j = 1, 2, 3, or 4) represent first a real number (monotonic perturbations); i.e., $\alpha_j = \gamma_1$. In this case, for an arbitrary μ value, the process of solidification is absolutely unstable because the time exponent is positive for all the perturbations. Let α_j be now pure imaginary; i.e., $\alpha_j = i\gamma_2$ (i is the unit imaginary number). In this case, the time exponent is negative ($\alpha_j^2 = -\gamma_2^2$) and the solidification process is absolutely stable.

Further, we consider the case when α_j are complex: $\alpha_j = \beta_1 + i\beta_2$. The time behavior of perturbations is now completely determined by the real part $\mathrm{Re}\alpha_j^2 = \beta_1^2 - \beta_2^2$, because all the perturbations are proportional to $\tau^{2\mu}\exp[n(\beta_1^2 - \beta_2^2)\tau^2]$ (n plays the role of the coefficients κ_S, κ_L, D_S, or D_L), while the imaginary part ($\mathrm{Im}\alpha_j^2 = 2\beta_1\beta_2 i$) describes the oscillations of the front around the self-similar position. If $\beta_1^2 > \beta_2^2$, the solidification process is unstable with respect to the morphological perturbations for arbitrary values of μ; if $\beta_1^2 < \beta_2^2$, it is stable. For this reason, the curve of neutral stability requires the fulfillment of the conditions $\beta_1^2 = \beta_2^2$ and $\mu = 0$. It follows from this that $\beta_2 = \pm\beta_1$ in the neutral stability curve and that the perturbations oscillate in time following the law $\exp[\pm i \times 2n\beta_1^2\tau^2]$, but they are always bounded in amplitude; i.e., they do not evolve (the so-called mode of neutral equilibrium).

This regime changes to the mode of morphological instability for $\alpha_j = \gamma_1 = \beta_1(1 \pm i)$; from here, it follows that $\beta_1 = \gamma_1 = 0$. Similarly, the mode of neutral equilibrium changes to the mode of absolute morphological stability when the conditions $\alpha_j = i\gamma_2 = \beta_1(1 \pm i)$ are satisfied. This means, in turn, that $\beta_1 = \gamma_2 = 0$.

To summarize, we conclude that the curve of neutral stability corresponds to the relationships $\beta_1 = 0$ and $\beta_2 = 0$. This means that all α_j and μ are equal to zero in the neutral stability curve. Therefore, the curves of neutral morphological and dynamical stability completely coincide.

In this case, all the perturbations are expressed in terms of the parabolic-cylinder functions D_{-1}, which, in turn, are expressed through the error function and the exponent as follows [9, 10]:

$$D_{-1}(z) = \sqrt{\frac{\pi}{2}}\exp\left[\frac{z^2}{4}\right]\mathrm{erfc}\left(\frac{z}{\sqrt{2}}\right).$$

Using this relationship, we come to the following expressions for perturbations of temperatures and concentrations on the neutral stability curve:

$$T_S' = h_1\sqrt{\frac{\pi}{2}}\mathrm{erfc}\left[-\frac{\eta + \lambda}{\sqrt{4\kappa_S}}\right],$$

$$T_L' = h_2\sqrt{\frac{\pi}{2}}\mathrm{erfc}\left[\frac{\eta + \lambda}{\sqrt{4\kappa_L}}\right],$$

$$C_L' = h_3\sqrt{\frac{\pi}{2}}\mathrm{erfc}\left[\frac{\eta + \lambda}{\sqrt{4D_L}}\right],$$

$$C_S' = h_4\sqrt{\frac{\pi}{2}}\mathrm{erfc}\left[-\frac{\eta + \lambda}{\sqrt{4D_S}}\right].$$

Since, as was shown above, the curves of neutral stability coincide for the morphological and dynamical perturbations, the perturbations of the front (rate) of solidification are expressed through a constant amplitude h_5 in the neutral-equilibrium mode; i.e., we can write

$$\Xi' = h_5.$$

Substituting these expressions for perturbations into boundary conditions (17)–(21), we obtain a set of five linear equations whose nontrivial solvability condition requires that the determinant composed of the coefficients of the amplitudes h_1, h_2, h_3, h_4, and h_5 be equal to zero. Expanding the determinant of the fifth order, we come to the equation of the neutral stability curve, which is not written here for the sake of brevity.

In Fig. 1, the neutral stability curve is shown by the upper dashed line. Its intersection with the function $\lambda(T_{L\infty})$ (solid curve) gives the critical value $\lambda = \lambda_c$ for which the stable mode of solidification changes to an unsteady one. In other words, if $0 < \lambda < \lambda_*$, the solidification process is stable and proceeds without the supercooling region before the planar front; if $\lambda_* < \lambda < \lambda_c$, a metastable region of concentrational supercooling appears ahead of the front, which still retains a planar shape. This region does not give rise to the development of perturbations, because the latent heat released during the solidification removes the region of supercooling. On further increasing the rate $\lambda > \lambda_c$, the supercooling ahead of the front increases (because the impurity is expelled deep into the melt) and the front becomes unstable to perturbations of arbitrary nature, both monotonic and vibrational. In other words, there is a sharp boundary between the stable and unstable scenarios of solidification. Unstable solidification can lead to dendritic growth (nucleation and growth of elements of the solid phase in the supercooled prefront region), i.e., to the formation of the two-phase zone.

Therefore, it seems important to take into account the presence of the supercooling metastable region ahead of the solidification front in considering the processes of solidification.

ACKNOWLEDGMENTS

This study was made possible in part by Award no. REC-005 of the US Civilian Research and Development Foundation for the Independent States of the Former Soviet Union (CRDF).

REFERENCES

1. W. W. Mullins and R. F. Sekerka, J. Appl. Phys. **35**, 444 (1964).
2. D. J. Wollkind and L. A. Segel, Philos. Trans. R. Soc., London, Ser. A **268**, 351 (1970).
3. J. I. D. Alexander, D. J. Wollkind, and R. F. Sekerka, J. Cryst. Growth **79**, 849 (1986).
4. L. Yu. Iskakova and V. V. Mansurov, Available from VINITI No. 2124-V88 (Moscow, 1988).
5. S. R. Coriell, G. B. McFadden, and R. F. Sekerka, J. Cryst. Growth **200**, 276 (1999).
6. H. E. Huppert and M. G. Worster, Nature **314**, 703 (1985).
7. S. R. Coriell, G. B. McFadden, R. F. Sekerka, and W. J. Boettinger, J. Cryst. Growth **191**, 573 (1998).
8. G. P. Ivantsov, Dokl. Akad. Nauk SSSR **81**, 179 (1951).
9. *Higher Transcendental Functions (Bateman Manuscript Project)*, Ed. by A. Erdelyi (McGraw-Hill, New York, 1953; Nauka, Moscow, 1974), Vol. 2.
10. N. N. Lebedev, *Special Functions and Their Applications* (Gostekhizdat, Moscow, 1963; Prentice-Hall, Englewood Cliffs, 1965).

Translated by V. Bukhanov

Doklady Physics, Vol. 46, No. 7, 2001, pp. 459–462. Translated from Doklady Akademii Nauk, Vol. 379, No. 1, 2001, pp. 38–41.
Original Russian Text Copyright © 2001 by Belobrov, Gordeev, Petrakovskaya, Falaleev.

PHYSICS

Paramagnetic Properties of Nanodiamond

P. I. Belobrov*, S. K. Gordeev, É. A. Petrakovskaya***, and O. V. Falaleev*****

Presented by Academician K.S. Aleksandrov December 25, 2000

Received January 19, 2001

In nanodiamonds obtained by the explosion method [1–3], the existence of diamond molecular forms [4] is based on the thermodynamic stability of 5-nm-sized diamond particles [5, 6]. There are several basic characteristics of molecular diamond which only quantitatively differ for diamond and nanodiamond, namely, the region of coherent X-ray scattering, the specific surface area, the stable-particle size, etc. It is of importance that the exact reproduction of conditions for synthesis and extraction results in a yield of nanodiamonds with the same characteristics [7]. The absence of a physical parameter defining the diamond molecule is the basic cause of underestimating the fact that any ultradisperse diamond obtained by the explosion method consists of the spherical molecules and edged particles of nanocrystalline diamond.

In this paper, the radiospectroscopic methods of electron paramagnetic resonance (EPR) and nuclear magnetic resonance (NMR) are used to experimentally prove the existence of diamond macromolecules. The chemical activity of nanodiamond depends on surface states traditionally associated with dangling bonds, i.e., with unpaired electrons. Therefore, nanodiamonds with exactly determined surface states were chosen for the experiment. These nanodiamonds, obtained using various methods, were subjected to different purification stages and had strongly distinguished values of incombustible remnants or ash content.

For EPR-spectrum measurements of the same samples, EPR-3, SE/x-2544, EMX EPR Bruker (9 GHz), and RE08 (36 GHz) spectrometers were used (Table 1). The measurements were carried out at temperatures of 290 and 77 K. While determining the absolute concentration of unpaired spins, $CuCl_2 \cdot 5H_2O$ served as a standard. Three standards were used in the measurement of the Lande g-value: α-diphenyl-β-picrylhydrazyl (DPPG, $g = 2.0036$), standard samples of Mn^{2+} ions ($g = 1.9803$) in MgO, and Li ($g = 2.0023$). The mean values of the g-value and line widths ΔH for the samples under study are given in Table 1, where the standard deviation for the last significant digit is indicated in brackets. Each sampling relates to the spectra of the same sample. The calculated values of ΔH were averaged by interpolating both the shape of the absorption line by the Lorentzian curve and the values of g-values obtained with various standards, scans, and modulations.

The temperature-independent behavior of the paramagnetic-absorption line shape for nanodiamond was first observed in [8]. There, it was shown that the concentration of unpaired electrons attained a value on the order of 10^{19} spin/g within the temperature range from 77 to 600 K [8]. The g-values at temperatures of 77 and 290 K also did not differ within the experimental error. In addition, by varying the microwave-field amplitude from 1 to 40 dB, only the EPR-signal intensity changed, whereas the g-value and the line width remained invariable. Therefore, data obtained with different equipment and for different temperatures, standards, and attenuation magnitudes were used for increasing the sampling volume and reducing the measurement error.

An example of a nanodiamond EPR spectrum is shown in Fig. 1. Parameters of paramagnetic absorption for nanodiamond particles with various surface states are given in Table 1. As can be seen, the nanodiamond EPR spectrum virtually does not change with significant variation of the particle-surface structure. The corresponding mean g-values and ΔH for powder nanodiamond (samples nos. 1–8) are, respectively, 2.0027(5) and 0.87(6) mT. The DPPG and manganese standards do not allow us to determine the g-value with sufficient accuracy. Using a Li standard, it is possible to increase the accuracy by an order of magnitude: for example, the g-value for samples no. 9 and no. 12 is equal to 2.00271(3) and 2.00266(2), respectively.

In nanocomposite samples (nos. 9–15), the ratio γ for the pyrocarbon mass to that of the nanodiamond varies from 0 to 40%. In this case, the EPR spectrum virtually does not change. Consequently, the nanocomposite spectrum represents the EPR spectrum of nano-

* *Institute of Biophysics, Siberian Division, Russian Academy of Sciences, Akademgorodok, Krasnoyarsk, 660036 Russia*

** *Central Research Institute of Materials, ul. Paradnaya 8, St. Petersburg, 191014 Russia*

*** *Kirenskiĭ Institute of Physics, Siberian Division, Russian Academy of Sciences, Akademgorodok, Krasnoyarsk, 660036 Russia*

1028-3358/01/4607-0459$21.00 © 2001 MAIK "Nauka/Interperiodica"

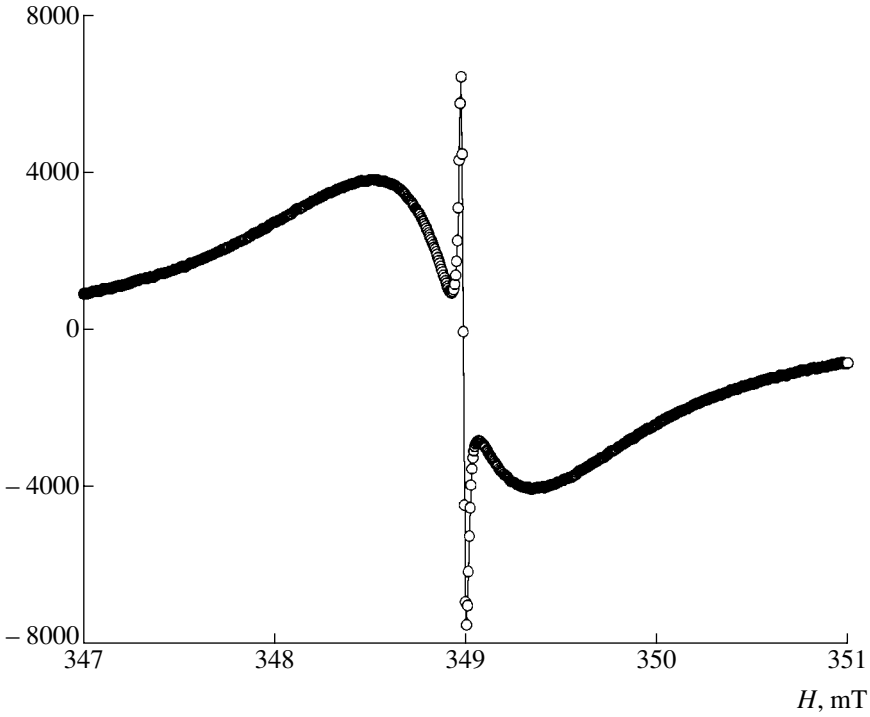

Fig. 1. Central part of the EPR spectrum (EMX EPR Bruker) of the NDC 10 nanocomposite with the Li standard (g = 2.0023). The scan and the modulation are 50 and 0.01 mT.

diamond. Data testifying to the independence of an EPR signal from the chemical modification of the nanodiamond surface (chlorination, methylation, etc.) show that the paramagnetic properties of the nanodiamond are probably determined only by the sp^3 core of a nanodiamond molecule.

Determination of the unpaired-spin concentration was performed at a high accuracy for three samples

Table 1

Item	Description of samples	g-value	ΔH, mT
1	Preparation [1], purification [7], 4% ash	2.0030(4)	0.85(7)
2	Sample no. 1, modification of the surface by chlorine	2.0028(7)	0.88(8)
3	Sample no.1, modification of the surface by CH_3	2.0029(6)	0.84(9)
4	Preparation and purification [3], 2% ash	2.0022(3)	0.86(6)
5	Sample no. 4, purification by sedimentation, 0.3% ash	2.0026(2)	0.86(2)
6	Preparation [3], purification by ozone, 1% ash	2.0027(5)	0.88(1)
7	Sample no. 4, modification of the surface by a protein	2.0024(1)	0.97(1)
8	Preparation and purification [3], 1% ash	2.0024(2)	0.85(3)
9	NDC 0	2.0026(1)	0.84(2)
10	NDC 0.5	2.0026(1)	0.86(1)
11	NDC 5	2.0027(1)	0.85(1)
12	NDC 10	2.0026(1)	0.84(4)
13	NDC 20	2.0025(1)	0.85(1)
14	NDC 30	2.0026(1)	0.85(1)
15	NDC 40	2.0027(1)	0.86(3)
	Mean values	2.0027(1)	0.86(2)

Note: Composites nos. 9-15, (NDC γ) made of nanodiamond (sample no. 1) and pyrocarbon are obtained using the method described in [9]. The carbon content [C] > 99 wt % in contrast to nos. 1–8, in which [C] < 85 wt %.

Table 2

Sample	Concentration of unpaired spins			
	T = 293 K		T = 77 K	
	30 dB	40 dB	30 dB	40 dB
NDC 20	4.9×10^{19}	4.7×10^{19}	–	–
NDC 30	3.6×10^{19}	3.4×10^{19}	3.4×10^{19}	3.7×10^{19}
NDC 40	2.9×10^{19}	–	2.8×10^{19}	–

with a side standard at an attenuation of 30 and 40 dB. The results are shown in Table 2; the concentration of radicals is expressed in spins per gram of the nanocomposite.

As follows from Table 2, the number of unpaired spins is proportional to the quantity $\frac{1}{\gamma}$, i.e., to the ratio $\frac{sp^3}{sp^2}$. In other words, the number of radicals is approximately equal to Avogadro's number divided by the number ~13400 of carbon atoms in a 5-nm nanodiamond. Any variation of the pyrocarbon mass in the composite does not change the number of spins in nanodiamond. This indicates the absence of saturation in nanodiamond even at T = 77 K and demonstrates a strong coupling of an unpaired electron with the nanodiamond sp^3-core.

While passing to the 36-GHz range, the EPR-signal parameters observed, i.e., the g-value and ΔH, did not change within the measurement accuracy. This result indirectly testifies to the absence of inhomogeneous line broadening and allows us to exclude free local radicals from consideration. We may also ignore the dipole broadening, as the line shape is well described by a Lorentzian curve. The distortions of the spatial structure near the surface can be determined by the NMR method.

The NMR of nanodiamond according to the ^{13}C and ^{11}B isotope was first investigated in [10] and [11], respectively. We studied the purest nanodiamond of the type corresponding to the sample no. 5 with a incombustible remnant of 0.2% by weight. The NMR spectra of ^{13}C were taken using a CXP-400 Bruker spectrometer with a magnetic field H_0 = 9.4 T at a frequency of 100.6 MHz. The interaction with protons was suppressed, and the rotation under the magic angle at a frequency exceeding 1 kHz was used. The number of spectra accumulated reached 500.

The results are shown in Fig. 2. It is seen that the resonance line is asymmetric and well decomposed into two Gaussian components, whose numerical values are presented in Table 3. The narrow line with δ = 35.1 ppm relates to diamond carbon; the wide line with δ = 34.2 ppm is caused by the nonequivalence of carbon atoms due to distortion of the tetrahedral coordination. It is seen that there is only 30% of the pure sp^3-phase in nanodiamond. The residual absorption of the microwave power in the EPR corresponds to distorted carbon–carbon (70%) bonds, these bonds also having sp^3-hybridization. The ^{13}C content is ~1%; therefore, ~100 carbon ^{12}C atoms account for one ^{13}C atom contributing to the absorption-line shape given in Fig. 1.

It is worth noting for comparison that jewelry and synthetic diamonds are characterized by chemical shifts at δ = 50 ppm and δ = 40 ppm, respectively [10].

The interpretation of single NMR and EPR lines is a difficult problem, and our case is not an exception. As follows from [11], the number of nitrogen and boron atoms in the sample no. 1 are approximately equal. Therefore, the image of dangling C–C bonds is not final, because nitrogen and oxygen impurities can form paramagnetic centers. This question should be verified independently by thorough analysis of the relaxation times and EPR signal within the 2-mm wave range.

Plastically deformed diamonds [12, 13] and the adamantan radical [14] have paramagnetic properties similar to those of nanodiamond. The EPR signal of the diamond-surface states exhibits a single line with g = 2.0027 ± 0.0002 and ΔH = 0.55 mT [12]. The signal intensity is inversely proportional to the microcrystal size, the line has a Lorentzian shape, and the number of paramagnetic centers is close to that of carbon atoms on the diamond surface [13].

Detailed discussion of the physical nature of the "paramagnetic invariant" observed is beyond the scope of the present paper. However, it is clear that independently of the interpretation of the data obtained, nanodiamond is a stable macroradical in which the three-dimensional diamond core of each spherical macromolecule has an unpaired electron localized at distorted sp^3-bonds.

In the present paper, the independence of the paramagnetic properties from the nanodiamond production

Table 3

Nos.	Position		Width		Amplitude, arb. units	Relative integral intensity
	Hz	ppm	Hz	ppm		
1	3532	35.104	278	2.763	4.18	27.83
2	3445	34.236	1261	12.532	2.39	72.17

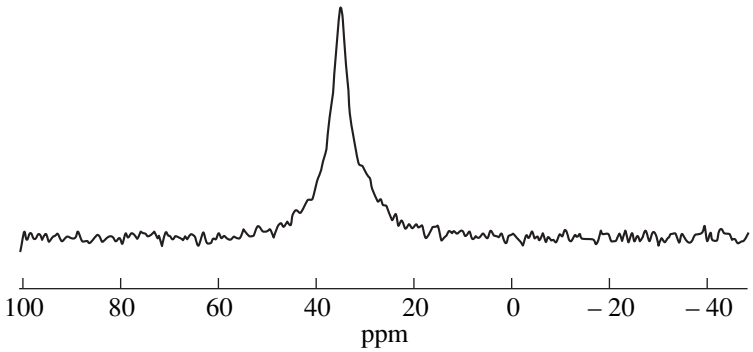

Fig. 2. ^{13}C NMR spectrum for nanodiamond. The numerical values of chemical shifts, intensities, and line widths after decomposition into Gaussian components are given in Table 3.

method and purification technique is experimentally confirmed. The concentration of unpaired spins, which is equal to 4×10^{19} spin/g of the nanocomposite (about one spin per nanodiamond particle), is determined. The magnitude of the g-value = 2.0027×10^{-4} and the EPR-line width $\Delta H = 0.86 \pm 0.02$ mT is measured. These values remain constant within the experimental error and are independent of the temperature, composition, structure, and state of the nanodiamond surface. It is shown by the ^{13}C NMR method that the nanodiamond contains 70% of distorted sp^3 bonds in which an unpaired electron is probably localized.

The paramagnetic properties observed above are qualitatively different for diamond and nanodiamond and, as a physical parameter, exactly define the nanodiamond. Therefore, the EPR and NMR spectra may be used as a criterion to determine the diamond molecular state. The physical nature of the nanodiamond paramagnetic-property independence from the state of its surface consists in the fact that molecular diamond is a stable microradical.

The existence of local paramagnetic centers or dangling bonds is considered a conventional interpretation of one free spin per molecule. In addition, there are grounds to suggest that a collective unpaired electron can reside at surface Tamm levels that stabilize the de Broglie wave having a wavelength $\lambda = 4$ nm and an electron energy of about 0.1 eV [15]. This implies that in each spherical particle consisting of $\sim 10^4$ carbon atoms, the neutralization of the surface charge (on the order of one electron per particle) is, probably, accompanied by the formation of a radical nanodiamond state with a 1/2 spin.

ACKNOWLEDGMENTS

We are grateful to P.Ya. Detkov, A.P. Puzyr', and V.F. Gerasimenko for preparing samples nos. 4–6, no. 7, and no. 8, respectively. We are also grateful to R.I. Samoĭlova for analyzing the EPR spectra and to K.S. Aleksandrov and V.A. Ignatchenko for their helpful discussions and useful critical remarks.

This work was supported in part by the INTAS, grant no. 1754.

REFERENCES

1. A. M. Staver, N. V. Gubareva, A. I. Lyamkin, *et al.*, Fiz. Goren. Vzryva **20** (5), 100 (1984).
2. N. R. Greiner, D. S. Philips, J. D. Johnson, *et al.*, Nature **333**, 440 (1988).
3. K. V. Volkov, V. V. Danilenko, and V. N. Elin, Fiz. Goren. Vzryva **26** (3), 123 (1990).
4. A. P. Rudenko, I. I. Kulakova, and V. L. Skvortsova, Usp. Khim. **62** (2), 99 (1993).
5. P. Badziag, W. S. Verwoerd, W. P. Ellis, *et al.*, Nature **343**, 244 (1990).
6. M. Y. Gamarnik, Phys. Rev. B **54**, 2150 (1996).
7. G. A. Chiganova and A. S. Chiganov, Neorg. Mater. **35**, 581 (1999).
8. J. V. Tushko, S. B. Petrov, and V. V. Kharitonov, Interface **4**, 185 (1995).
9. S. K. Gordeev, S. G. Zhukov, Yu. I. Nikitin, *et al.*, Neorg. Mater. **31**, 470 (1995).
10. V. M. Mastikhin and A. L. Vereshchagin, in *Superdisperse Powders, Materials, and Nanostructures* (Krasnoyarsk, 1996), pp. 37–38.
11. Yu. N. Ivanov, A. V. Kalinkin, and Yu. V. Tushko, Neorg. Mater. **33**, 803 (1997).
12. G. K. Walters and T. L. Estle, J. Appl. Phys. **32**, 1854 (1961).
13. N. D. Samsonenko and E. V. Sobolev, Pis'ma Zh. Éksp. Teor. Fiz. **5**, 304 (1967) [JETP Lett. **5**, 250 (1967)].
14. R. J. Waltman, A. C. Ling, and J. Bargon, J. Phys. Chem. **86**, 325 (1982).
15. I. E. Tamm, Phys. Z. Sowjetunion **1**, 733 (1932).

Translated by T. Galkina

Doklady Physics, Vol. 46, No. 7, 2001, pp. 463–466. Translated from Doklady Akademii Nauk, Vol. 379, No. 2, 2001, pp. 177–180.
Original Russian Text Copyright © 2001 by Krivoguz, Norman.

PHYSICS

The Spinodal of Superheated Solid Metal

M. N. Krivoguz and G. É. Norman

Presented by Academician V.E. Fortov January 10, 2001

Received January 11, 2001

The formation of a liquid phase on the surface of a solid that is being melted is not associated with the energy consumption for creating a new surface. Therefore, the superheating of a solid is, generally speaking, impossible (see [1, p. 60]). However, it was noted in [1] that the situation changes if the solid is heated from the interior, while its surface is supported at a temperature below the melting point. This situation arises in the case of an electrical explosion of conductors, when the time of energy contribution is reduced to 10^{-9}–10^{-8} s (see [2, 3] and references therein). Under the conditions used in [2], the magnetic pressure (and, respectively, the melting temperature for the majority of metals) rises to the periphery of the conductor. In this case, the surface is cooled due to the radiation and thermal emission of hot electrons, the skin effect is absent, and the heating is uniform over the conductor bulk. Thus, we can expect that the melting begins only under considerable superheating, the probability of nucleation being the highest on the conductor axis, where the magnetic pressure is absent. Even when the nucleus has formed, the time of the melting-front propagation is long compared to the time of energy contribution (see [2]). The motion rate for the melting front in copper was calculated by the molecular-dynamics method [3]. This rate attained only 100 m/s for a superheating of 20%. Thus, for characteristic times of ~10^{-8} s, the melting front has a chance to propagate only by 10^{-2} of the wire radius. The maximum superheating of 5–6 sublimation energies was attained for the maximum energy-contribution rate of 10^{12} W/g [2].

The passage to a metastable state for rapid (~10^{-6} s) Joule heating was experimentally studied by Baĭkov and Shestak [4]. For a copper wire 3×10^{-2} cm in diameter at atmospheric pressure, superheating $\vartheta = \frac{T - T_m}{T_m} \simeq 0.13$ was attained, where T_m was the melting temperature. The kinetics of metal-bulk melting was theoretically investigated in 1984 by Motorin and Musher. The resulting estimate of the maximum superheating ϑ up to 20% or $T - T_m$ = 150–200 K were in agreement with the results of [4]. In experiments [5], gold wires superheated to a temperature of 12000 K were maintained in the solid state for a 1-ns voltage-pulse duration.

The transition of a solid into the superheated metastable state was noted by Urlin as early as 1965 when analyzing experiments on the action of intense shock waves on solids. The possibility of bulk superheating of solids behind the shock wave front was discussed in detail by Kuznetsov [6]. Experimental data on 20% superheating (i.e., on the order of 650 K) of haloid crystals of alkaline metals (KBr and CsBr) in shock waves were obtained in [7].

Thus, the bulk superheating of solids of various chemical compositions was actually observed experimentally in pulsed modes [2, 4, 5, 7] in agreement with the theoretical concepts [1, 6, 8]. This problem is also important for applications in connection with extended studies devoted to isochoric heating [9, 10]. At the same time, analysis of the superheating phenomenon is hampered by the absence of necessary information concerning the spinodal, i.e., the ultimately accessible superheating of solids.

We numerically simulated uniformly superheated noble-gas crystals of infinite size (without an open surface) using both the Monte Carlo method and the methods of molecular dynamics. The Monte Carlo method was also employed to simulate crystals formed by charges of the same sign against a compensating background and by particles interacting via a uniform soft-repulsion potential (see [3, 11] and references therein). However, in that case, the spinodal of a superheated metal was not investigated. This is the problem that is considered in the present paper.

THE MODEL AND THE CALCULATION METHOD

The curve representing the locus corresponding to the limit of the thermodynamic stability of a particular phase on the phase plane is called the spinodal. The criterion for the thermodynamic stability is the inequality

Moscow Institute of Physics and Technology, Institutskiĭ per. 9, Dolgoprudnyĭ, Moscow oblast, 141700 Russia

1028-3358/01/4607-0463$21.00 © 2001 MAIK “Nauka/Interperiodica”

$\left(\frac{\partial P}{\partial V}\right)_T < 0$, i.e., the points, in which $\left(\frac{\partial P}{\partial V}\right)_T = 0$, form the spinodal.

The spinodal of a solid, as other physical and chemical properties of the macrosystem, can be calculated by methods of computer simulation based on interparticle-interaction potentials. In this paper, based on the molecular-dynamics method, we investigate a system of 108 particles arranged in fcc-lattice sites. Test calculations have shown that the difference in the simulation with samples comprising 108 and 256 particles is lower than 2%. For eliminating surface effects on the system boundaries, we used the periodic boundary conditions. As a potential of the interparticle interaction, the soft-sphere pair potential $U = \varepsilon\left(\frac{\sigma}{r}\right)^n$ was chosen. This potential was also employed in [11, 12] for simulating crystals and in [13, 14] for describing the properties of liquid metals in a wide temperature region, including melting.

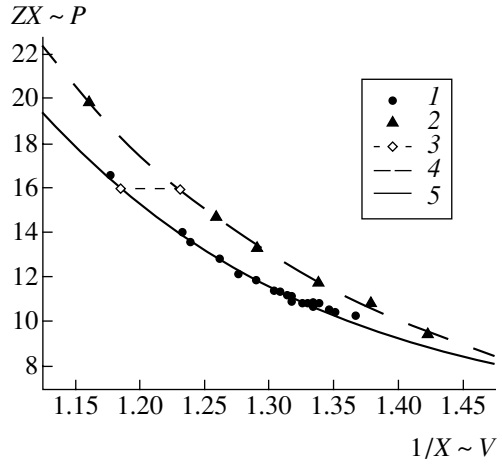

Fig. 1. Equation of state for $n = 12$ in dimensionless variables: (*1*) molecular-dynamic calculation for a solid, (*2*) molecular-dynamic calculation for a liquid, (*3*) phase transition recorded in [12]; (*4*) and (*5*) calculation results according to equations of state for a liquid and solid, respectively, [11].

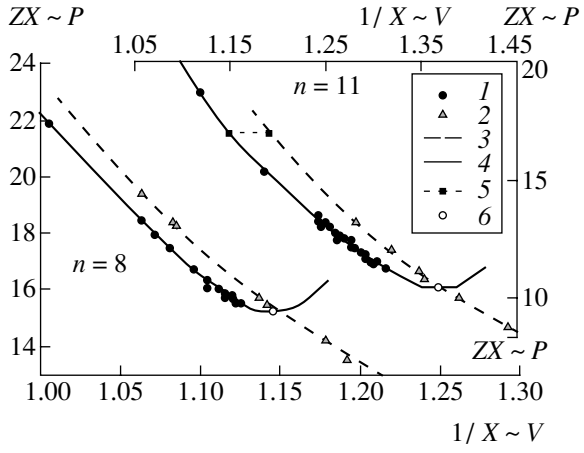

Fig. 2. Extrapolation of the equation of state for $n = 8$ and 11 to the spinodal point: (*1*) molecular-dynamics calculation for a solid; (*2*) molecular-dynamics calculation for a liquid; (*3*) and (*4*) approximating curves for liquid and solid phases, respectively; (*5*) crystal–liquid phase transition; and (*6*) spinodal point.

The soft-sphere potential is uniform; this provides the dependence of thermodynamic properties only on a single parameter $X = \frac{N\sigma^3}{\sqrt{2}V}\left(\frac{\varepsilon}{kT}\right)^{3/n}$. In this case, we can represent the free energy in the form (cf. [1, p. 116])

$$F = -3\left(\frac{1}{2} - \frac{1}{n}\right)NT\ln T + NT\varphi\left(\frac{VT^{3/n}}{N}\right),$$

where φ is the function of a single variable. Thus, a dimensionless quantity $Z = \frac{PV}{NkT}$ is the function of parameter X alone.

In the variables X and Z, the equation of state represents a single curve, each point (X_0, Z_0) of which is a surface in the (P, V, T) space. As the quantities $1/X$ and ZX are proportional to the volume V and pressure P at a constant temperature, respectively, the equation of state in the coordinates $(1/X, ZX)$ behaves like an isotherm on the PV diagram. Therefore, the problem of seeking the spinodal [the surface $\left(\frac{\partial P}{\partial V}\right)_T = 0$ in the coordinates $(1/X, ZX)$] is reduced to finding a point at which $\frac{\partial(ZX)}{\partial(1/X)} = 0$.

Thus, it is convenient to perform the calculations using the indicated reduced coordinates by plotting the data obtained on the $(1/X, ZX)$ diagram.

THE RESULTS OBTAINED IN THE REDUCED VARIABLES

The equations of states were obtained by the molecular dynamics method using a number of potentials ($n = 8$, 9, 10, 11, 12, and 13) for the crystalline phase in the metastable region and for the liquid phase. The data for the potential with $n = 12$ were compared with the equation of state [11] for a model solid with an fcc lattice and a similar potential of interparticle interaction (Fig. 1). We observed good agreement between the results, excluding the region in which the cutoff of the obtained equation of state for the crystalline phase takes place. The region near the spinodal was not purposefully investigated in [11, 12].

As can be seen from Fig. 2, in the case of both the potential with $n = 12$ and other values of n, the calculated curve terminates without attaining the spinodal point. This is likely associated with the violation of the mechanical stability of the system under investigation [8]. Problems associated with the criteria of

mechanical stability were beyond the scope of this paper. To immediately determine the spinodal, we use the extrapolation of the data obtained. As a spinodal point, we take the point in which the derivative $\frac{\partial(ZX)}{\partial(1/X)}$ of the approximating function vanishes. The error in determining the spinodal point, which is associated with the ambiguous choice of the approximating polynomials, is close to ~10%. For various values n of exponents in the description of the soft-sphere potential, a smooth dependence of coordinates of spinodal points on the value of n was obtained.

For the subsequent estimate of the degree of metal superheating, it is also necessary to know the position of the segment for the crystal–liquid phase transition. In [12], values of melting points and crystallization points were found for the potentials with $n = 4, 6, 9, 12$, and ∞. Interpolating these data, we are able to know the melting and crystallization points for intermediate values of n. The results obtained in the reduced variables are exhibited in the table.

The subscripts "melt," "cryst," "cutoff," and "spinod" at values of X and Z in the table imply, respectively, the points of melting and crystallization for equilibrium phases, the cutoff point of the calculated curve, i.e., seemingly, a point of mechanical buckling, and a point of the absolute loss of thermodynamic stability in which $\left(\frac{\partial P}{\partial V}\right)_T = 0$ (this point is found by extrapolation).

THE RESULTS OBTAINED FOR CERTAIN METALS

In [13, 14], experimental data on enthalpy, density, and sound velocity for liquid metals at high pressures and temperatures were thoroughly analyzed. As a result of this analysis, the parameters of the soft-sphere potential which most closely describe the available experimental results were determined. This made it possible to construct the spinodal in the actual (P, V, T) coordinates and to plot the spinodal curve on the actual phase diagram. In Fig. 4, we show a corresponding example for iron.

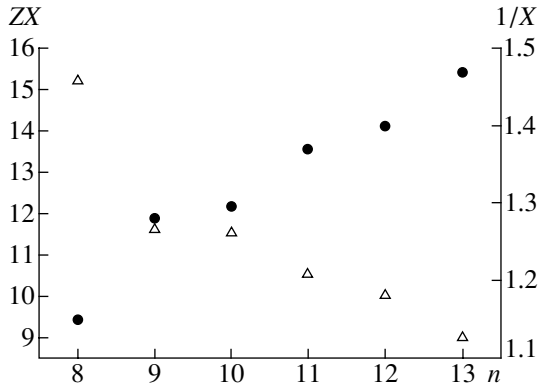

Fig. 3. Dependence of the spinodal point on the softness of the potential. (△) ZX, (●) $1/X$.

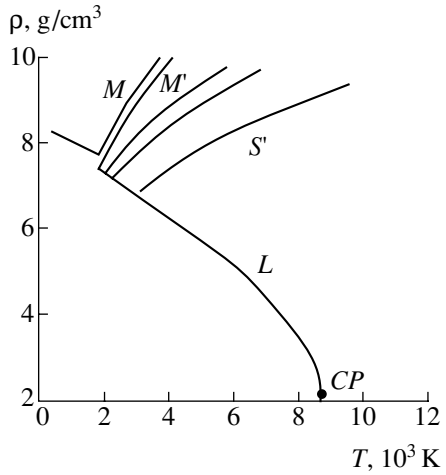

Fig. 4. Fragment of the phase diagram for iron. Data of [13]: M is the binodal in the melting region; L is the liquid in equilibrium with vapor; CP is the critical point. The results of calculations according to the soft-sphere model: M' is the binodal in the melting region, and S' is the spinodal.

Table

n	X_{melt}	X_{cryst}	X_{cutoff}	X_{spinod}	Z_{melt}	Z_{cryst}	Z_{cutoff}	Z_{spinod}
4	3.94	3.92			108	109		
6	1.56	1.54			39.1	39.6		
8 (Cu)	1.06	1.03	0.89	0.87	26	26.3	17.4	17.5
9 (W, Ta)	0.97	0.94	0.82	0.78	22.6	23.3	15.8	16.1
10 (Al)	0.91	0.88	0.80	0.77	21	21.7	15.6	15.0
11 (Fe)	0.87	0.84	0.76	0.73	19.5	20.2	14.6	14.4
12 (Pt, Pb)	0.84	0.813	0.74	0.71	19	19.7	14.14	14.3
13 (Mo)	0.83	0.77	0.708	0.68	17.7	18.4	12.7	13.2
∞	0.74	0.67			11.2	12.4		

The data obtained make it possible to estimate the maximum superheating. For the isochoric processes, the superheating amounts to 70% for Cu, 75% for Al, 90% for Fe and W, and 95% for Pb and Pt. For the isobaric superheating, the results are as follows: 50% for Cu, Al, Fe, and Pt and 60% for W.

The molecular-dynamics method makes it possible to estimate the melting time for a superheated metal in the case of the stability loss at the cutoff point of the equation of state for the solid phase. This value turned out to be on the order of 10 ps.

DISCUSSION OF THE RESULTS

At temperatures of ~1 eV, electrons begin to markedly contribute to the heat capacity of a medium. For example, the outer shells of a copper atom have the $d^{10}s^1$ structure. Accordingly, the electron structure of a copper crystal involves six Brillouin zones: one half-filled *s*-zone and five filled *d*-zones. However, the energy levels of all the *d*-zones differ within 2 eV from the Fermi energy. Therefore, at temperatures on the order of 1 eV and higher, all 11 electrons of the *s*- and *d*-zones begin to contribute to the electron heat capacity.

Since the electron component turned out to be so important, we can indicate the factors capable of causing an additional increase in the maximum energy contribution. For the rates of the energy contribution under discussion, a solid can pass not only into a metastable state but also into an electron-excited state. In the literature, two types of such electron excitations are discussed: the formation of Rydberg matter (Manykin *et al.*, 1982) and the separation of the electron temperature from the phonon temperature [15].

In spite of ignoring the indicated factors, the results obtained by us satisfactorily agree with available experimental data. The magnitudes of superheating by 20 and 13% obtained in [5, 7] and in [4], respectively, lie within the maximum superheating obtained in our study. The disposition of the binodal on the diagram of Fig. 4, which was found in the approximation of the soft-sphere model, describes qualitatively correctly the behavior of the actual binodal based on the results of this paper. The spinodal obtained in the framework of the present study can be used as the zero approximation with subsequent refinement through the help of the perturbation theory of the contribution of the electron and other components.

ACKNOWLEDGMENTS

The authors are grateful to P.R. Levashov and I.V. Lomonosov for kindly submitting data on the phase diagrams.

This study was supported by the Russian Foundation for Basic Research, project no. 00-02-16310a.

REFERENCES

1. L. D. Landau and E. M. Lifshitz, *Course of Theoretical Physics*, Vol. 5: *Statistical Physics* (Nauka, Moscow, 1995; Pergamon, Oxford, 1980), Part 1.
2. L. I. Chemezova, G. A. Mesyats, V. S. Sedoi, *et al.*, in *Proceedings of the XVIII International Symposium on Discharges and Electrical Insulation in Vacuum, Eidhoven, 1998*, p. 48.
3. A. A. Valuev and G. É. Norman, Zh. Éksp. Teor. Fiz. **116**, 2176 (1999) [JETP **89**, 1180 (1999)].
4. A. P. Baĭkov and A. F. Shestak, Pis'ma Zh. Tekh. Fiz. **5**, 1355 (1979) [Sov. Tech. Phys. Lett. **5**, 569 (1979)].
5. V. M. Gennad'ev, I. V. Zakurdaev, and N. N. Chadaev, Izv. Akad. Nauk, Ser. Fiz. **62**, 2030 (1998).
6. N. M. Kuznetsov, Teplofiz. Vys. Temp. **37**, 1004 (1999).
7. D. A. Boness and J. M. Brown, Phys. Rev. Lett. **71**, 2931 (1993).
8. V. I. Zubov, J. F. Sánchez-Ortiz, J. N. Teixeira Rabelo, and I. V. Zubov, Phys. Rev. B **55**, 6747 (1997).
9. T. A. Mehlhorn, M. P. Desjarlais, T. A. Hail, *et al.*, J. Phys. IV **10** (5), 65 (2000).
10. P. Blinov, A. Chernenko, A. Chesnokov, *et al.*, in *Proceedings of the XIII International Conference on High-Power Beams, Nagaoka, 2000*, p. O-3-4.
11. W. G. Hoover, J. Chem. Phys. **63**, 5434 (1975).
12. W. G. Hoover, S. G. Gray, and K. W. Johnson, J. Chem. Phys. **55**, 1128 (1971).
13. P. R. Levashov, Preprint No. 1-446, Ob"edin. Inst. Vys. Temp. Ross. Akad. Nauk (Russian Research Center Institute of High Temperatures, Russian Academy of Sciences, Moscow, 2000).
14. S. I. Tkachenko, K. V. Khishchenko, V. S. Vorob'ev, *et al.*, Teplofiz. Vys. Temp. **39** (5) (2001) (in press).
15. M. B. Agranat, S. I. Anisimov, and B. J. Makshantsev, Appl. Phys. B: Photophys. Laser Chem. **B55**, 451 (1992).

Translated by V. Bukhanov

Doklady Physics, Vol. 46, No. 7, 2001, pp. 467–472. Translated from Doklady Akademii Nauk, Vol. 379, No. 2, 2001, pp. 181–186.
Original Russian Text Copyright © 2001 by Shevkunov.

PHYSICS

Cluster Mechanism of the Energy Accumulation in a Ball Electric Discharge

S. V. Shevkunov

Presented by Academician A.A. Andreev March 30, 2001

Received February 15, 2001

1. OBSERVATIONAL RESULTS

Experiments on a man-made initiation of a ball-lightning discharge attract attention in the context of employing this phenomenon in technological applications [1]. There are well-known hypotheses that treat this form of discharge as matter with a condensed excited phase (É. Manykin, M. Ozhovan), as a system possessing magnetic self-organization (B. Kadomtsev), as a result of the electromagnetic-field capture into a plasma waveguide (V. Kunin, V. Pleshivtsev, L. Furov), as a consequence of electromagnetic-wave interference, etc. There are also rather exotic hypotheses like V. Korshunov's model, which invokes Dirac magnetic monopoles for the explanation of plasma-ball "pumping" or the "polymer" model (V. Bychkov *et al.*). These hypotheses were reviewed in [2], as well as in monographs [3, 4]. Undeniably, any of the scenarios proposed corresponds to usual atmospheric conditions and is unavoidably accompanied by physicochemical processes in gas, ionization being the most important among them. Ionization necessarily causes ion hydration at sufficiently low temperatures.

The lack of a generally recognized ball-lightning theory is an essential gap in the general gas-discharge theory. The key problem is the energy-accumulation mechanism. Estimates of the energy released in the discharge for its lifetime show that the mechanism cannot be reduced to simple gas heating. At high temperatures, a plasma ball would be of a low density, would be entrained vertically upwards by the Archimedean buoyancy force, and would disintegrate in the presence of turbulent flows caused by its own motion. As observations reveal, the plasma bunch (plasmoid) has a density of the same, or slightly higher, order of magnitude as that of ambient air and the stable spherical shape is a consequence of the positive surface tension at the plasmoid boundary. An excess specific weight of a ball, even in the moderate-heating state, testifies to an elevated average molecular weight of its material. This is indirect evidence of intense clustering. A short but powerful electric-field pulse is undoubtedly required for ball-lightning initiation. Such conditions occur in a linear electric discharge of lightning.

The relatively rare occurrence of ball lightning in the course of a thunderstorm suggests that the coincidence of several conditions is necessary for ball-discharge formation. As a consequence of the requirement of a high degree of ionization in combination with a moderate gas temperature, spontaneous ball-lightning formation is a relatively rare phenomenon. The most favorable prerequisites for ball-discharge initiation are, apparently, realized at the periphery of a powerful linear discharge. A shock acoustic wave is capable of causing fast adiabatic gas expansion and its local cooling. The optimum geometry of a linear-discharge current-conducting channel might be responsible for the local interference amplification of an electromagnetic wave. Apparently, a combination of antinodes for a standing electromagnetic wave and a standing shock acoustic wave composes an origin in which the generation of a ball plasma bunch is most likely to be expected.

Independent measurements of the hydrated-ion content in the atmosphere indicate that the concentration of charged clusters is moderate and does not exceed 10^3 ions/cm^3 under normal conditions. However, in equilibrium with this component, there exists a considerably more abundant fraction of electrically neutral clusters arising from the coalescence of hydrated ions into both ion pairs and coarser clusters. The concentration of such clusters is by 6–7 orders of magnitude higher [5, 6]. The high concentration of the electrically neutral clusters results in the well-known anomalously high atmospheric absorption in the middle part of the infrared region [5]. Laboratory experiments with humid air show [7] that the cluster-component relaxation time is abnormally high and comprises tens of minutes. This fact testifies to cluster stability and a low probability of ion-pair recombination. We can recognize a direct resemblance between the anomalously high absorption in normal atmosphere and a ball electric discharge. Conceptually, these two phenomena have a common

St. Petersburg State Technical University, ul. Politekhnicheskaya 29, St. Petersburg, 195251 Russia

1028-3358/01/4607-0467$21.00 © 2001 MAIK "Nauka/Interperiodica"

basis and differ only in their energy scales. Intense ionization of air occurs in an originating ball lightning. The reverse recombination process proves to be delayed due to ion hydration. Water molecules possess relatively large dipole moments and are primarily drawn into the ion electric field. The ball-lightning lifetime is governed by the slow recombination of hydrated ion pairs. At the same time, a steady concentration of ion pairs is maintained predominantly by both the natural radioactive background and slow thermal ionization.

Virtually all observational data concerning ball electric discharge are obtained from occasional eyewitnesses in natural conditions. Interviews with numerous onlookers [4] suggest that, in spite of the relatively bright luminosity of ball lightning, its temperature is no more than hundreds of absolute degrees; i.e., the glow is not thermal radiation. Abrupt heating and explosion of a ball occur in the case of contact with conductors. The explosion temperature is high enough to cause partial fusion of metal. Based on these and other data, as well as on preliminary estimates of the volume energy density and ion hydration rate, a suggestion was conjectured in [8, 9] that the discharge energy can be accumulated in the ion-pair field. Estimates show that this mechanism makes it possible to construct a consistent quantitative pattern of the phenomenon. In this approach, the most difficult point is the quantitative check of the model with respect to the stability of cluster ions and their complexes.

2. THE QUANTITATIVE CHECK

The tentative estimates of [4, 8, 9] and their comparison with atmospheric spectroscopy data [5–7] cause us to anticipate that ion pairs actually possess a high thermal stability and can serve as energy accumulators in ball discharge. At the same time, the mechanism of this stability at the microscopic level remains to be clarified. The barrier that prevents counterions from mutually approaching each other and recombining should be so significant that the recombination characteristic time would increase by 14–15 orders of magnitude compared to the characteristic time scale of the molecular motion. Calculations made in [10–13] reveal that, under normal conditions, hydrate shells of ions typically consist of a single layer. However, it is unlikely that a single monomolecular layer is a significant obstacle in preventing ions from attaining contact distances with subsequent recombination. The counter motion of ions should be terminated at much longer distances. Based on the observation data, we expect that the forces preventing ions from approaching each other are essentially temperature-dependent. The unstable character of the processes involved is indicative of a rather delicate balance of the opposite factors that slow down the counter motion of counterions. The effect of the electrically neutral component lies at the root of the problem and should be taken into account in detail. Water molecules play a crucial role since they possess the largest dipole moments. We have reproduced the conditions for the motion of counterions in water vapor using computer simulation. The probability density for finding two counterions in a unit volume of water vapor at a temperature T and at a distance R from each other is found to be

$$W(R) = 4\pi R^2 \rho^2 \exp\left(-\frac{\Phi(R)}{k_B T}\right). \quad (1)$$

Here, ρ is the number of ion pairs per unit volume, k_B is the Boltzmann constant, and $\Phi(R)$ is the mean-force potential for interacting ions. The mean-force potential incorporates both the direct interaction of ions and all effects pertaining to their interaction with water molecules. Actually, $\Phi(R)$ represents the average energy of both a cluster consisting of two counterions fixed at a distance R and molecules drawn into the space between ions. This energy is averaged over both molecule positions and ion orientations, the energy of hydrated ions separated by an infinite distance being subtracted from the average energy. For calculating $\Phi(R)$, the centers of two counterions were fixed at a distance R, the ions being able to rotate freely. The system was placed into a gas environment consisting of water molecules at a given pressure p and temperature T so that the number of molecules being drawn into the ion field was not fixed *a priori*. Equilibrium conditions for the thermal and material contact of the system with the environment were simulated by the Monte Carlo method in a Grand Canonical Ensemble. The system was bounded by a spherical cavity 80 Å in diameter. The averaging of the energy, number of drawn-in molecules, and other characteristics was carried out over molecular configurations with the Gibbs equilibrium distribution function $\rho(X)$. For calculating each point in the curve $\Phi(R)$, the Markovian process of a random walk over the space of configurations X consisting of 110 million steps was numerically generated. Each step consists in the translation and rotation of a single molecule, throwing a single molecule into the system or removing it from the system. The first-type steps executed from the configuration X into the configuration Y were executed with the probability

$$\min\left\{\frac{\sin(\theta_Y)}{\sin(\theta_X)}\exp\left(-\frac{U(Y)-U(X)}{k_B T}\right), 1\right\},$$

where θ_X and θ_Y are the Euler angles between the molecule symmetry axis and the Z-axis; $U(X)$ is the configuration potential energy. Steps accompanied by the throw of molecules ($X \longrightarrow Y$) and their removal ($Y \longrightarrow$

X) were performed with probabilities satisfying the principle of detailed balancing:

$$\frac{p(X, Y)}{p(Y, X)} = \frac{\rho(Y)}{\rho(X)}$$

$$= \frac{\frac{1}{n!}(Z_{tr}^{kin})^n (Z_{rot}^{kin})^n \exp\left(\frac{n\mu - U(Y)}{k_B T}\right) d\Omega dV}{\frac{1}{(n-1)!}(Z_{tr}^{kin})^{n-1} (Z_{rot}^{kin})^{n-1} \exp\left(\frac{(n-1)\mu - U(X)}{k_B T}\right)} \quad (2)$$

$$= \frac{d\Omega}{\left(\frac{8\pi^2}{\sigma}\right)} \frac{dV}{V} \frac{V}{n} v_{ref}^{-1} \exp\left(\frac{\mu^c - (U(Y) - U(X))}{k_B T}\right).$$

Here, $d\Omega$ and dV are elementary volumes in the molecule-orientation and molecule-position spaces, respectively;

$$\mu^c \equiv \mu^{conf} - k_B T \ln\left(\frac{\sigma}{8\pi^2}\right),$$

$\mu^{conf}(p, T) = \mu + k_B T \ln(Z_{tr}^{kin} Z_{rot}^{kin} v_{ref})$ is the configuration part of the chemical potential μ;

$$Z_{tr}^{kin} = \left(\frac{h}{\sqrt{2\pi m k_B T}}\right)^{-3} = \frac{1}{\Lambda^3}$$

and

$$Z_{rot}^{kin} = \frac{(2k_B T)^{3/2} (I_1 I_2 I_3)^{1/2} \pi^{3/2}}{h^3}$$

are the results of integration over the translational and rotational moments of molecules, respectively; Λ is the thermal de Broglie wavelength; σ is a molecule rotation-symmetry parameter (equal to 2 for water); v_{ref} is an arbitrary fixed volume specifying the reference level for μ^{conf}; m is the molecule mass; and I_1, I_2, and I_3 are the principal moments of inertia for a molecule. For converting the values of the vapor chemical potential to its pressure, the formulas for ideal gas are employed:

$$\mu^c = k_B T \ln\left(\frac{p}{k_B T} v_{ref}\right). \quad (3)$$

In the atmosphere, there exist various types of ions. Among them, H^+, N_4^+, OH^-, O^{2-}, and CO_4^- ions are the most numerous. In this paper, results of the numerical simulation of clusterization for two types of ions (H^+ and OH^-) are presented. A free proton H^+ produced due to the dissociation of a water molecule is captured by another water molecule to form a hydronium ion H_3O^+. The energy of the attachment of the first water molecule to a proton is anomalously high and comprises 7.18 eV $\approx 280 k_B T$. For subsequent molecules, the attachment energy is much lower: 1.6, 0.97, 0.74, 0.67, 0.57, and 0.51 eV. Because of this fact we consider a H_3O^+ ion to be an integral formation and ignore its negligible dissociation probability in the simulation process. The interaction between ions and water molecules is described by complicated potentials reconstructed on the basis of experimental data on the nucleation free energy for water vapor on ions. The potentials take into account the Coulomb, polarization, exchange, and dispersion interactions, as well as the charge transfer and formation of covalent bonds. Comprehensive information on the potentials is contained in [11–14], and numerical values of the parameters are given in [15]. The molecular interaction is described by the five-center Rahman–Stillinger ST2 potential (see references in [11–15]) supplemented by interactions of dipoles induced in the ion field.

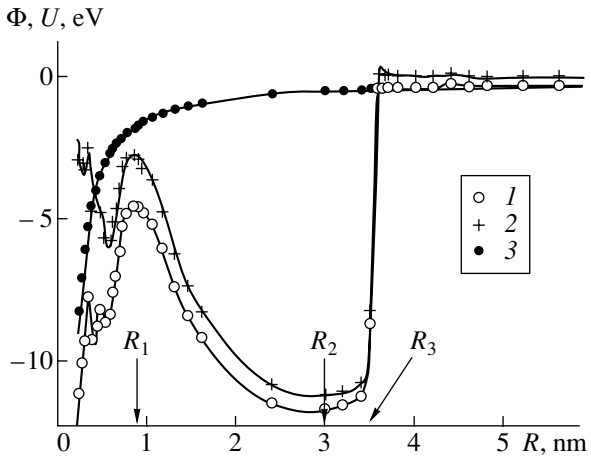

Fig. 1. (*1*) Mean-force potential, (*2*) the energy of interaction between ions and vapor molecules, and (*3*) the energy of direct interactions of OH^- and H_3O^+ ions in water vapor at a temperature of 300 K and a pressure of 2 kPa.

The mean-force interaction potential of counterions in water vapor under normal conditions exhibits a deep minimum at a distance $R_2 = 3$ nm between ions (Fig. 1). The water molecules that are drawn into a strong electric field of the space between ions are responsible for this minimum (Fig. 2). The energy for each drawn-in molecule is reduced by about 0.54 eV = $21 k_B T$. The overall energy decrease due to the formation of a molecular cluster in the space between ions exceeds 11 eV. For comparison, the ion direct-interaction energy at the same distance is only about 0.49 eV (Fig. 1). The ion counter motion is associated with the molecule displacement from the space between ions (Fig. 2) and is energetically unfavorable. The potential barrier developed at a distance $R_1 = 0.8$ nm between ions has a height of about 8 eV = $310 k_B T$ (Fig. 1). The barrier prevents ions from recombining and stabilizes them at a distance on the order of ten molecular radii (Fig. 3). A cluster is highly polarized in the space between ions. If the dipole moment of a two-ion system

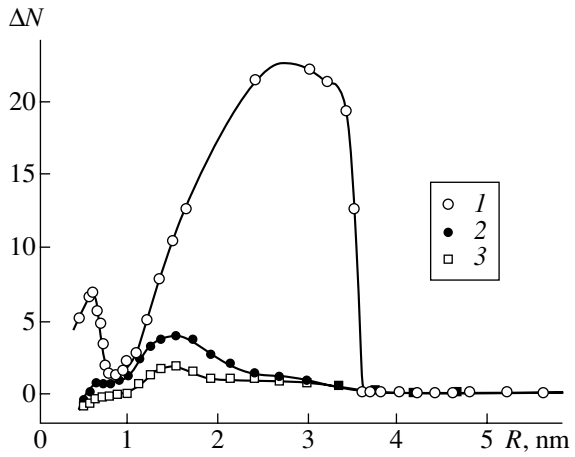

Fig. 2. Number of water molecules drawn into the space between ions as a function of the distance between OH^- and H_3O^+ ions. This number is calculated as the difference between the number of molecules in a cluster and that in hydrate shells of counterions separated from each other by an infinite distance. The vapor temperature in a cluster is (*1*) 300, (*2*) 375, and (*3*) 450 K.

is $P_I = 144$ D at a distance of 3 nm, then the molecular cluster in the space between ions is polarized in the opposite direction and has a mean dipole moment $P_w = -77$D. This is only 30% lower than the theoretical limit corresponding to molecule dipole moments aligned exactly parallel to a straight line connecting the ions. The cluster-polarizability tensor is calculated from the fluctuation theorem. It is a sum of the polarizability owing to the molecule dipole-moment rotation and the intrinsic electric susceptibility $\alpha_w = 1.44 \times 10^{-3}$ nm^3 of a water molecule. The tensor is very anisotropic: the longitudinal (along the straight line connecting the ions) component is larger than the transverse one by about a factor of five. With the intrinsic electric susceptibility taken into account, the longitudinal and transverse components per molecule are 62×10^{-3} nm^3 and 14×10^{-3} nm^3, respectively. They are, correspondingly, 16×10^{-3} nm^3 higher and 32×10^{-3} nm^3 lower than the vapor polarizability. With one longitudinal and two transverse components taken into account, the overall balance in the molecular-component polarizability caused by the vapor clusterization is negative and reaches -17×10^{-3} nm^3 per molecule drawn into the space between ions. This decrease in the polarizability is two orders of magnitude lower than its increase caused by the formation of ion pairs with giant dipole moments. The ion-pair rotational polarizability $\alpha_I^{\text{rot}} = \frac{(P_I + P_w)^2}{3k_B T}$ for $T = 300$ K per drawn-in molecule alone comprises 0.8 nm^3. Despite the drop in the molecular-component polarizability, the ion-pair formation is accompanied by a rise in the total medium polarizability. The increase in the relative permittivity of the medium caused by the ion-pair production is estimated as $\Delta\varepsilon_I > \alpha_I^{\text{rot}} \rho_I = 0.4 \times 10^{-19}\rho_I$, where ρ_I is the number of ion pairs per cubic centimeter. For comparison, the deviation of the vapor permittivity from unity is estimated to be $\Delta\varepsilon_w \approx 0.5 \times 10^{-22}\rho_w \approx 2 \times 10^{-5}$ under the same conditions.

The energy of the ion-pair recombination in vacuum can be reconstructed from the known experimental values for intermediate products:

$$(H_3O)^+ + OH^- \rightarrow H^+ + H_2O + OH^-$$
$$\longrightarrow H + H_2O + OH \rightarrow 2H_2O.$$

The summation yields $U_{\text{rec}} = 9.5$ eV. The energy released in the process of the recombination of two ions

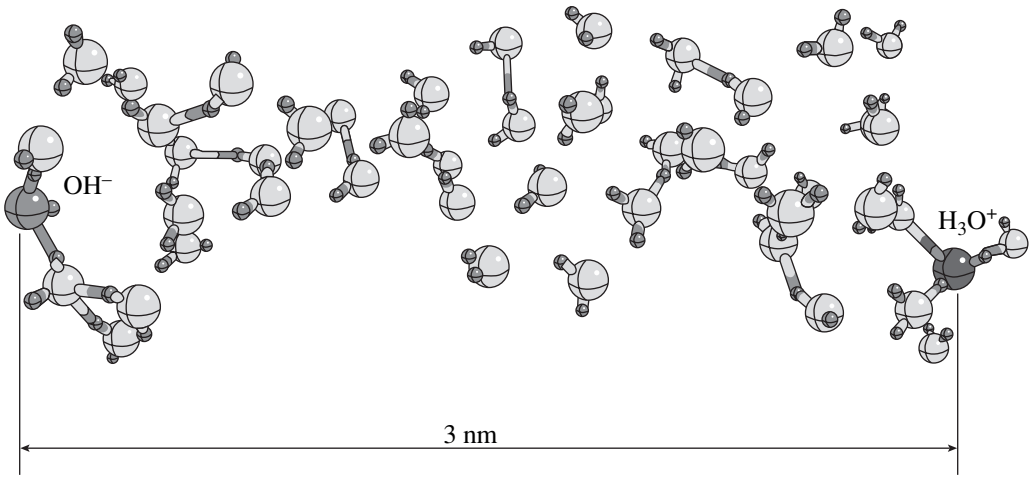

Fig. 3. Example of a configuration for a cluster of water molecules drawn into the space between ions at a temperature of 300 K. The total number of molecules in the system is 47. The ion separation corresponds to the position R_2 in Fig. 1 for the minimum of the mean-force potential.

in water vapor (with the cluster disintegration energy taken into account) is $\Delta E = U_{rec} + U_{cl}$, where U_{cl} is the energy of the cluster production on two counterions. The Monte Carlo calculation shows that $U_{cl} = -23.7$ eV for $T = 300$ K, and the overall balance for the energy ΔE turns out to be negative. At room temperature, recombination in the water vapor does not result in energy release. However, in the case of heating the system to $T = 375$ K, U_{cl} decreases in its absolute value to $U_{cl} = -6.5$ eV at the same vapor pressure. Thus, it attains the value $U_{cl} = -4.9$ eV at $T = 450$ K. In this case, the depth of the stabilizing minimum is reduced to 3.9 eV = $120k_BT$ and 1.8 eV = $46k_BT$, respectively (Fig. 4). The reason for this decrease is a reduction in the number of molecules in the cluster. In this case, the energy released in the recombination of a single ion pair is $\Delta E = 9.5 - 4.9 = 4.6$ eV.

From the data presented, it follows that the plasma-ball temperature must be greater than room temperature by 100–150 K in order for the ion pairs to serve as an energy accumulator. As was observed in natural conditions, this temperature is intrinsic to a plasma ball. As the temperature increases to 100°C, the vapor partial pressure approaches atmospheric pressure and gas-dynamic plasma-ball equilibrium becomes possible, so that vapor completely substitutes for air in the plasma ball. Most likely, the conditions for the initiation of ball lightning include shock local heating and fast evaporation of water drops. Furthermore, all the processes occur in a region almost completely filled with vapor at a temperature close to 383 K at atmospheric pressure. If, as a result of the ionization, the number of ions produced becomes comparable to the number of molecules, then virtually all molecules are drawn into the ion field. The ions for which molecules are deficient will rapidly recombine. If the recombination of a single ion pair results in an energy release on the order of $\Delta E = 5$ eV and the stabilizing cluster consists of $n_{cl} \approx 10$ molecules, then, assuming molecules to be rigid rotators with six degrees of freedom, we obtain the temperature increase that would occur if all ion pairs simultaneously recombined:

$$\Delta T = \frac{\Delta E}{(n_{cl} + 2) \times 3k_B} = 1600 \text{ K}.$$

In this case, the plasma ball will be heated to 383 + 1600 ≈ 2000 K. Shock expansion will occur with the formation of an acoustic wave, which will be perceived as an explosion. Such a temperature is sufficient for causing local burns upon contact with skin. The plasma-ball collapse occurs as a result of the development of an instability: the heating leads to cluster disintegration and acceleration of the recombination, which, in turn, results in further heating.

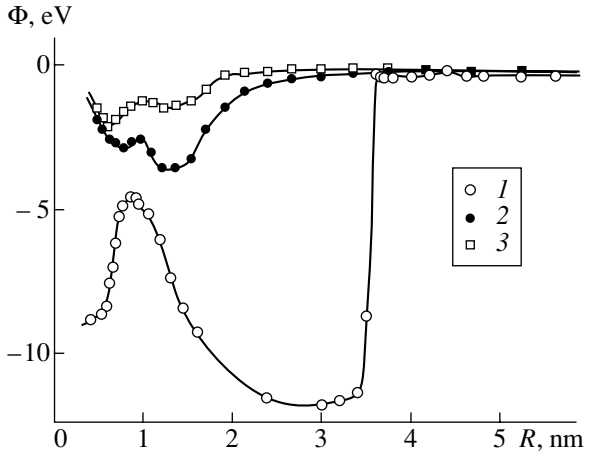

Fig. 4. Mean-force potential for the interaction of OH^- and H_3O^+ ions in water vapor at a pressure of 2 kPa. The vapor temperature in a cluster is (*1*) 300, (*2*) 375, and (*3*) 450 K.

3. CONCLUSIONS

Computer simulation revealed that ion pairs can be present in long-lived prerecombination states under actual conditions existing in the atmosphere. The recombination is prevented not by the hydrate shells, as was expected previously, but by a deep stabilizing minimum formed in the mean-force potential of the interacting counterions. The minimum is produced as a consequence of a strong dependence of the number of molecules drawn into the space between ions on the distance between these ions and is located at a distance on the order of ten molecular radii. The depth of the minimum is sensitive to temperature variation. Even upon heating above room temperature by ~150 K, the minimum virtually disappears and an ion pair recombines with an energy release of a few electron volts.

The cluster mechanism of the energy accumulation in ball lightning makes it possible to explain the observed regularities and construct a consistent quantitative theory of the phenomenon. Cold cluster plasma is produced after the occurrence of a linear electric discharge as a result of molecule dissociation into ions with their subsequent hydration and integration into ion pairs. The slow recombination is accompanied by cold nonequilibrium radiation. A collapse of a long-lived metastable cluster-plasma state with a high concentration of nonrecombined ion pairs is initiated by the Joule heat released at the contact with a conductor. The collapse is accompanied by a chain reaction of energy liberation of recombined ion pairs with subsequent rapid plasma heating to a temperature higher than thousands of degrees, by the formation of a shock wave, and by thermal radiation.

REFERENCES

1. V. N. Kunin, V. S. Pleshivtsev, and L. V. Furov, Teplofiz. Vys. Temp. **35**, 866 (1997).
2. O. A. Sinkevich, Teplofiz. Vys. Temp. **35**, 651 (1997); **35**, 968 (1997).
3. B. M. Smirnov, *The Ball-Lightning Problem* (Nauka, Moscow, 1988).
4. I. P. Stakhanov, *On the Physical Nature of Ball Lightning* (Énergoatomizdat, Moscow, 1985).
5. H. R. Carlon, J. Appl. Phys. **52**, 3111 (1981); **52**, 2638 (1981).
6. H. R. Carlon, Appl. Opt. **20**, 1316 (1981).
7. H. R. Carlon, J. Chem. Phys. **76**, 5523 (1982); **78**, 1622 (1983).
8. I. P. Stakhanov, Zh. Tekh. Fiz. **46**, 82 (1976) [Sov. Phys. Tech. Phys. **21**, 44 (1976)].
9. L. I. Gudzhenko, V. I. Derzhiev, and S. I. Yakovlenko, Tr. Fiz. Inst. Akad. Nauk SSSR **120**, 50 (1980).
10. S. V. Shevkunov, Zh. Éksp. Teor. Fiz. **105**, 1258 (1994) [JETP **78**, 677 (1994)].
11. S. V. Shevkunov and A. Vegiri, J. Chem. Phys. **111**, 9303 (1999).
12. S. V. Shevkunov and A. Vegiri, Mol. Phys. **98**, 149 (2000).
13. A. Vegiri and A. V. Shevkunov, J. Chem. Phys. **113**, 8521 (2000).
14. S. V. Shevkunov, Dokl. Akad. Nauk **356**, 652 (1997).
15. S. V. Shevkunov, Zh. Éksp. Teor. Fiz. **119**, 485 (2001) [JETP **92**, 420 (2001)].

Translated by V. Tsarev

Doklady Physics, Vol. 46, No. 7, 2001, pp. 473–475. Translated from Doklady Akademii Nauk, Vol. 379, No. 3, 2001, pp. 319–321.
Original Russian Text Copyright © 2001 by Borisov.

PHYSICS

Spiral Vortices in a Ferromagnet

A. B. Borisov

Presented by Academician V.E. Zakharov December 25, 2000

Received December 25, 2000

In the last decade, it was experimentally ascertained that structures similar to targets, spiral domains, and domain structures with high translational and orientation ordering are developed from the labyrinth domain structure in thin magnetic films having strong transverse anisotropy (like a "weak axis") provided that these films are subjected to a harmonic or monopolar pulsed magnetic field [1–3]. These guiding centers were observed with the help of the magnetooptical Kerr effect.

Rotating spiral waves and guiding centers are studied in detail in self-oscillatory systems, where they belong to the basic types of dissipative structures [4]. For ferromagnets with uniaxial anisotropy, only low-amplitude nonlinear spiral waves have been described to date [5]; in addition, the stability of the spiral domains in these materials has been proved [6].

In this paper, we treat the spiral domains and targets as defects in magneto-ordered media. We argue that structures similar to spiral vortices in a two-dimensional ferromagnet are formed even under the influence of the basic (exchange) interaction alone. We find a wide class of new exact solutions to the corresponding equations, study the structure and interaction of the spiral vortices, and qualitatively analyze the influence of other interactions on the spiral-vortex structure. The singular behavior of magnetization at the vortex centers is unessential because the vortices originate at nonmagnetic defects.

In the continuous approximation, the steady magnetic structures in a two-dimensional ferromagnet are defined as solutions to the equation

$$\mathbf{M}(\mathbf{r}) \times [\alpha \Delta \mathbf{M}(\mathbf{r}) + \mathbf{H}] = 0, \quad \mathbf{M}^2(\mathbf{r}) = M_0^2, \quad (1)$$

where α is the exchange-interaction constant. The effective magnetic field H is determined by the energy of magnetic anisotropy and by the magnetostatic field. If the field H vanishes, Eqs. (1) coincide with the equations for an n-field ($D = 2$, $N = 3$) and a nematic in the one-constant approximation. Although such equations are integrable and the procedure of their "dressing" is known [7], finding the desired class of their solutions is very difficult.

We now consider a wide class of the solutions provided that the fields $\Phi(x, y)$ and $\theta(x, y)$, entering as parameters in the magnetization vector $\mathbf{M}(x, y) = M_0\{\cos\Phi\sin\theta, \sin\theta\sin\Phi, \cos\theta\}$, can be expressed in terms of the independent functions $a(x, y)$ and $b(x, y)$ as follows:

$$\theta(x, y) = \theta(a(x, y)), \quad \Phi(x, y) = \Phi(b(x, y)). \quad (2)$$

It follows from Eqs. (1) (for $H = 0$) that the fields $\theta(a)$ and $\Phi(b)$ will obey a simple set of the differential equations

$$\theta''(a) = \frac{\sin(2\theta(a))}{2}(\Phi'(b))^2, \quad \Phi''(b) = 0, \quad (3)$$

if the following conditions are satisfied:

$$\partial_u \partial_{\bar{u}} \Omega = \partial_u \Omega \partial_{\bar{u}} \Omega = 0, \quad \Omega = a + ib, \quad u = x + iy = r\exp(i\varphi). \quad (4)$$

It is worth noting that this approach permits a three-dimensional generalization. In this case, after substituting $\theta(x, y, z) = \theta(a)$ and $\Phi(x, y, z) = \Phi(b)$ into Eqs. (3) and choosing an arbitrary function $\Omega(k_1(x + iy) + k_2(x - iy) + k_3 z)$, with the complex-valued parameters k_1, k_2, and k_3 satisfying the dispersion equation $4k_1k_2 + k_3^2 = 0$, we obtain a wide class of exact solutions to Eq. (1) with $H = 0$.

In the two-dimensional case, we choose $\Phi(x, y) = b(x, y)$, without loss of generality, and consider the solutions for $\theta(a)$ taking the form of a mesh of solitons (cnoidal wave):

$$\cos\theta = \sigma\,\mathrm{sn}\left(\frac{a(R, \varphi)}{k}, k\right), \quad \text{with } \sigma = \pm 1, \quad R = \ln r, \quad \text{and} \quad 0 < k < 1. \quad (5)$$

It follows from the uniqueness condition for magnetization that the general solution $\Omega = \Omega(u)$ for a set of mag-

Institute of Metal Physics, Ural Division, Russian Academy of Sciences, ul. S. Kovalevskoĭ 18, Ekaterinburg, 620219 Russia

1028-3358/01/4607-0473$21.00 © 2001 MAIK "Nauka/Interperiodica"

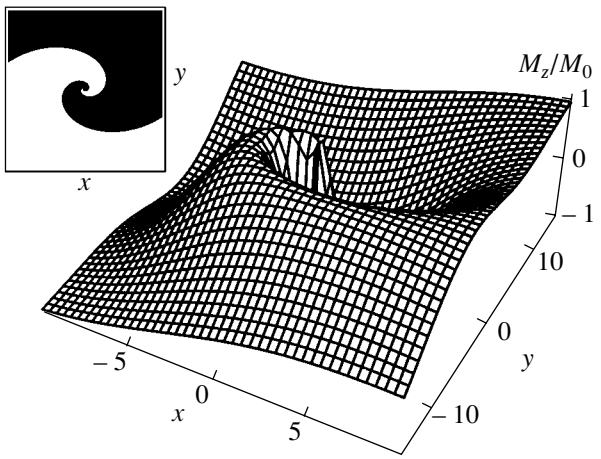

Fig. 1. Structure of the core for a one-turn spiral ($N = 1$) with $k = \frac{1}{2}$ and $Q = 1$ ($r_0 = 1$). The domains with positive (white region) and negative (black region) values of M_z are shown in the inset. The angular twist of the spiral domain increases with decreasing k.

netic defects centered at the points u_j takes the form

$$\Omega = a + ib = \sum_j^n \left(\frac{2ikK}{\pi}N_j + Q_j\right)\ln(u - u_j) + w(u), \quad (6)$$
$$N_j, Q_j \in Z,$$

where $w(u)$ is an arbitrary meromorphic function. This solution is defined by $4n + 3$ parameters [if $w(u) = \text{const}$] and describes both the structure and interaction of the magnetic defects. For $N_j = 0$ ($j = 1, 2, \ldots, n$) and $k = 1$, the complex-valued field $\cot\left(\frac{\theta}{2}\right)\exp(i\Phi)$ is reduced to $\exp(\Omega)$, while solution (5), (6) coincides with the well-known multi-instanton Belavin–Polyakov solution [8]. For the fields of the nematic director, the number N can take half-integer values. In hydrodynamics, the function Ω given by (6) with $w(u) = \text{const}$ is a sum of the complex-valued flow potentials for the vorticity sources.

An isolated magnetic defect with discrete parameters σ, $N \neq 0$, and Q represents a spiral vortex. In this case, the magnetization-vector component perpendicular to the film plan and the azimuthal angle are given, respectively, by

$$M_z = M_0\sigma\,\mathrm{sn}\left(\frac{Q\ln(r/r_0)}{k} - \frac{2K(k)}{\pi}(\varphi - \varphi_0)N, k\right) \quad (7)$$

$$\Phi = Q(\varphi - \varphi_0) + \frac{2kK(k)}{\pi}N\ln\frac{r}{r_0}. \quad (8)$$

For $N = 1$, solution (7) represents two spiral domains, with their magnetization vectors oppositely directed and two logarithmic spirals separating them (Fig. 1). For an arbitrary N, Eq. (7) describes an N-turn logarithmic spiral whose chirality (i.e., the direction of angular twist) is defined by the sign of N. The field $M_z(x, y)$ and the configuration of a two-turn spiral domain are shown in Fig. 2. The case $N = 0$ corresponds to a set of concentric (with respect to the variable R) ring-shaped domains, i.e., to a magnetic target coinciding with an instanton solution in the limit $k \longrightarrow 1$.

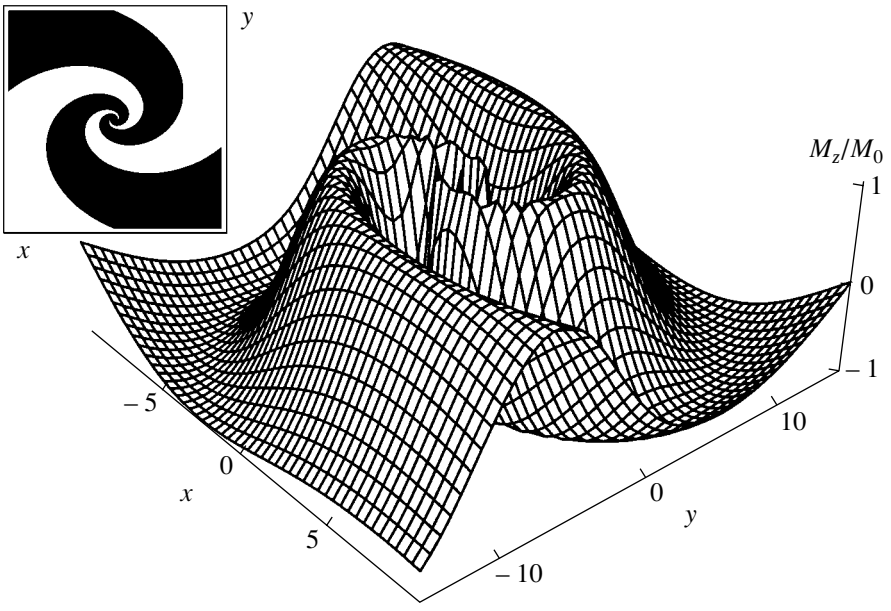

Fig. 2. Structure of a two-turn spiral with $k = \frac{1}{6}$, $Q = 1$, and $N = 2$.

The energy W of a spiral vortex, like the energy of other similar nonlocalized structures (dislocations and disclinations), depends logarithmically on the size of the system L and the radius of the vortex core d. In thin magnetic films, the latter is equal to the radius of the nonmagnetic defects at which the magnetic spirals and targets originate.

Equations (1) with a nonvanishing field **H** are not scale invariant. In this case, the exchange interaction determines the structure of a spiral vortex only in the neighborhood of its center. Spirals and targets are observed, in particular, in films having large quality factors when the magnetostatic field can be neglected as compared to the magnetic-anisotropy field $\mathbf{H} = \beta\mathbf{n}(\mathbf{nM})$, with $\mathbf{n} = (0, 0, 1)$ and $\beta > 0$. In this case, the magnetization vector of a spiral vortex at large distances from its center tends to a uniform ground state [$\theta(x, y) \longrightarrow m\pi$, $m \in Z$]. For an isolated spiral vortex, the self-similar solution defined by formulas (7) and (8) is adequate only at distances $r < l = \sqrt{\alpha/\beta}$. At larger distances ($r \gg l$), the domain boundary spreads and one of the spiral domains dissipates even if the external magnetic field is weak. Numerical calculations show that the structure of a magnetic target can be described by a solution given by (7) and (8) with $N = 0$ when the modulus $k = k(r)$ is considered r-dependent. At distances smaller than the magnetic length l, the quantity k remains constant and rapidly tends to unity for $r \gg l$. In this case, the asymptotic value m (i.e., the number, measured to $r = l$, of the ring-shaped domains) is uniquely defined by the numerical value of $k(r)|_{r \to 0}$. The radius of the last ring increases when this limiting value is decreased.

In contrast to the multi-instanton solutions, the energy of multivortex solution (5) and (6) with $k \neq 1$ depends on the distances between the centers of the spiral vortices; this results in their interaction. The interaction of two vortices with the parameters (N, Q) and $(-N, -Q)$ is attractive, i.e., $\theta \longrightarrow \frac{\pi}{2}$ as $r \longrightarrow \infty$. The energy of such a localized dipole is independent of the size L of the system (the energy density is inversely proportional to r^4). This feature suggests that such dipoles may contribute to the thermodynamical properties of two-dimensional magnets. The interaction of two spiral vortices with the parameters (N, Q_1) and $(-N, Q_2)$ is also attractive because the corresponding solution at large distances turns into a target with the parameters $(0, Q_1 + Q_2)$.

ACKNOWLEDGMENTS

This study was supported in part by the Russian Foundation for Basic Research, project no. 00-01-00366 and the INTAS grant no. 99-1782.

REFERENCES

1. G. S. Kandaurova, Pis'ma Zh. Eksp. Teor. Fiz. **47**, 410 (1988) [JETP Lett. **47**, 490 (1988)].
2. G. S. Kandaurova, Dokl. Akad. Nauk **331**, 428 (1993) [Phys. Dokl. **38**, 342 (1993)].
3. I. E. Dikshteĭn, F. V. Lisovskiĭ, U. G. Mansvetova, and E. S. Chizhik, Zh. Eksp. Teor. Fiz. **100**, 1606 (1991) [Sov. Phys. JETP **73,** 888 (1991)].
4. M. C. Cross and H. C. Hohenberg, Rev. Mod. Phys. **65**, 851 (1993).
5. A. B. Borisov, V. A. Feĭgin, and B. N. Filippov, Fiz. Tverd. Tela (Leningrad) **33**, 2316 (1991) [Sov. Phys. Solid State **33**, 1304 (1991)].
6. A. B. Borisov and Yu. I. Yalyshev, Fiz. Met. Metalloved. **79**, 18 (1995).
7. S. Novikov, S. V. Manakov, L. P. Pitaevskii, and V. E. Zakharov, *Theory of Solitons: The Inverse Scattering Method* (Nauka, Moscow, 1980; Consultants Bureau, New York, 1984).
8. A. A. Belavin and A. M. Polyakov, Pis'ma Zh. Eksp. Teor. Fiz. **22**, 503 (1975) [JETP Lett. **22**, 245 (1975)].

Translated by V. Chechin

Doklady Physics, Vol. 46, No. 7, 2001, pp. 476–480. Translated from Doklady Akademii Nauk, Vol. 379, No. 1, 2001, pp. 42–46.
Original Russian Text Copyright © 2001 by Zelkin, Kravchenko, Pustovoĭt.

TECHNICAL PHYSICS

Synthesis of Directivity Patterns for Nonequidistant Antenna Arrays by Means of Atomic Functions

E. G. Zelkin*, V. F. Kravchenko*, and Corresponding Member of the RAS V. I. Pustovoĭt**

Received January 16, 2001

In this paper, we present results which considerably extend the field of solutions to problems of aerial-array synthesis. These results are obtained by employing a devised and justified method of auxiliary functions. As such, the atomic functions (AF) [1–10] employed in solving synthesis problems are successfully used.

STATEMENT OF THE PROBLEM

Two types of aerial arrays are known [11]: equidistant or nonequidistant arrays with regularly or irregularly spaced radiating elements, respectively. In the first case, for a linear array, the directivity pattern is of the form

$$R(u) = \sum_{p=1}^{N} A(pd)e^{ipdu}, \quad p = 1, 2, \ldots, N, \qquad (1)$$

where $u = k\sin\theta\cos\varphi$ is a generalized coordinate related to the angles θ and φ of a spherical coordinate system and d is the spacing between the array elements. In the second case, we have

$$R(u) = \sum_{p=1}^{N} A(s_p)e^{is_p u}. \qquad (2)$$

Here, $A(y)$ is the amplitude–phase current distribution throughout the radiating elements, $s_p = \frac{2\pi}{\lambda}x_p$ is the relative coordinate of the pth element, λ is the wavelength, and N is the number of radiating elements of the array. Methods for solving (1) and (2) are different and call for separate investigations.

Directivity patterns exactly represented in form (1) or (2) are referred to as realizable and are denoted by B'_σ, as opposed to the directivity-pattern class of linear radiating elements denoted by W_σ: $R(u) \in W_\sigma$.

METHOD OF SOLVING THE PROBLEM

In the synthesis problems considered below, $R(u)$ are given functions. The amplitude–phase distributions $A = A(x_p)$ are to be found; they take N independent values corresponding to the number of radiating elements and their positions at the points x_n.

Consequently, if a given directivity pattern belongs to realizable directivity patterns, then the synthesis problem reduces to the consideration of (1) or (2), depending upon its conditions. If $R(u)$ does not belong to functions of the classes W_σ or B'_σ, it should be approximated, in line with [11], by using an auxiliary function. As a result, the product of this function and a given directivity pattern can be represented in the form of a function of the class W_σ. Thus, it is represented as a directivity pattern of a continuous radiating element. Then,

$$R(u)U_m(u) = \frac{1}{2\pi}\int_{-\pi}^{\pi} A(y)e^{iuy}dy. \qquad (3)$$

It is well known that the solution to Eq. (3) is expressed in terms of the Fourier integral

$$f(y) = \int_{-\infty}^{\infty} R(u)U_m(u)e^{-iuy}du. \qquad (4)$$

We state the following theorem.

Theorem. *If a directivity pattern can be represented as a product of two functions $R(u) = R_1(u)\cdot R_2(u)$, where $R_1 \in B'_\sigma$, and $R_2(u) \in W_\sigma$, then the Fourier transform takes the form*

$$f(y) = \begin{cases} \sum_{p=1}^{N} A(s_p) f_2(y - s_p), & -\sigma + s_p < y < \sigma + s_p \\ 0 \quad \textit{outside these intervals.} \end{cases} \qquad (5)$$

* *Institute of Radio Engineering and Electronics, Russian Academy of Sciences, ul. Mokhovaya 18, Moscow, 103907 Russia*

** *Central Design Bureau of Unique Instrumentation, Russian Academy of Sciences, ul. Butlerova 15, Moscow, 117342 Russia*

1028-3358/01/4607-0476$21.00 © 2001 MAIK “Nauka/Interperiodica”

Here,

$$A(s_p) = \sum_{n=-\infty}^{\infty} R_1(n)e^{ins_p}, \quad s_p < \sigma_1,$$

$$f_2(y) = \sum_{n=-\infty}^{\infty} R_2(n)e^{iny} = \int_{-\infty}^{\infty} R_2(u)e^{iuy}du,$$

$$y < \sigma_2, \quad \sigma \le \sigma_2 + \sigma_1.$$

Proof. By substituting $R_1(u)$ and $R_2(u)$ into (4), we obtain

$$f(y) = \int_{-\infty}^{\infty} R_1(u) \cdot R_2(u)e^{-iuy}du.$$

Since $R_1 \in B'_\sigma$ and $R_2(u) \in W_\sigma$, we represent them in the following form:

$$R_1(u) = \sum_{p=1}^{N} A(s_p)e^{is_p u}, \quad s_p < \sigma_1,$$

$$R_2(u) = \frac{1}{2\pi}\int_{-\pi}^{\pi} f_2(y)e^{iuy}dy = \sum_{n=-\infty}^{\infty} R(n)e^{iny},$$

$$y < \sigma_2, \quad \sigma_1 + \sigma_2 \le \sigma.$$

Consequently,

$$f_2(y) = \sum_{p=1}^{N} A(s_p)\int_{-\infty}^{\infty} R_2(u)e^{iu(s_p - y)}du$$

$$= \sum_{p=1}^{N} A(s_p) f_2(y - s_p).$$

We now apply the theorem for the solution to Eq. (4). The Fourier transform of an atomic function is used as an auxiliary function:

$$F(u) = \int_{-1}^{1} \mathrm{up}(y)e^{iuy}dy. \tag{6}$$

Substituting $F(u)$ for $U_m(u)$ in (4) and taking (5) into account, we obtain

$$f(y) = \sum_{p=1}^{N} A(s_p)\int_{-\infty}^{\infty} F(u)e^{-iu(s_p - y)}dy$$

$$= \sum_{p=1}^{N} A(s_p)\mathrm{up}(y - s_p).$$

We consider the last expression in more detail.

The function up(y) has a bell-shaped form, and up($y - s_p$) = up(0) = 1 at the points $y = s_p$. With increasing $|y|$, up(y) decreases and is zero at the points $y = \pm 1$.

By squeezing the function $\mathrm{up}\left(\frac{y}{a}\right)$ ($a < 1$), we can manage that it approaches zero for small $|y|$, thus tending to the Dirac delta-function. In this case, all up($y - s_p$), with $|y|$ not equal to s_p, will be close to zero and this allows us to set $A(s_p) = f(s_p)$. Then, it follows that

$$R(u) = \sum_{p=1}^{N} f(s_p)e^{is_p u}. \tag{7}$$

The function $f(y)$ is known; it is determined from solution (4). Therefore, if the coordinates s_p of the radiating elements are found, the current in the pth radiating element is determined by the value of the function $f(y)$ at the point $y = s_p$.

Thus, if the coordinates of radiating elements for an aerial array are specified, then, using formulas (4) and (5), we can determine the currents in the radiating elements. If s_p are not specified and are to be determined, the synthesis problem becomes more involved. However, after performing certain mathematical operations, we arrive at the following results. Differentiating (7) with respect to u, we obtain

$$\frac{\partial R}{\partial u} = \sum_{p=1}^{N} A(s_p)is_p e^{is_p u}. \tag{8}$$

Next, we multiply (8) by $F(u)e^{iuy}$ and integrate from $-\infty$ to ∞:

$$\int_{-\infty}^{\infty} \frac{\partial R(u)}{\partial u}F(u)e^{-iuy}du = f_2(y). \tag{9}$$

Substituting (8) into (9), we have

$$f_2(y) = \sum_{p=1}^{N} A(s_p)is_p \int_{-\infty}^{\infty} F(u)e^{i(s_p - y)u}du$$

$$= \sum_{p=1}^{N} A(s_p)is_p \mathrm{up}(s_p - y).$$

Since up($s_p - y$) = 1 at the points $s_p = y$, then $A(s_p)is_p = f_2(s_p)$.

Because $A(s_p) = f_1(s_p)$, the following equation holds, whose solutions allow the positions s_p of the radiating

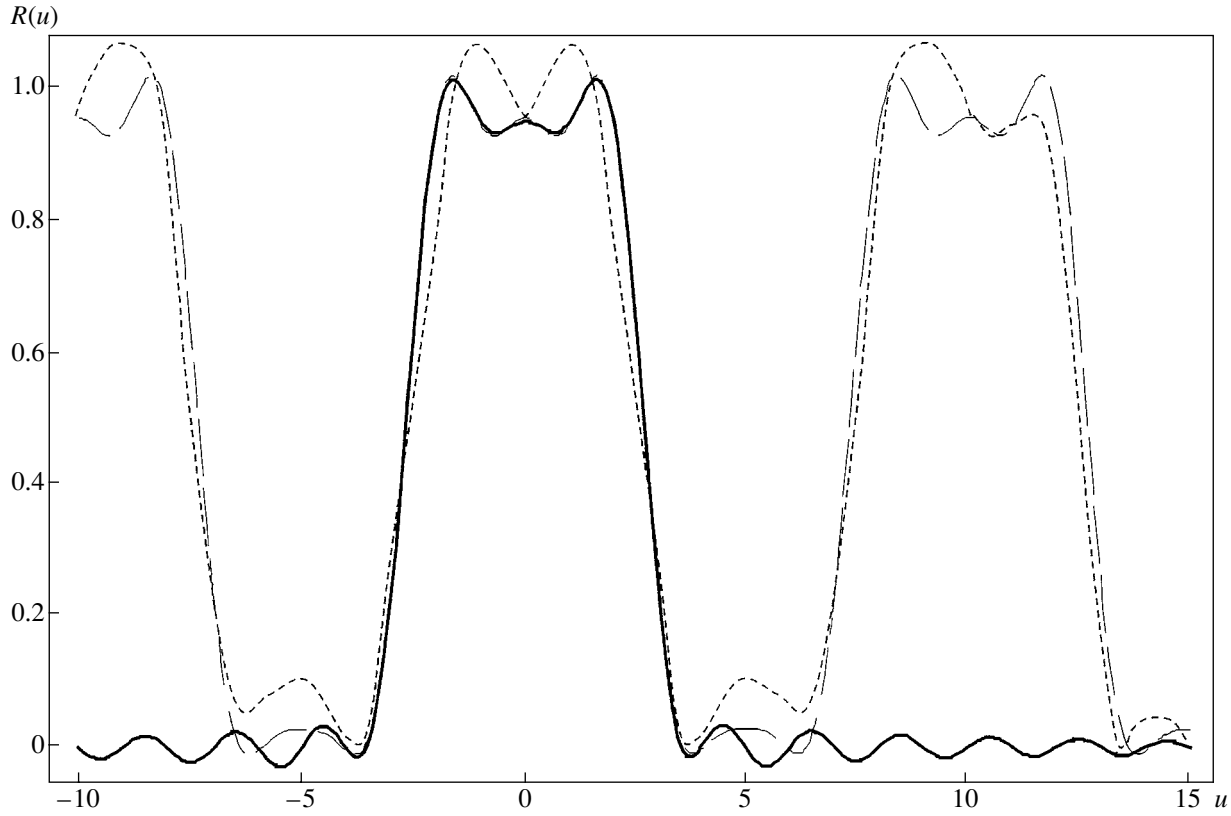

Fig. 1. Sector directivity pattern.

elements to be determined:

$$is_p f_1(s_p) = f_2(s_p). \tag{10}$$

The functions $f_1(y)$ and $f_2(y)$ are given by formulas (4) and (9); therefore, s_p are determined from the roots of Eq. (10) using numerical methods. Since s_p are real values, the functions $f_1(s_p)$ and $f_2(s_p)$ can differ in phase only by $\pm\frac{\pi}{2}$. It is worth noting that Eq. (10) has an exact solution only if $f_1(y)$ and $f_2(y)$ are determined from relations (4) and (9), where $R(u) \in B'_\sigma$. Provided that $R(u)$ does not belong to these functions, formula (10) does not allow the required solution to be found. Consequently, if $R(u) \notin B'_\sigma$, $R(u)$ should be initially approximated, with a given accuracy, by a function of the class B'_σ, and next, after solving Eq. (10), all the positions s_p of the radiating elements should be determined. Evidently, when solving the synthesis problem for nonequidistant aerial arrays (as well as for a linear radiating element), the central difficulty is related to the approximation of a given directivity pattern by the functions B'_σ (or by functions of the class W_σ in the case of a linear radiating element). It is well known that the simplest function belonging to the class B'_σ is a finite Fourier series; this was successfully used to approximate a given directivity pattern using such functions.

NUMERICAL SIMULATION

We now illustrate the proposed procedure using particular examples.

Example 1. It is required that a sector directivity pattern be obtained through the use of a nonequidistant aerial array. We specify this pattern in the following form:

$$R(u) = \frac{\sin\pi u}{\pi u}\frac{36 + 7u^2 + 5.5u^4 - 0.5u^6}{(1-u^2)(4-u^2)(9-u^2)}. \tag{11}$$

The behavior of function (11) is shown in Fig. 1 by the solid curve. This function belongs to the class W_σ and can be exactly evaluated by the use of a linear radiating element. However, in order to construct such a function by employing an array, an approximation of a Fourier series partial sum is required. We restrict ourselves to six terms of this series:

$$\begin{aligned} R(u) &= \frac{A_0}{2} + \sum_{n=1}^{m} A_n \cos\frac{n\pi u}{l}, \\ A_n &= \int_{-l}^{l} R(u)\cos\frac{n\pi u}{l}du. \end{aligned} \tag{12}$$

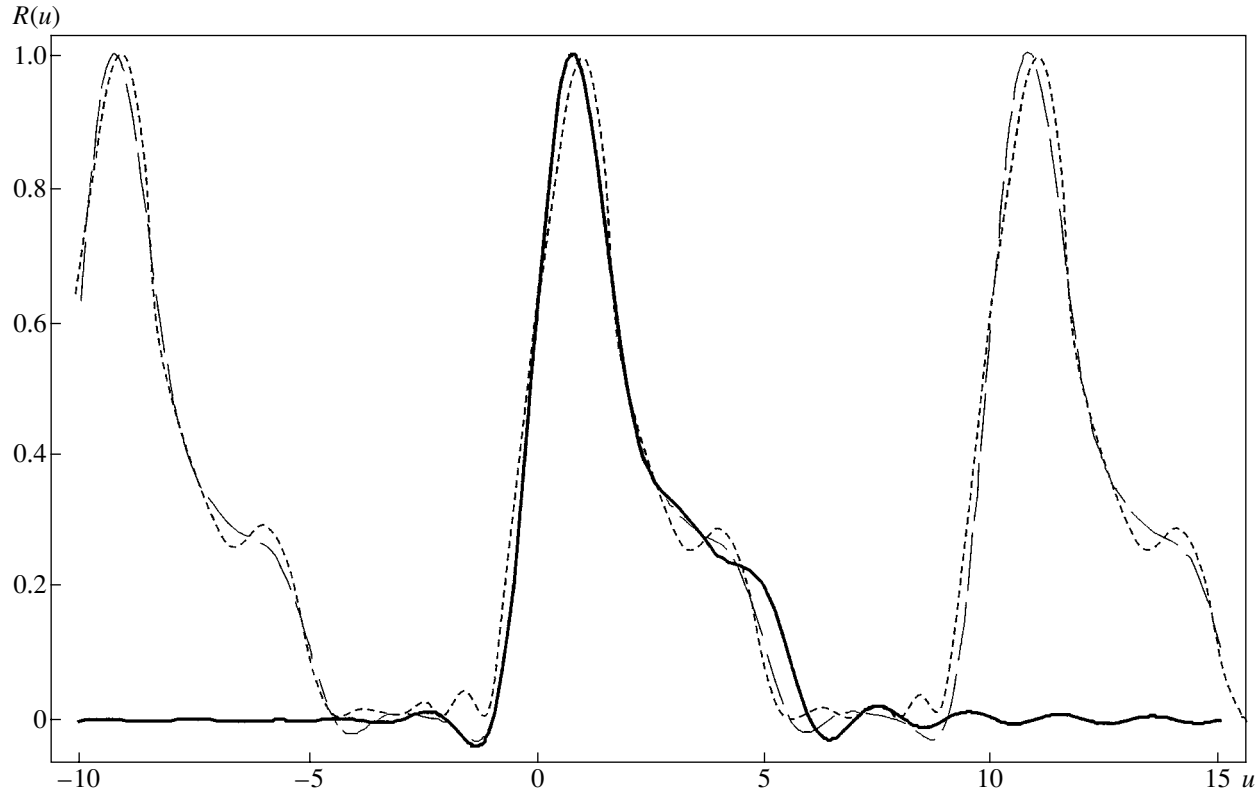

Fig. 2. Directivity pattern of the cosecant type.

Here, the atomic function contraction coefficient $a = 0.3$, $l = 5$, and $m = 5$. Substituting (12) into (4) and (9), we determine the functions $f_1(y)$ and $f_2(y)$. Then, using the values of $f_1(y)$ and $f_2(y)$ obtained, we numerically find the values of s_p from formula (10). Next, in the function $f_1(y)$, we substitute these values for y, thus finding the current amplitudes in the radiating elements. Finally, the directivity pattern of the array is determined from formula (2). The calculated physical parameters and numerical results are listed in Table 1. The broken line in Fig. 1 is a directivity pattern; hence, the approximation to the given directivity pattern is seen to be good.

The sector directivity pattern is produced by a symmetrical current distribution, which ranges, with substantial oscillations, from 0.03 to 0.15 at the edges and attains unity at the center. In this case, the phase ranges from 0 up to 180°. The side lobes are not greater than 6–7%. Such small values are due to the use of the auxiliary atomic function.

Example 2. It is necessary to obtain a directivity pattern of the cosecant type, which is given in the following form:

$$R(u) = \frac{\sin\pi u}{\pi u} \times \frac{u^5 - 7.5u^4 - 5u^3 + 187.5u^2 - 581u + 585}{7.5(u-1)(u-2)(u-4)(u-5)}. \quad (13)$$

The given directivity pattern is plotted in Fig. 2 by the solid line, and it does not belong to the functions of the class B'_σ. Therefore, it will be approximated by a partial sum of the Fourier series. Since the directivity pattern is asymmetric, it is approximated by a finite Fourier cosine and sine series. We restrict ourselves to five terms of this series:

$$R(u) = \frac{A_0}{2} + \sum_{n=1}^{m}\left(A_n\cos\frac{n\pi u}{l} + B_n\sin\frac{n\pi u}{l}\right),$$

$$A_n = \int_{-l}^{l} R(u)\cos\frac{n\pi u}{l}du, \quad B_n = \int_{-l}^{l} R(u)\sin\frac{n\pi u}{l}du,$$

$$l = 5, \quad m = 5.$$

The calculated physical characteristics for the cosecant directivity pattern are listed in Table 2. The synthesized directivity pattern constructed from these data is indicated in Fig. 2 by the broken line.

Thus, the cosecant-type directivity pattern [formula (13)] is constructed with the use of a nonequidistant array having 12 elements. The current amplitudes of the array fall off to the edges with certain oscilla-

Table 1. Physical parameters and numerical results for the Example 1

s_p	−2.524	−1.852	−1.341	−1.185	−0.638	0.000	0.638	1.185	1.341	1.852	2.524
$A(s_p)$	0.378	0.1550	0.0508	0.622	0.5501	1.000	0.5501	0.0622	0.0508	0.155	0.378
$\varphi(s_p)$, deg	180	360	0.000	360	180	180	180	0.0	360	0.0	180

Table 2. Calculated physical characteristics for the cosecant-type directivity pattern

s_p	−3.172	−2.534	−1.891	−1.263	−0.628	−0.297	0.0	0.297	0.628	1.263	1.891	2.534
$A(s_p)$	0.0460	0.0753	0.2633	0.3179	0.6812	0.0341	1.0	0.0341	0.6812	0.3179	0.2633	0.736
$\varphi(s_p)$, deg	100.2	86.4	77.88	59.0	52.8	200.8	360	159.2	307.2	301.0	282.2	273.2

tions, attaining unity at the center; their phases range from 50 to 360°.

CONCLUSIONS

In this paper, a new method for calculating directivity patterns of nonequidistant aerial arrays is proposed and justified that can be employed for designing arrays in a wide microwave range. The results were reported in part at the Second International Conference "Actual Problems of Computing Physics" (July 24–29, 2000, Dubna, Russia) [12].

ACKNOWLEDGMENTS

The authors are grateful to Academician of the National Academy of Sciences of Ukraine V.L. Rvachev, Corresponding Member of the Russian Academy of Sciences L.D. Bakhrakh, Professor Ya.S. Shifrin for discussion of the results, and to A.E. Tumanskaya for the analysis of the numerical experiment.

REFERENCES

1. V. F. Kravchenko and V. V. Timoshenko, Élektromagn. Volny Élektron. Sist. **4** (5), 21 (1999).
2. V. F. Kravchenko, Zarubezhn. Radioélektron. Usp. Sovrem. Radioélektron., No. 8, 23 (1996).
3. V. F. Kravchenko and V. A. Rvachev, Zarubezhn. Radioélektron. Usp. Sovrem. Radioélektron., No. 8, 6 (1996).
4. E. G. Zelkin and V. F. Kravchenko, *Antennas*, 1999, No. 2 (43), p. 46.
5. V. F. Kravchenko, in *Proceedings of the III International Conference on Antenna Theory and Techniques, Sevastopol, 1999*, p. 55.
6. V. F. Kravchenko, E. G. Zelkin, and V. V. Timoshenko, in *Proceedings of the III International Conference on Antenna Theory and Techniques, Sevastopol, 1999*, p. 124.
7. E. G. Zelkin, V. F. Kravchenko, V. I. Pustovoĭt, and V. V. Timoshenko, Dokl. Akad. Nauk **371**, 42 (2000) [Dokl. Phys. **45**, 97 (2000)].
8. E. G. Zelkin, V. F. Kravchenko, V. I. Pustovoĭt, and V. V. Timoshenko, Dokl. Akad. Nauk **374**, 35 (2000) [Dokl. Phys. **45**, 449 (2000)].
9. E. G. Zelkin, V. F. Kravchenko, V. I. Pustovoĭt, and V. V. Timoshenko, Antenny, No. 1 (44), 63 (2000).
10. M. A. Basarab, V. F. Kravchenko, V. I. Pustovoĭt, and V. V. Timoshenko, Dokl. Akad. Nauk **374**, 324 (2000) [Dokl. Phys. **45**, 457 (2000)].
11. E. G. Zelkin and V. G. Sokolov, *Synthesis Methods of Antennas* (Sov. Radio, Moscow, 1980).
12. V. F. Kravchenko, in *Proceedings of the II International Conference on Modern Trends in Computational Physics, Dubna, 2000*, p. 106.

Translated by V. Tsarev

Doklady Physics, Vol. 46, No. 7, 2001, pp. 481–483. Translated from Doklady Akademii Nauk, Vol. 379, No. 1, 2001, pp. 47–49.
Original Russian Text Copyright © 2001 by Semenov.

TECHNICAL PHYSICS

Determination of the Plastic-Deformation Zone in Viscoplastic Elastic Materials

Ya. S. Semenov

Presented by Academician V.P. Larionov January 15, 2001

Received January 15, 2001

INTRODUCTION

While studying relaxation phenomena in viscoplastic elastic materials, these phenomena are usually considered as occurring in continuum with mechanical properties occupying the intermediate place between elastic solid bodies and viscous liquids. Therefore, the work of external forces is partially accumulated, spent for destruction, and liberated in the form of heat [1–3].

Usually, the heat dissipation occurs in the plastic-deformation zone, attaining its maximum in the separation zone. This yields a basis for the investigation and determination of the size of the plastic-deformation zone with the help of an infrared imager. The determination as a result of mechanical tests of the plastic-deformation zone for smooth specimens and those having stress concentrators is associated with certain difficulties [3, 4]. Exact determination of the plastic-deformation zone with various stress concentrators would make it possible to calculate the energy spent for the failure, accumulation, and heat release, and also to evaluate the J integral using theoretical calculations.

EXPERIMENTAL METHOD

It is well known [1–3] that under deformation, structural materials release a substantial amount of heat. However, under plastic deformation, polymeric structural materials release a minor amount of heat. Therefore, to check the accuracy of the method employed, specimens cut from PEVP polymeric material according to the GOST-112626-80 were taken for investigations.

Rupture tests were performed using the Instron-195 testing machine with a velocity of clamp motion of 100 mm/min. Two types of specimens were tested, namely, a smooth specimen and a specimen with a sharp notch.

Institute of Physicotechnical Problems, North, Siberian Division, Russian Academy of Sciences, Yakutsk, 677890 Russia

Measurements of the plastic deformation zone were carried out with the help of a Thermovision-650 infrared imager, which possesses the following characteristics: the sensitivity is 0.1°C; the operation-temperature range is 10 to 200°C.

The temperature was continuously measured in the process of specimen deformation up to complete failure, which yields the dynamics of temperature variation with specimen extension.

The measurement and calculation of the temperature and other parameters in the plastic-deformation zone were made with the help of an IBM PC connected to an infrared imager. The IBM PC processes the specimen thermal image and simultaneously saves the specimen parameters. These parameters are the specimen ordinal number, the temperature scale, the values of the maximum and minimum temperature at given points, the date and time, the segment in the plastic-deformation zone (a is the segment with an elevated temperature), and, finally, the temperature-distribution plot along the specimen length.

In addition to these data, we constructed diagrams related to the operation of the Instron-195 testing machine, i.e., loading-time and extension-time diagrams, as well as to the specimen size according to the GOST-11262-80. These data make it possible to calculate the plastic-deformation zone and the energy spent for the specimen failure.

THE RESULTS OF THE EXPERIMENT

Typical results of these tests are shown in Figs. 1 and 2. Figure 1 corresponds to a smooth specimen with the standard dimensions required by the GOST-11262-80.

As should be expected, we observe, in the plastic-deformation zone, a noticeable elevation of the temperature (a is the zone length and b and h are the specimen width and thickness, respectively). These data allow us to rapidly determine with sufficient accuracy the dissi-

1028-3358/01/4607-0481$21.00 © 2001 MAIK “Nauka/Interperiodica”

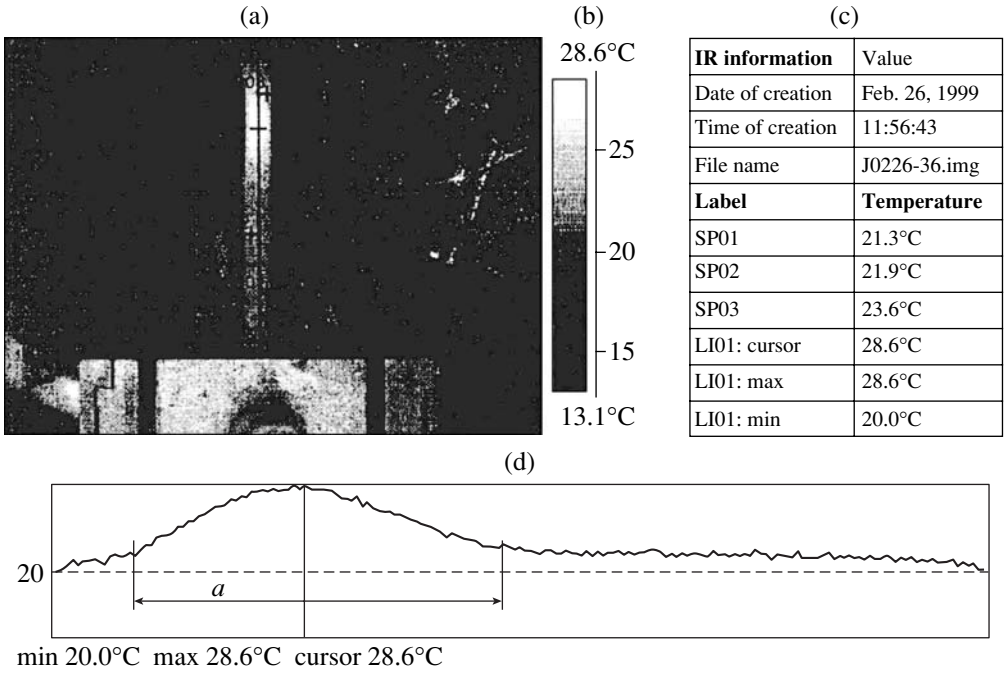

IR information	Value
Date of creation	Feb. 26, 1999
Time of creation	11:56:43
File name	J0226-36.img
Label	**Temperature**
SP01	21.3°C
SP02	21.9°C
SP03	23.6°C
LI01: cursor	28.6°C
LI01: max	28.6°C
LI01: min	20.0°C

Fig. 1. Smooth specimen. Here, as in Fig. 2, (a) thermal image of a specimen; (b) temperature scale; (c) table with the date, time, file name, labels, and temperatures; and (d) the temperature distribution along the specimen length are presented (*a* is the length of the plastic-deformation zone). The temperature of the ambient air is 21.2°C.

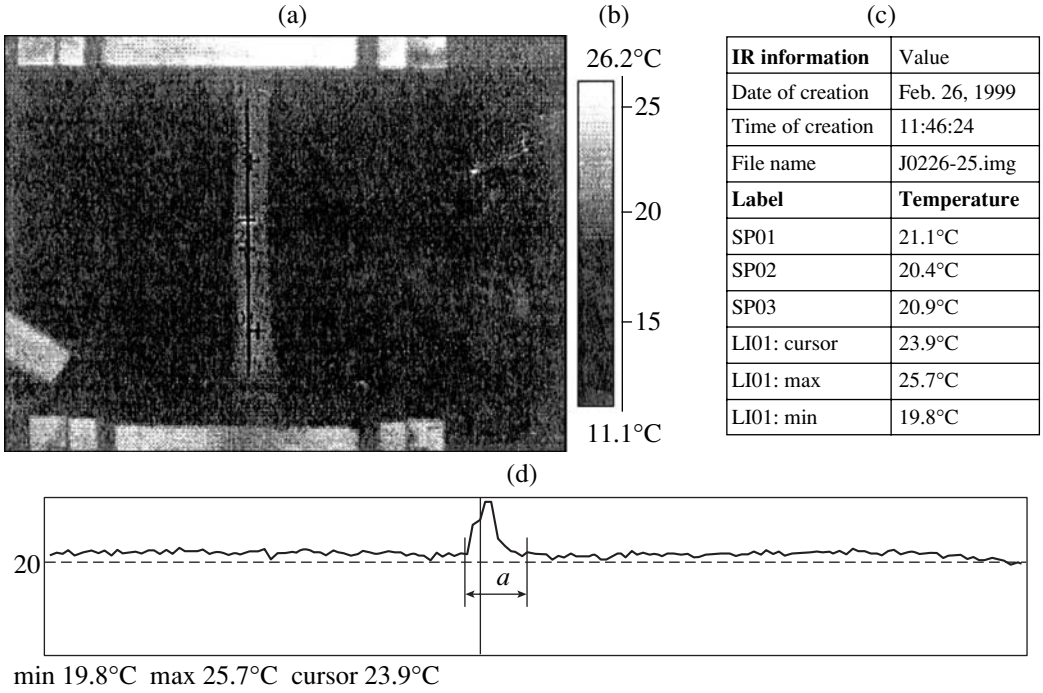

IR information	Value
Date of creation	Feb. 26, 1999
Time of creation	11:46:24
File name	J0226-25.img
Label	**Temperature**
SP01	21.1°C
SP02	20.4°C
SP03	20.9°C
LI01: cursor	23.9°C
LI01: max	25.7°C
LI01: min	19.8°C

Fig. 2. Specimen with a sharp notch.

pation volume containing all forms of the energy absorbed in the plastic-deformation zone.

Figure 2 exhibits typical results of the tests for a specimen with a sharp notch. Here, the notation is the same as for the smooth specimen.

A decrease in dissipation volume in the presence of a notch is clearly seen in Fig. 2 and occurs due to the stress concentration at the notch tip [3, 4].

With the known dissipation volume, we can evaluate the energy spent for different processes. The relaxation

process in viscoplastic elastic bodies can be described by the relation

$$P = P_0 \exp\left(-\frac{t}{\tau}\right),$$

where τ is the relaxation time of the material and t is the current time.

In the case of continuous loading, the quantity P as P_0 is a time-dependent function and can be written in a similar way as

$$P = P_0\left(\frac{t}{\tau}\right).$$

The relaxation time, being many-valued, is represented by a certain spectrum. In terms of the relaxation times, this spectrum can be described by the Gauss curve, i.e.,

$$\tau = A\exp\left[\frac{t-\tau_0}{\tau_0}\right]^2.$$

Both the viscoelastic and elastic deformations lead to the energy release. It is well known that the thermal energy $E = kT$ is liberated per bond. Calculating the volume of the plastic-deformation zone (in which the temperature variation occurs, see Figs. 1, 2) and multiplying E by Avogadro's number N_A, we obtain the relation

$$E_t = k\Delta T N_A abh,$$

where k is the Boltzmann constant and a, b, and h are the parameters of the plasticity zone.

The total energy spent for the specimen deformation is

$$E_F = E_t + A = k\Delta T N_A abh + \Delta l P_0(t)\exp\left\{-\frac{t}{A\exp\left(\frac{t-\tau_0}{\tau_0}\right)^2}\right\}.$$

Here, E is the energy spent for heating and A is the work done for the deformation and failure. In other words, using the known parameters, we are capable of separating the energies spent for heating, deformation, and failure.

Thus, we may conclude that the method proposed for the determination of the plastic-deformation zone allows us to extend the feasibility of the destructive testing of specimens.

REFERENCES

1. *Viscoelastic Relaxation in Polymers*, Ed. by M. Shen (Wiley, Berkley, 1971; Mir, Moscow, 1974).
2. Ya. B. Fridman, *Mechanical Properties of Metals. Deformation and Failure* (Mashinostroenie, Moscow, 1974), Part 1.
3. A. M. Belkin, A. P. Vishnevskiĭ, and V. I. Rulev, Metalloved. Term. Obrab. Metal., No. 1, 34 (1989).
4. M. D. Novopashin, S. V. Suknev, and A. M. Ivanov, *Elastoplastic Deformation and Ultimate State of Structural Components with Stress Concentrators* (Nauka, Novosibirsk, 1995).
5. R. P. Bazarov, *Thermodynamics* (Nauka, Moscow, 1989).

Translated by G. Merzon

Doklady Physics, Vol. 46, No. 7, 2001, pp. 484–487. Translated from Doklady Akademii Nauk, Vol. 379, No. 2, 2001, pp. 187–190.
Original Russian Text Copyright © 2001 by Bazhenov, Berlin.

TECHNICAL PHYSICS

Two Mechanisms of Compression Failure of Unidirectional Carbon-Fiber-Reinforced Plastics

S. L. Bazhenov* and Corresponding Member of the RAS A. A. Berlin**

Received February 5, 2001

The compression failure of a unidirectional carbon-fiber-reinforced plastic containing an epoxy matrix as its base is due to the formation of a so-called kink, i.e., a slip band oriented at an angle of approximately 45° to the loading axis [1–5]. It is conventionally considered that the kink appearance in a carbon-filled plastic is due to a violation of the stability of its fibers. This process is similar to the buckling of a rod on an elastic base. The critical stress of the fiber buckling in a composite is equal to the elastic modulus G of the composite under an in-plane shear [6]:

$$\sigma = G. \quad (1)$$

If the fiber concentration in a composite is approximately 50–60 vol %, the shear modulus G of the composite is close to Young's modulus of its matrix and, therefore, the strength due to such a failure mechanism is determined by the rigidity of the matrix.

The assumption that the failure is caused by fiber buckling is confirmed by a certain increase in the strength for a carbon-fiber-reinforced plastic when the elastic modulus of its epoxy matrix is increased [7]. Nevertheless, this is not the only point of view on the failure mechanism for carbon-fiber-reinforced plastics. Indeed, their strength turns out to be significantly lower than the shear modulus. This fact suggests that the compression failure is not caused by fiber buckling. Typical values of the shear modulus for carbon-fiber-reinforced plastics range from 4 to 5 GPa [8, 9]. The compression strength of a carbon-fiber-reinforced plastic depends on the types of both its fibers and its matrix and ranges from 1.2 to 1.8 GPa [7]. These values are not greater than one-third of the shear modulus.

There are two other possible failure mechanisms. It was assumed in [10–12] that the failure of a carbon-fiber-reinforced plastic is caused by the fracture of its fibers and that its strength is determined by a fairly low fiber strength. The values of the carbon fiber strength cited in various papers range from 2.4 to 6 MPa [7, 12]. Measuring the compressive strength for isolated very thin fibers (6–10 μm in diameter) is a technically demanding task, and, therefore, the values published for the fiber strength are not completely reliable. This fact hampers the elucidation of the question raised as to whether a direct correlation exists between the strength of a carbon-fiber-reinforced plastic and that of its fibers.

Another possible mechanism of failure is the splitting (delamination) of a carbon-fiber-reinforced plastic along the direction of its fibers [12]. The splitting of a composite usually involves the origination of longitudinal cracks in the matrix or on the fiber–matrix interface and the subsequent bending of a separated part of the material. The direct formation of the kink by the first longitudinal crack is a specific feature of this failure mechanism in carbon-fiber-reinforced plastics; hence, the crushed sample does not look as though it were split off. The splitting is caused by the low strengths of both the matrix and the interface. This mechanism was originally considered only as a possible mode of failure; however, later studies showed that splitting is the most probable failure mechanism for carbon-fiber-reinforced plastics [13]. According to [13], the failure of a carbon-fiber-reinforced plastic can be caused by either the ultimate strength attained or longitudinal splitting, depending on the types of fibers and the matrix. Since the failure mechanism for composites is not unambiguously established at room temperature, failure with kink origination will be here referred to as a shear failure.

The aim of this report is to study the temperature effect on the compressive failure mechanism for a carbon-fiber-reinforced plastic containing UKN-5000 fibers and an EDT-10 epoxy matrix.

Carbon fibers with the trade mark UKN-5000 were used for reinforcement. An EDT-10 epoxy composition (consisting of an 80 wt % of epoxy ED-20, 10 wt % of triethanolamine titanate hardener, and 10 wt % of diethylene glycol as a modifier) was used as the matrix. The fiber was passed twice through a bath with a liquid resin heated to 60°C and was then wound on a plane bobbin. The bundle obtained was pulled into a steel cylindrical

* *Institute of Synthetic Polymer Materials, Russian Academy of Sciences, Profsoyuznaya ul. 7, Moscow, 117393 Russia*

** *Institute of Chemical Physics, Russian Academy of Sciences, ul. Kosygina 4, Moscow, 117977 Russia*

1028-3358/01/4607-0484$21.00 © 2001 MAIK "Nauka/Interperiodica"

tube with an inner diameter of 9 mm. The epoxy resin was hardened at a temperature of 160°C for 4 h.

The concentration of the fibers in the composite was 46 vol %. The rod was then extracted out of the tube and divided into 50-mm long samples. The central part of the rod was machined off; the diameter of the rod in the minimum cross section was equal to 5 mm. The tests were carried out by using an Instron-1169 machine with cylindrical rails, which allowed the misalignment of the samples under compression to be reduced.

To measure the shear modulus of the carbon-fiber-reinforced plastic, we fabricated cylindrical rods 6 mm in diameter. The bundle was pulled into a glass tube treated by an antiadhesive; the tube was smashed after the resin hardened. The operating length of the rods was 400 mm.

The shear modulus was determined by using a device which allowed us to vary the torsional moment. The calculations were carried out using the formula [14]

$$G = \frac{2ML}{\pi R^4 \varphi}, \quad (2)$$

where M is the torsional moment, L is the operating length of a rod, R is its radius, and φ is the torsional angle of the rod in the plane perpendicular to its axis.

The temperature dependence of the shear modulus for the carbon-fiber-reinforced plastic is shown in Fig. 1. In the range from 20 to 80°C, a moderate decrease in the shear modulus with increasing temperature is observed. There is a sharp decrease in the region of the matrix glass transition (T = 80–90°C) which ceases at a temperature of 120°C.

As is seen from Fig. 2 (curve *1*), the compression strength varies similarly to the shear modulus and sharply drops in the region of the matrix glass transition (80–100°C). At temperatures above 120°C, the strength practically does not vary. The similar behavior of the shear modulus and the compression strength suggests that, in the entire temperature range, the failure is caused by fiber buckling. However, a more careful quantitative analysis of the dependences shows that they significantly differ. The ratio of the compression strength to the shear modulus $\frac{\sigma}{G}$ as a function of temperature is represented by curve *2*. At temperatures above 100°C, the ratio $\frac{\sigma}{G}$ is nearly equal to 0.8 and the strength of the carbon-fiber-reinforced plastic is close to the critical stress of the fiber buckling. Consequently, in this temperature range, the failure is due to the fiber buckling. At temperatures from 20 to 80°C, the ratio $\frac{\sigma}{G}$ is equal to 0.3 and the compression strength is significantly lower than the shear modulus. This suggests that, in this temperature range, the failure of the composite is not caused by the fiber buckling and that at $T \approx T_c$, the

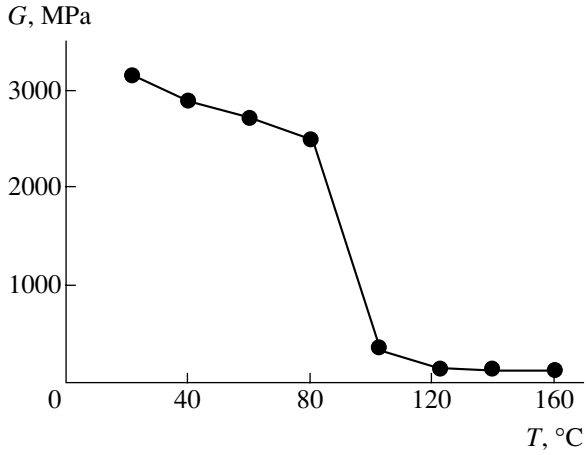

Fig. 1. Dependence of the shear modulus G of the carbon-fiber-reinforced plastic on the test temperature T.

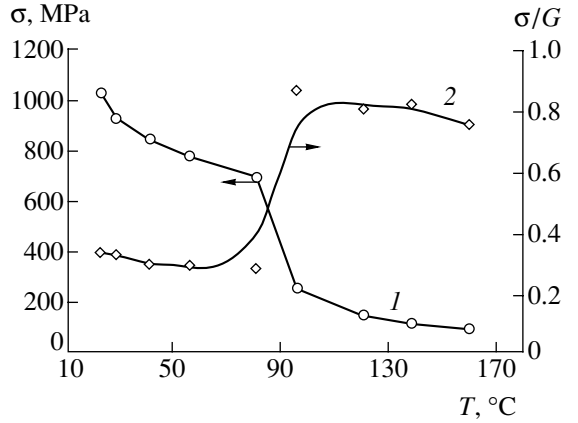

Fig. 2. (*1*) Compression strength σ and (*2*) the ratio $\frac{\sigma}{G}$ of the compression strength to the shear modulus for the carbon-fiber-reinforced plastic as functions of the test temperature T; V_f = 46 vol % (*2*).

change of the failure mechanism from shear failure to fiber buckling occurs.

The examination of samples subjected to the tests showed that, in the temperature region of the matrix glass transition, the appearance of the crushed samples changes. Shear failure takes place at temperatures from 20 to 75°C, with the shear plane oriented at an angle of 50° to 60° to the fiber axis. Above the matrix glass transition temperature, the failure zone is oriented perpendicularly to the stress axis. The temperature dependence of the angle between the plane of the failure band and the fiber axis is presented in Fig. 3. In the temperature region of the matrix glass transition, a sharp jump in the value of the angle takes place.

Thus, the change of both the ratio $\frac{\sigma}{G}$ and the appearance of samples subjected to the tests clearly indicates the fact that, at $T \approx T_c$, the failure mechanism changes.

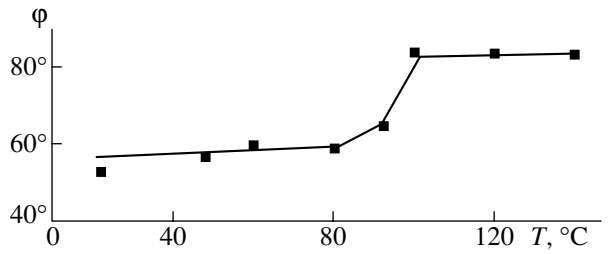

Fig. 3. Dependence of the angle φ between the failure band and the fiber axis on the test temperature *T*.

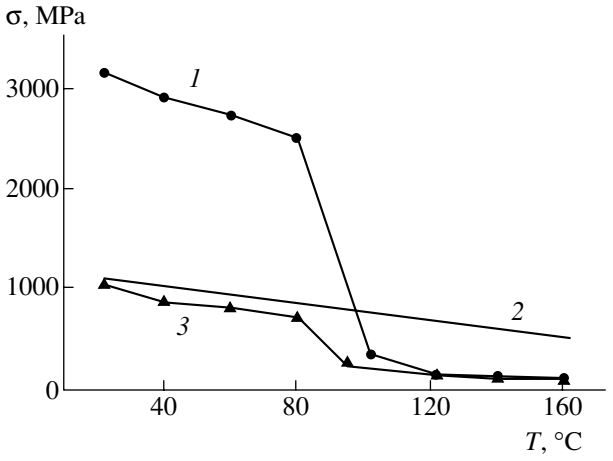

Fig. 4. Critical stresses (*1*) for fiber buckling; (*2*) for shear failure; and (*3*) the experimental values of the compression strength for the carbon-fiber-reinforced plastic as functions of the test temperature *T*.

Since the failure mechanism at temperatures above T_c involves fiber buckling, the failure at room temperature and, correspondingly, kink formation are not associated with fiber buckling.

There are two concurrent failure mechanisms for carbon-fiber-reinforced plastics. The first one is shear failure resulting in kink formation, and the second mechanism is fiber buckling. The failure of a composite occurs when the stress inside it attains the smallest of the two critical stresses that correspond to the above failure mechanisms. The temperature dependence of the critical stresses for both failure mechanisms is shown in Fig. 4. Curves *1* and *2* present, respectively, the critical stress for fiber buckling and the shear strength of the composite. In the range from 20 to 80°C, the critical stress for shear failure (curve *2*) is lower than that for fiber buckling. In the region of the matrix glass transition temperature, the critical stress for fiber buckling sharply drops and, at $T > 90$°C, becomes lower than that for shear failure; this results in a change of the failure mechanism. For comparison, the experimental dependence of the compressive strength for the carbon-fiber-reinforced plastic is given by curve *3*. The experimental values of the strength are close to the minimum critical stress (of the two stresses) in the entire temperature range.

Assuming the failure of carbon-fiber-reinforced plastics to be caused by fiber buckling, Budiansky [15] derived the following expression for the critical stress at which a failure zone oriented at an angle θ to the stress axis is formed:

$$\sigma = G + E\cot\theta, \qquad (3)$$

where *E* is the elastic modulus of a composite subjected to extension perpendicular to its fibers.

The minimum critical stress corresponds to the angle $\theta = 90°$.

The formula derived by Budiansky predicts that the failure zone is perpendicular to the fibers. Zones oriented practically perpendicular to the fibers were observed in all cases when the failure was, *a fortiori*, caused by fiber buckling and the strength was close to the shear modulus of the composite. The failure zone perpendicular to the stress axis was observed in organic- and carbon-fiber-reinforced plastics when the failure tests were carried out at temperatures above the matrix glass transition. The same takes place in glass-fiber-reinforced plastics provided that a special procedure which allows us to lower the misalignment of the samples and to obtain very high values of the strength is employed [13]. A failure zone perpendicular to the fibers was also observed in bending tests of glass-fiber-reinforced plastics containing low-modulus rubberlike matrices as their bases when the failure was initiated near the compressed surface [13].

Thus, when increasing temperature, the failure mechanism transforms from shear failure with kink formation to fiber buckling. We hence conclude that kink formation is not associated with fiber buckling accompanied by a failure zone perpendicular to the fibers. As follows from the analysis of the data published, in all the cases for which the failure of unidirectional composites (organic-, carbon-, or glass-fiber-reinforced plastics) was certainly caused by fiber buckling, the failure zone was perpendicular to the loading axis. This fact, together with formula (3), allows us to conclude that the failure zone caused by fiber buckling is necessarily perpendicular to the loading axis. The presence of a kink indicates that the failure is not associated with fiber buckling. The same can be said in the cases when the samples subjected to tests strongly stratify and there is no clear failure plane perpendicular to the compression axis.

REFERENCES

1. M. R. Piggott, in *Developments in Reinforced Plastics* (Elsevier, New York, 1984), Vol. 4, pp. 131–156.
2. N. L. Hancox, J. Mater. Sci. **10**, 234 (1975).
3. S. Kumar, W. W. Adams, and T. E. Helminiak, J. Reinf. Plast. Compos. **7**, 108 (1988).
4. I. Petker, SAMPE Q. **3**, 7 (1972).

5. J. R. Diefendorf, in *Carbon Fibres and Their Composites*, Ed. by E. Fitzer (Springer-Verlag, Berlin, 1985), pp. 46–61.
6. Yu. M. Tarnopol'skiĭ and A. M. Skudra, *Structural Strength and Deformability of Glass-Fiber-Reinforced Plastics* (Zinatne, Riga, 1966).
7. H. D. Stenzenberger, in *Carbon Fibres and Their Composites*, Ed. by E. Fitzer (Springer-Verlag, Berlin, 1985), pp. 95–142.
8. K. Brunsch, in *Carbon Fibres and Their Composites*, Ed. by E. Fitzer (Springer-Verlag, Berlin, 1985), pp. 207–228.
9. O. V. Lebedeva, Candidate's Dissertation (Inst. Khim. Fiz., Akad. Nauk SSSR, Moscow, 1988).
10. E. M. De Ferran and B. Harris, J. Compos. Mater. **4**, 62 (1970).
11. R. L. Sierakowski, G. E. Newill, C. A. Ross, and E. R. Jones, J. Compos. Mater. **5**, 362 (1971).
12. S. L. Bazhenov and V. V. Kozey, J. Mater. Sci. **26**, 6764 (1991).
13. S. L. Bazhenov, Doctoral Dissertation in Mathematical Physics (Inst. Khim. Fiz., Ross. Akad. Nauk, 1995).
14. L. D. Landau and E. M. Lifshitz, *Course of Theoretical Physics*, Vol. 7: *Theory of Elasticity* (Nauka, Moscow, 1965; Pergamon, New York, 1986).
15. B. Budiansky, Comput. Struct. **16**, 3 (1983).

Translated by T. Galkina

Doklady Physics, Vol. 46, No. 7, 2001, pp. 488–490. Translated from Doklady Akademii Nauk, Vol. 379, No. 3, 2001, pp. 322–324.
Original Russian Text Copyright © 2001 by Bazhenov, Berlin.

TECHNICAL PHYSICS

Temperature Effect on Fracture Mechanisms in Organic-Fiber-Reinforced Plastics under Compression

S. L. Bazhenov* and Corresponding Member of the RAS A. A. Berlin**

Received February 5, 2001

High-strength composite materials based on organic aramid fibers in epoxy matrices are currently widely used in aerospace technology. A shortcoming of these materials is their relatively low compression strength.

The fracture of unidirectionally reinforced composite materials under compression can be caused by different factors. It is commonly assumed that the fracture of organic-fiber-reinforced plastics usually occurs owing to fiber buckling similar to the buckling of a bar at an elastic base [1–7]. The critical compression stress σ corresponding to the buckling is equal to the shear modulus of the composite:

$$\sigma = G_c, \tag{1}$$

where G_c is the elastic modulus corresponding to the longitudinal shear. In the unidirectional composites with a fiber volume fraction of 50–70 vol %, the shear modulus is close to Young's modulus of the matrix. As a consequence, the fiber buckling is determined by the matrix rigidity.

The shear modulus of organic-fiber-reinforced plastics based on different aramid fibers ranges from 1.4 to 2.0 GPA [8–11]. A typical value of the compression strength for organic plastic materials with aramid fibers is equal to 0.2–0.3 GPa. This value corresponds only to about 15% of their shear modulus. The large difference between the actual compressive strength of an organic-fiber-reinforced plastic and its estimate based on Eq. (1) suggests that the fracture of the composite is not determined by the fiber buckling. It was suggested that the fracture of a composite is initiated by the fracture of fibers owing to the low compressive strength of the fibers. Note that the strength measurements for individual fibers constitute a serious technical problem since their diameter is rather small (about 13 μm). The strength values for the SVM fibers reported in different papers range from 400 to 900 MPa [9, 12, 13]. However, even the highest reported value, 900 MPa, is lower by a factor of 5–6 than the tensile strength. This is a clear indication of the insufficient compressive strength of these fibers.

The present paper is aimed at studying the temperature effect on a fracture under compression for organic-fiber-reinforced plastics with SVM aramid fibers in the epoxy matrix.

For strengthening, we used organic aramid filaments of the SVM trademark consisting of 300 fibers with a mean diameter equal to 13 mm. As a matrix, we used an epoxy composition EDT-10 consisting of epoxy resin ED-20 (80 wt %), triethanolamine titanate hardener (10 wt %), and diethylene glycol modifier (10 wt %). A fiber bunch consisting of four parallel filaments was dragged twice through a bath filled with liquid resin heated to 60°C and was then wound onto a planar mandrel. The resulting fiber bundle was drawn into a steel cylindrical tube with an inner diameter of 9 mm. The epoxy resin was cured over 4 h at 160°C. The fiber content in the composite was 50 vol %. Thereafter, the bar was extracted from the tube and was cut into samples 50 mm long. The tests were performed using an Instron-1169 with the help of cylindrical guides, which allowed us to reduce the compression-induced warp.

To measure the shear modulus of the organic-fiber-reinforced plastic, we manufactured cylindrical bars 6 mm in diameter. The fiber bundle was drawn into a glass tube treated by an antiadhesive. After curing of the resin, the tube was broken. The content of fibers was also equal to 50 vol %. The operating length of the bar was 400 mm. The shear modulus was determined using a setup which allowed us to measure the torque. The shear modulus was calculated according to the formula [14]

$$G = \frac{2ML}{\pi R^4 \varphi}, \tag{2}$$

where M is the torque, L is the operating length of the bar, R is its radius, and φ is the torsion angle of the bar in the plane perpendicular to its axis.

The shear modulus of the composite as a function of test temperature T is plotted in Fig. 1. Within the 20–60°C range, the shear modulus linearly decreased with a rise in temperature. Near the glass transition temper-

* *Institute of Synthetic Polymeric Materials, Russian Academy of Sciences, Profsoyuznaya ul. 70, Moscow, 117393 Russia*

** *Semenov Institute of Chemical Physics, Russian Academy of Sciences, ul. Kosygina 4, Moscow, 117977 Russia*

1028-3358/01/4607-0488$21.00 © 2001 MAIK "Nauka/Interperiodica"

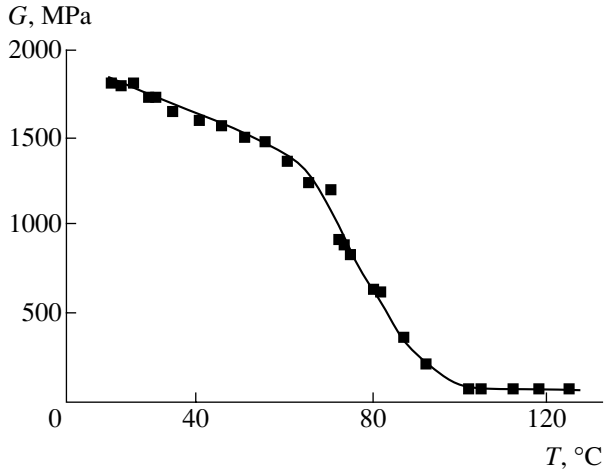

Fig. 1. Shear modulus G of organic-fiber-reinforced plastic versus testing temperature T.

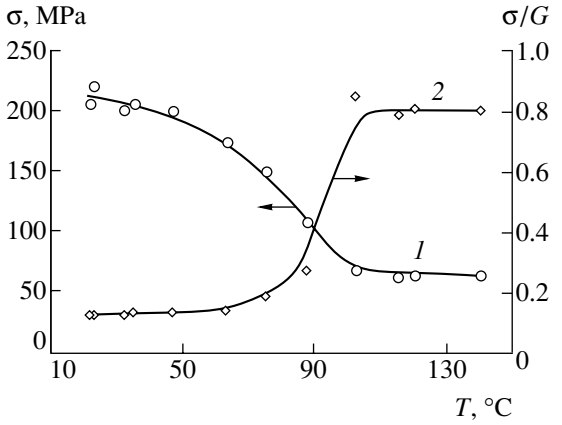

Fig. 2. (*1*) Compressive strength σ and (*2*) ratio $\frac{\sigma}{G}$ of the compressive strength to the shear modulus versus testing temperature T; V_f = 50 vol %.

ature of the matrix ($T_g \approx 80$°C), the modulus decreases; this decrease terminates at about 100°C.

The compression strength behaves in the same way as the shear modulus (see Fig. 2, curve *1*). A slight decrease in the strength within the 20–60°C temperature range gives way to a steep drop at 70–100°C. At temperatures above 100°C, the strength remains nearly unchanged (see Fig. 2, where curve *2* illustrates the temperature dependence of the $\frac{\sigma}{G}$ ratio; σ is the compressive strength). At 20–80°C, this ratio is as low as 0.12–0.13 and the compressive strength is much lower than the shear modulus. Hence, in this temperature range, the fracture of the composite is not related to the fiber buckling.

The fracture stress of fibers was estimated using the so-called mixture rule, according to which the strength of a composite is equal to the sum of strengths of the fibers and matrix (with account taken of their volume fractions) [15]:

$$\sigma_c = \sigma_f V_f + \sigma_m(1 - V_f), \quad (3)$$

where σ_f and σ_m are the strengths of the fibers and matrix, respectively, and V_f is the volume fraction of fibers.

The compression strength of the epoxy matrix is assumed to be equal to its tensile strength. The latter is determined from the tension of films 200–300 μm thick, and the corresponding estimates give 85 MPa. Using 220 MPa as the value of the compressive strength of the composite with $V_f = 0.50$, the strength of fibers can be estimated as 360 MPa. This value is close to the compressive strength of individual organic fibers (400–500 MPa) reported in [12, 13]. Thus, we come to the conclusion that the strength of organic-fiber-reinforced plastics is limited by the strength of their fibers.

At temperatures above 100°C, the ratio of the shear modulus to the compressive strength equals 0.8 (Fig. 2, curve *2*). The strength of the composite is close to the critical stress corresponding to the fiber buckling. Therefore, in this temperature range, a fracture occurs due to fiber buckling, whereas at $T \approx T_g$, the fracture mechanism changes because the resistance of fibers to buckling is exhausted.

The study of the samples after testing demonstrated that the change in the fracture mechanism is accompanied by changes in the pattern of the fracture zone, as is schematically illustrated in Fig. 3. Within the 20–65°C temperature range, the fracture zone is a shear band oriented at an angle of 48–52°C to the fiber axis. The fibers attain the form of a Z-shaped kink. Above the glass transition temperature for the matrix, the fracture zone has a different form. In this case, it is oriented perpendicular to the loading axis and the fibers become V-shaped. The temperature dependence of the angle between the plane of the fracture band and the fiber axis

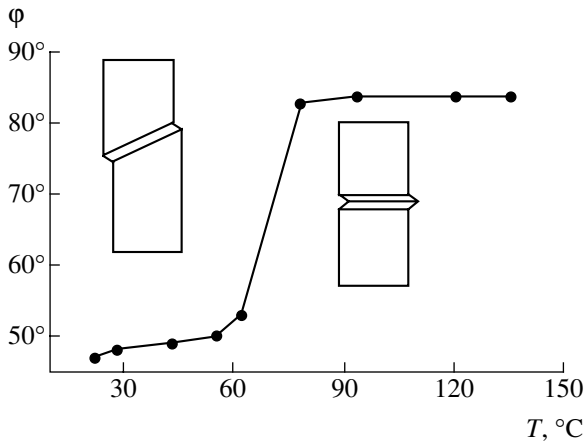

Fig. 3. Angle φ between the fracture band and the fiber axis versus testing temperature T.

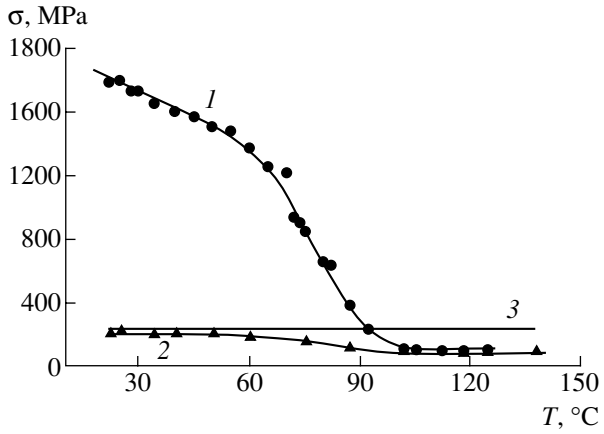

Fig. 4. Critical stress corresponding to the buckling (*1*) and the yield strength for fibers (*3*) versus testing temperature *T*. Curve *2* illustrates the measured compressive strength of the organic-fiber-reinforced plastic.

is shown in Fig. 3. In the neighborhood of the glass transition temperature for the matrix, the change in the fracture mechanism causes a drastic change in the angle.

Thus, we have two competing mechanisms underlying the fracture of organic-fiber-reinforced plastics. The first mechanism is related to the properties of fibers, namely, to their strength. The second fracture mechanism (the fiber buckling) is limited by the characteristics of the matrix, namely, by its elastic modulus. The fracture of a composite occurs upon attainment of the lower of the two critical values of stresses corresponding to these fracture mechanisms.

The temperature dependence of critical stresses for both fracture mechanisms is shown in Fig. 4. Curve *1* corresponds to the critical stress of the fiber buckling equal to the shear modulus of the composite. Curve *3* defines the strength of the composite for the fracture occurring when the fiber strength is exhausted. The fiber strength in the temperature range 20–120°C decreases by no more than 20%. At relatively low temperatures ($T < 60$°C) straight line *3* is lower than the stress corresponding to the fiber buckling and the fracture is related to the fiber strength. In the vicinity of the glass transition temperature for the matrix, the critical stress corresponding to the fiber buckling steeply decreases and at high temperatures ($T > 90$°C) becomes lower than the fiber strength. For comparison, in Fig. 4, curve *2* illustrates the measured temperature dependence of the strength for the composite under study. In the entire temperature range under discussion, the actual strength of the composite is relatively close to the minimum value (among two of them) of the critical stress. The change in the fracture mechanism in the vicinity of T_g for the matrix is accompanied by a drastic change in the angle between the fracture plane and the fiber axis, as well as in the symmetry of the fiber bending in the fracture band.

In conclusion, the fracture of organic-fiber-reinforced plastic is caused by the exhaustion of the fiber strength with respect to their buckling. At high temperatures ($T > T_g$), the strength of the composite is already limited by the matrix rigidity rather than by the fiber strength. When the fracture occurs due to the fiber buckling, the fracture zone is oriented perpendicularly to the sample axis.

REFERENCES

1. B. W. Rosen and N. F. Dow, in *Fracture*, Vol. 7: *Fracture of Nonmetals and Composites*, Ed. by H. Liebowitz (Academic, New York, 1972; Mir, Moscow, 1976), Part 1.
2. A. N. Guz' and I. Yu. Babich, in *Mechanics of Materials* (Naukova Dumka, Kiev, 1982), pp. 120–143.
3. S. J. DeTeresa, R. J. Farris, and R. S. Porter, Polym. Compos. **3**, 57 (1982).
4. C. C. Chan, J. Blackson, and J. Im, Polymer **36**, 2511 (1995).
5. S. J. DeTeresa, S. R. Allen, R. J. Farris, and R. S. Porter, J. Mater. Sci. **19**, 57 (1984).
6. F. J. McGarry and J. E. Moalli, Polymer **32**, 1811 (1991).
7. S. J. DeTeresa, R. S. Porter, and R. J. Farris, J. Mater. Sci. **23**, 1886 (1988).
8. O. V. Lebedeva, Candidate's Dissertation (Inst. Khim. Fiz. Akad. Nauk SSSR, Moscow, 1988).
9. A. A. Aslanyan, S. L. Bazhenov, A. Ya. Gorenberg, *et al.*, Dokl. Akad. Nauk SSSR **291**, 1113 (1986) [Sov. Phys. Dokl. **31**, 999 (1986)].
10. V. V. Koziĭ, S. L. Bazhenov, A. M. Kuperman, *et al.*, Dokl. Akad. Nauk SSSR **298**, 62 (1988).
11. S. L. Bazhenov, V. V. Kozey, and A. A. Berlin, J. Mater. Sci. **24**, 4509 (1989).
12. S. R. Allen, J. Mater. Sci. **22**, 853 (1987).
13. S. Bazhenov, Composites **26**, 757 (1995).
14. L. D. Landau and E. M. Lifshitz, *Course of Theoretical Physics*, Vol. 7: *Theory of Elasticity* (Nauka, Moscow, 1965; Pergamon, New York, 1986).
15. A. Kelly and W. R. Tyson, *Fiber-Strengthened Materials, High Strength Materials* (Wiley, New York, 1965).

Translated by K. Kugel

Doklady Physics, Vol. 46, No. 7, 2001, pp. 491–494. Translated from Doklady Akademii Nauk, Vol. 379, No. 3, 2001, pp. 325–328.
Original Russian Text Copyright © 2001 by Bakhrakh, Izrailovich.

TECHNICAL PHYSICS

Synthesis of Correcting Signals for Ultrashort-Pulse Antennas

Corresponding Member of the RAS L. D. Bakhrakh* and M. Ya. Izrailovich**

Received January 25, 2001

In the case of the emission of ultrashort pulses by antennas [1, 2], a rather significant discrepancy between the time diagrams of an exciting signal transmitted to an antenna and of an emitted pulse is observed. In particular, the emitted signal is noticeably stretched in time compared to the initial transmitting (exciting) pulse.

Therefore, an adequate correction of the time diagrams for emitted signals is a rather urgent task.[1] In the present paper, a method for solving the problem is proposed, which is based on the employment of an additional correcting signal. The latter signal is transmitted to the antenna input simultaneously with the basic (operating) pulse and also acts after the basic-pulse termination; i.e., the additional signal is more strongly stretched in time.

1. STATEMENT OF THE PROBLEM AND ITS SOLUTION

It is assumed that the emitted and exciting signals are related to each other by a linear operator,

$$y_0(t) = \int_0^t h(t-\tau)x_0(\tau)d\tau.$$

Here, $h(t)$ is the antenna pulsed transient function that, in the general case, can be found experimentally, in particular, by solving the corresponding differential equations.

In order to obtain a corrected emitted signal $y_0(t)$, a correcting pulsed action $u(t)$ is transmitted to the antenna input in addition to the basic exciting pulse $x_0(t)$. As a result, the emitted signal is transformed to

$$y(t) = \int_0^t h(t-\tau)[x_0(\tau) + u(\tau)]d\tau. \quad (1)$$

In contrast to the basic signal $x_0(t)$, the correcting signal is assumed to smoothly increase with time and to be more stretched within the initial time interval of its application.

We also assume that the desired time diagram for the emitted signal $y_*(t)$ is specified and that both $x_0(t)$ and $y_*(t)$ are finite functions:

$$x_0(t) = 0, \quad t \in (T_1, \infty), \quad y_*(t) = 0,$$

$$t \in (T_2, \infty), \quad T_2 \geq T_1.$$

The correcting action $u(t)$ is introduced in order to obtain a signal $y(t)$ that would be the best approximation to the desired radiated signal $y_*(t)$. In this case, the exact reproduction of the signal $y_*(t)$ is generally impossible in the class of physically realizable signals $u(t)$. Therefore, we should speak only about the best approximation. Here, we imply that two features of the emitted signal should be attained. First, $y(t)$ should be close to $y_*(t)$ at $t \in [T_2, T]$; i.e., an approximate specific shape of the emitted signal should be provided. Second, $y(t)$ should be close to zero for $t \in [T_2, T]$, where T is the time duration of the action $u(t)$ of the correcting signal, which is assumed to be finite. The second property corresponds to minimizing the antenna-emission intensity beyond the required time range $(0, T_2)$.

The goal formulated above can be attained by introducing certain constraints imposed on the correcting-signal intensity with allowance for the above arguments. Thus, the following integral quadratic functional can be used as the optimum criterion for finding the function $u(t)$:

$$I(u) = \int_0^T [(y - y_*)^2 + \gamma u^2]dt. \quad (2)$$

[1] The problems of correcting the antenna's directivity patterns are beyond the scope of this consideration. Although this problem is also topical, it should be considered in its own right.

* *Moscow Research Institute of Instrument Building, Kutuzovskiĭ pr. 34, Moscow, 121170 Russia*

** *Blagonravov Institute of Engineering Science, Russian Academy of Sciences, ul. Bardina 4, Moscow, 117334 Russia*

1028-3358/01/4607-0491$21.00 © 2001 MAIK "Nauka/Interperiodica"

Here, γ is a weighting factor that takes into account the relation between the requirement of minimizing the deviation $(y - y_*)^2$ and the intensity of the correcting signal $u(t)$.

The minimization problem for functional $I(u)$ (2) with the constraint (1) imposed is solved on the basis of the procedure presented in [3]. According to this procedure, Eq. (1) is written in the form $y = Ax_0 + Au$, where A is a bounded linear operator specified on the class of the functions $L^2(0, T)$, and functional (2) is expressed in the form

$$I(u) = (Au + Ax_0 - y_*, Au + Ax_0 - y_*) + \gamma(u, u). \quad (3)$$

Furthermore, the Gateaux derivative of functional (3) with respect to u is calculated and the following operator equation for u is determined from the condition of steadiness of the solution:

$$(A^*A + \gamma)u = -A^*Ax_0 + A^*y_*. \quad (4)$$

Here, the operator A^* is conjugate to the operator A. From Eq. (4), the optimum law

$$u_* = R_\gamma(-A^*Ax_0 + A^*y_*) \quad (5)$$

is determined, where the operator $R_\gamma = (A^*A + \gamma)^{-1}$ is inverse to the operator $A^*A + \gamma$.

According to the results presented in [3], the solution u_* (5) exists and is unique.

Since the conjugate operator A^* is defined in the form

$$y(t) = \int_t^T h(s - t) f(s) ds,$$

where $f(s)$ is an arbitrary function $f \in L^2(0, T)$, operator equation (4) appears, in the nonabstract form, as

$$\int_t^T h(s - t) \int_0^s h(s - \tau) u(\tau) d\tau ds + \gamma u = -\int_t^T h(s - t) \int_0^s h(s - \tau) x_0(\tau) d\tau ds + \int_t^T h(s - t) y_*(s) ds. \quad (6)$$

Equation (6) is a Volterra integral equation of the second kind; thus, the operator R_γ represents its resolvent. From Eq. (6), it follows for $t = T$ that $u(T) = 0$. Applying the operator A^{*-1}, which is inverse to the operator A^*, to the left-hand side and right-hand side of Eq. (6), we obtain the second boundary condition $\gamma A^{*-1}u(0) = y_*(0) = 0$ for $t = 0$. Both of these boundary conditions are natural. To account more accurately, if necessary, for the possibility of physical realization of the correcting signal $u(t)$, one more condition should be added, namely, $u(0) = 0$. This can be provided by properly choosing either the duration T of the action $u(t)$ or the value of the weighting factor γ.

2. A PROBLEM WITH FIXED FINAL CONDITIONS

Despite the fact that the obtained solution $u_*(t)$ provides a decrease in the intensity of the emitted signal $y(t)$ at $t \in (T_2, T)$, this solution cannot ensure the complete absence of the signal at the time moment T. To meet this condition, it is necessary that $y^i(T) = 0$ ($i = 0, 1, \ldots, n - 1$) at the moment $t = T$, where the superscript i implies the ith-order derivative of the function $y(t)$, which is calculated at the moment $t = T$.

According to Eq. (1), the latter conditions are written out in the form

$$A_i(T)x_0 + A_i(T)u = 0, \quad i = 0, 1, \ldots, n - 1, \quad (7)$$

where

$$A_i(T) = \int_0^T h^i(T - t) x_0(t) dt.$$

To satisfy conditions (7), the extended functional

$$\hat{I}(u, \lambda_i) = I(u) + \sum_{i=0}^{n-1} \lambda_i A_i(T) u \quad (8)$$

is introduced instead of $I_0(u)$ (3), where λ_i are the Lagrange multipliers.

By applying the same procedure to functional (8) that was used for minimizing functional (3), the following operator equation with respect to u is obtained:

$$(A^*A + \gamma)u = -A^*Ax_0 + A^*y_* - \sum_{i=0}^{n-1} \lambda_i h^i(T - t). \quad (9)$$

From Eq. (9), we find

$$u(\lambda_i) = R_\gamma \left[A^*(y_* - Ax_0) - \sum_{i=0}^{n-1} \lambda_i h^i(T - t) \right]. \quad (10)$$

By substituting equality (10) into (7), a system of n linear algebraic equations in λ_i is obtained. Substituting the solution to this system into (10), we arrive at the final expression for the correcting signal. This expression provides the total absence of the antenna's emission at the moment T of the signal-action termination:

$$u_* = R_\gamma \left\{ A^*(-Ax_0 + y_*) + \sum_{i=0}^{n-1} \sum_{j=0}^{n-1} \frac{\Delta_{ij}}{\Delta} h^i(T - t) \times A_j(T)[R_\gamma A^*(-Ax_0 + y_*) + x_0] \right\}. \quad (11)$$

Here, Δ is the determinant of the matrix

$$\left\| A_i(T) R_\gamma h^j(T-t) \right\|,$$

$$i = 0, 1, \ldots, n-1, \quad j = 0, 1, \ldots, n-1,$$

and Δ_{ij} is its algebraic cofactor for an element with the subscript ij.

It follows from the above-mentioned that solution (11) to the minimization problem for functional (2) under conditions (7) exists and is unique if the matrix $\|A_i(T)R_\gamma h^j(T-t)\|$ is nondegenerate. Equation (9), in its nonabstract form, differs from Eq. (6) in the presence of the function

$$H(t) = -\sum_{i=0}^{n-1} \lambda_i h^i(T-t) \tag{12}$$

in the right-hand side as a summand. By virtue of this fact, the following natural boundary conditions are defined: $u(T) = H(T)$, $\gamma A^{*-1} u(0) = H(0)$.

3. PARTICULAR CASES

If the exciting-signal duration is rather short and its intensity is very high, the signal can be approximately taken in the form of the δ-function. In this case, instead of Eq. (1), the following expression can be used for the output signal $y(t)$:

$$y(t) = h(t)x_0(0) + \int_0^t h(t-\tau)u(\tau)d\tau.$$

According to this expression, Eq. (6) acquires the form

$$\int_t^T h(s-t)\int_0^s h(s-\tau)u(\tau)d\tau ds + \gamma u$$

$$= -\int_t^T h(s-t)h(s)ds\,x_0(0) + \int_t^T h(s-t)y_*(s)ds.$$

In the case of the solution to the problem under conditions (7), the expression for the correcting pulse u_* (11) has the form

$$u_* = R_\gamma \Bigg\{ A^*[-h(t)x_0(0) + y^*]$$

$$+ \sum_{i=0}^{n-1}\sum_{j=0}^{n-1} \frac{\Delta_{ij}}{\Delta} h^i(T-t)[-A_j(T)R_\gamma A^* h(t)x_0(0) \tag{13}$$

$$+ A_j(T)R_\gamma A^* y_* + h_j(T)x_0(0)] \Bigg\}.$$

Another particular case corresponds to the determination of $u(t)$ with the single purpose of decreasing the emission intensity. Such a problem is meaningful if the desired emitted-signal intensity $y_*(t)$, $t \in (0, T_2)$ is rather high, while its duration T_2 is short and the correction of its time diagram by the action $u(t)$ is virtually unfeasible. Therefore, it is reasonable to use the correcting signal $u(t)$ only for lowering the emission intensity at $t > T_2$ (i.e., for lowering the free-oscillation intensity). In this case, either in (5) [or in (11) or (13)], we should assume that $y_* = 0$.

Determination of u_* with the single aim of quieting an antenna [i.e., to attain the total absence of the emission at the moment $t = T$, which corresponds to conditions (7)] is a further particular case. In this case, only correcting-signal intensity

$$I(u) = \int_0^T u^2 dt$$

is used as a minimizing functional. The solution is found from (11) for $R_\gamma = 1$ and by excluding all terms except those corresponding to inhomogeneous boundary conditions (7):

$$u_* = \sum_{j=0}^{n-1}\sum_{i=0}^{n-1} \frac{\Delta_{ij}}{\Delta} h^i(T-t)A_j(T)x_0. \tag{14}$$

We now assume that it is necessary to find a minimum time $T_{\min}$ for the quieting problem with a given intensity $I(u) \le \bar{I}$. According to [4], the value of $T_{\min}$ is determined from the equation $I[u_*(T)] \le \bar{I}$, where $u_*(T)$ is determined according to solution (14).

AN EXAMPLE

As a simplest (model) example, we consider a case in which the operator A is an integrating factor:

$$y(t) = \int_0^t [x_0(\tau) + u(\tau)]d\tau,$$

with

$$x_0(t) = \begin{cases} X, & t \in (0, T_1) \\ 0, & t \in [0, T_1], \end{cases}$$

$$y_*(t) = \begin{cases} Vt, & t \in (0, T_1) \\ 0, & t \in [T_1, T]. \end{cases}$$

In this case, $h(t) = 1$. We consider the problem of finding u_* under the condition $y(T) = 0$, from which it follows that

$$T_1 X + \int_0^{T_1} u(t)dt = 0. \tag{15}$$

According to Eqs. (6) and (9), the integral equation for u is of the form

$$\begin{aligned}\int_t^T\int_0^s u(\tau)d\tau ds + \gamma u \\ = -\int_t^T\int_0^s x_0(\tau)d\tau ds + \int_t^T y_*(s)ds - \lambda,\end{aligned} \tag{16}$$

where λ is the Lagrange multiplier.

From (15), it follows for $t = T$ that $u(T) = -\frac{\lambda}{\gamma}$. Differentiating (16), we obtain

$$\int_0^t u(\tau)d\tau + \gamma\dot{u} = -\int_0^t x_0(\tau)d\tau + y_*(t),$$

whence it follows that $\dot{u}(0) = 0$. After repeated differentiation, we obtain the second-order equation in u:

$$\ddot{u} + \omega_0^2 u = \omega_0^2(-x_0 + \dot{y}_*), \quad \omega_0^2 = \frac{1}{\gamma}. \tag{17}$$

By integrating Eq. (17) with the initial conditions $u(0) = u_0$, $\dot{u}(0) = 0$, we arrive at

$$\begin{aligned}u(t) &= \cos\omega_0 t u_0 + (1 - \cos\omega_0 t)(V - X), \\ &t \in [0, T_1), \\ u(t) &= \cos\omega_0 t u_0 \\ &+ [\cos\omega_0(t - T_1) - \cos\omega_0 t](V - X) \\ &- \omega_0 \sin\omega_0(t - T_1)VT_1, \\ &t \in [T_1, T).\end{aligned} \tag{18}$$

Next, we consider a case when $V = X$. In this case, from the condition $u(T) = -\lambda\omega_0^2$, we determine u_0 as

$$u_0 = \frac{-\omega_0^2\lambda + \omega_0 \sin\omega_0(T - T_1)VT_1}{\omega s \omega_0 T}.$$

(Since λ is unknown, the quantity u_0 can also be taken as unknown.)

From condition (15), by virtue of solution (18), the following equation is obtained:

$$\sin\omega_0 T u_0 - [1 - \cos\omega_0(T - T_1)]VT_1 + VT_1 = 0.$$

From this equation, with the constraint

$$T = T_1 + \frac{1}{\omega_0}\left(\frac{\pi}{2} + k\pi\right), \quad k = 1, 2, 3, \ldots,$$

it follows that $u_0 = 0$. Hence, by virtue of solution (18), we may conclude that

$$u_*(t) = \begin{cases}0, & t \in (0, T_1) \\ -\omega_0 \sin\omega_0(t - T_1)VT_1, & t \in [T_1, T).\end{cases}$$

REFERENCES

1. H. F. Harmuth, *Nonsinusoidal Waves for Radar and Radio Communication* (Academic, New York, 1981; Radio i Svyaz', Moscow, 1985).
2. L. D. Bakhrakh and A. A. Bliskovitskiĭ, Usp. Fiz. Nauk **162** (12), 51 (1992).
3. R. E. Bellman, I. Glicksberg, and O. A. Gross, *Some Aspects of the Mathematical Theory of Control Processes* (Rand Corp., Santa Monica, 1958; Inostrannaya Literatura, Moscow, 1962).
4. N. N. Krasovskiĭ, *Theory of Traffic Control. Linear Systems* (Nauka, Moscow, 1968).

Translated by V. Tsarev

Doklady Physics, Vol. 46, No. 7, 2001, pp. 495–498. Translated from Doklady Akademii Nauk, Vol. 379, No. 1, 2001, pp. 50–53.
Original Russian Text Copyright © 2001 by Bulychev.

MECHANICS

Dynamics of the Destruction of an Armored Polymer with Allowance for an Interfacial Layer

G. G. Bulychev

Presented by Academician I.F. Obraztsov February 19, 2001

Received March 1, 2001

A model for numerical simulation of the dynamics and dynamic destruction (foliation) of armored polymers is proposed with allowance for the interfacial layer. A method of numerical simulation is developed and realized. The role of the interfacial layer in the local dynamic foliation of a polymeric composite is demonstrated.

At present, polymeric composites with a highly developed interfacial surface are widely used. In these materials, an interfacial layer is formed in the polymeric matrix at the interphase boundary. This layer has a rather complicated microstructure, and its micromechanical characteristics differ from matrix properties [1].

For the interfacial layer consisting of polymeric macromolecules sewn at one end to the surface of the armor, equations were proposed describing the stress-strain state under large deformations [2]. Here, these equations are employed as initial equations in constructing a mathematical model for the case of small strains.

In the simulation, we use a method developed for studying the dynamics and destruction of anisotropic piecewise continuous bodies [3, 4]. The dynamic destruction (foliation) of an armored polymer is analyzed similarly to as in [4] under the assumption of an initial proportional tension of the armor and matrix along the direction of the armor fibers and a subsequent instantaneous break of one of the fibers. The initial tension of the fibers and the matrix is such that they cannot be removed from the elastic region. On the other hand, after subsequent redistribution of stresses, both the matrix and fibers become elastoplastic. This redistribution is axisymmetric, the symmetry axis lying in the axis of the broken fiber. Two coaxial layers can be distinguished around the fiber. The first is a thin interfacial layer consisting of macromolecules aligned in the direction normal to the side surface of armoring fibers. The second is the isotropic layer of the matrix material.

The elongation of macromolecules in the direction of the fiber surface is governed by the anisotropy parameter $a = \frac{R}{R_0}$. Here, R is the distance between the ends of a macromolecule forming the interfacial layer (this distance is taken along the normal to the armor) and R_0 is the average distance between macromolecule ends inside the polymer (Fig. 1). Furthermore, h is the conditional thickness of the interfacial layer and the OZ and OR axes are directed along and transverse to the fiber, respectively.

In order to determine the stress-strain state of the interfacial layer under small strains, we use a nonlinear model [2] in which the stress tensor t_{ij} is connected with the elongation tensor λ_{in} through the relation

$$t_{ij} = 2C\lambda_{in}\lambda_{jn}a_n^2 - p\delta_{ij} - t_{ij}^0. \quad (1)$$

Here, $C = \frac{T\chi R_{02}}{6Nq^2h}$, T is the absolute temperature expressed in energy units, χ is the density of macromolecules on the fiber surface, R_{02} is the mean square distance between the macromolecule ends far from the surface, N is the number of macromolecule segments, q is the segment linear size, and $\lambda_{ij} = \frac{\partial x_i^*}{\partial x_j}$, where x_j and

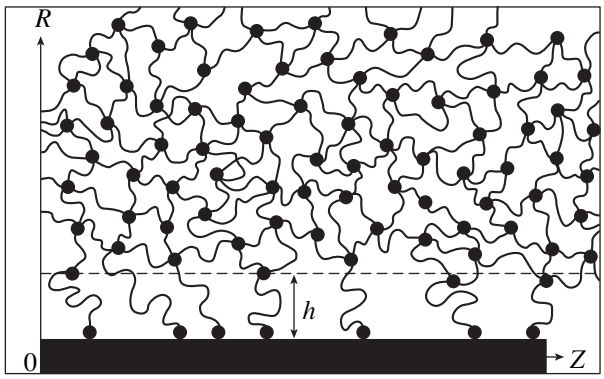

Fig. 1.

State Institute of Physicotechnical Problems, ul. Prechistinka, Moscow, 119034 Russia

1028-3358/01/4607-0495$21.00 © 2001 MAIK “Nauka/Interperiodica”

x_i^* are the coordinates of a point in the interfacial layer before and after deformation, respectively. Furthermore, a_n is the relative change in the coordinates of a point in the interfacial layer (under the condition that relations $a_2 = a_3 = a_1^{-1/2}$ and $a_1 = a$ are fulfilled); δ_{ij} is the Kronecker delta; $p = \frac{t_{11} + t_{22} + t_{33}}{3}$ is the hydrostatic pressure; and t_{ij}^0 are the components of the initial stress field in the interfacial layer, which is caused by the effect of the contact surface. In this case, $t_{11}^0 = 2C(a_1^2 - a_2^2)$ and all other terms $t_{ij}^0 = 0$. Henceforth, summation is performed over repeated indices $i, j, n = 1, 2, 3$.

To linearize Eq. 1, we express the elongation λ_{ij} in terms of the distortions $u_{i,j}$ according to the formulas $\lambda_{ij} = \delta_{ij} + u_{i,j}$.

As a result, ignoring the quadratic (in distortions) terms, we obtain, instead of Eq. (1), relations of the form

$$t_{ij} = 2C(\delta_{in}\delta_{jn}a_n^2 + \delta_{in}a_n^2u_{j,n} + \delta_{jn}a_n^2u_{i,n}) - p\delta_{ij} - t_{ij}^0, \quad (2)$$

which are linear in distortions. Taking into account the expressions for p and t_{ij}^0 and the condition $t_{ij} = t_{ji}$ for $i \neq j$, which is a corollary of relation (2), we arrive at the equations for the normal and tangential stresses, respectively:

$$t_{\alpha\alpha} - \frac{C}{a} = \frac{2C(5a_\alpha^2u_{\alpha,\alpha} - a_\beta^2u_{\beta,\beta} - a_\gamma^2u_{\gamma,\gamma})}{3}, \quad (3)$$

$$t_{\beta\gamma} = 2C(a_\gamma^2u_{\beta,\gamma} + a_\beta^2u_{\gamma,\beta}). \quad (4)$$

Here, $\alpha \neq \beta \neq \gamma \neq \alpha$; $\beta < \gamma$; $\alpha, \gamma = 1, 2, 3$; $\beta = 1, 2$.

Analysis of Eqs. (3) and (4) shows that the stress t_{ij} describes the mixed force and moment states of the layer under consideration. For isolation of these states, we separate the stresses t_{ij} into components of the force σ_{ij} and moment $\mu_{ij} = t_{ij} - \sigma_{ij}$. Then, we put the force stresses in correspondence to the symmetric parts of the distortions, i.e., the strains and symmetric part of the matrix linking the stresses t_{ij} with the distortions.

Expanding the distortion tensor into the strain tensor $\varepsilon_{ij} = 0.5(u_{i,j} + u_{j,i})$ and the rotation tensor $\omega_{ij} = 0.5(u_{i,j} - u_{j,i})$, we obtain the defining relations for the forces and moments:

$$\sigma_{\alpha\alpha} - \frac{C}{a} = \frac{C}{3}[10a_\alpha^2\varepsilon_{\alpha\alpha} - (\alpha_\beta^2 + a_\alpha^2)\varepsilon_{\beta\beta} - (a_\gamma^2 + a_\alpha^2)\varepsilon_{\gamma\gamma}],$$

$$\sigma_{\beta\gamma} = 2C(a_\beta^2 + a_\gamma^2)\varepsilon_{\beta\gamma},$$

$$\mu_{\alpha\alpha} = \frac{C}{3}[(a_\alpha^2 - a_\beta^2)\varepsilon_{\beta\beta} - (a_\alpha^2 - a_\gamma^2)\varepsilon_{\gamma\gamma}], \quad (5)$$

$$\mu_{\beta\gamma} = 2C(a_\beta^2 - a_\gamma^2)\omega_{\beta\gamma}.$$

Analysis of the matrices obtained with the help of the equations constructed testifies to the fact [3] that the moment state is described by bending and torsion waves propagating with the velocities $b_1 = \sqrt{\frac{C(a_1^2 - a_2^2)}{\rho}}$ and $b_2 = \sqrt{\frac{C(a_1^2 - a_3^2)}{\rho}}$, respectively (here, ρ is the density of the interfacial-layer material). In the case of $a = 1$, the moment state disappears.

The defining force equations describe a transversely isotropic medium in which waves of six types propagate. These are three longitudinal waves with the velocities

$$c_1 = a_1\sqrt{\frac{10C}{3\rho}}, \quad c_2 = a_2\sqrt{\frac{10C}{3\rho}}, \text{ and } c_3 = a_3\sqrt{\frac{10C}{3\rho}},$$

and three transversal waves with the velocities

$$c_4 = \sqrt{\frac{C(a_1^2 + a_2^2)}{\rho}}, \quad c_5 = \sqrt{\frac{C(a_1^2 + a_2^2)}{\rho}},$$

and

$$c_6 = \sqrt{\frac{C(a_2^2 + a_3^2)}{\rho}}.$$

The conditions of the static and dynamic [5] stability for the medium under consideration are given by the inequalities

$$A = \sigma_{ij}\varepsilon_{ij} + \mu_{ij}\omega_{ij} > 0,$$

$$b_{1,2} \geq 0, \quad c_i > c_{i+3}, \quad i = 1, 2, 3,$$

which lead to sufficiently rigorous constraints for the isotropy parameter a, namely, $1 \leq a \leq 1.3$.

These constraints for the parameter a are used furthermore for the determination of the simulation boundaries.

Admitting that a only slightly exceeds unity, we can ignore the moment state and assume the interfacial layer to be a transversely isotropic medium whose stiffness coefficients differ from zero and are determined by the expressions

$$c_{11}^e = \frac{10Ca^2}{3}, \quad c_{22}^e = c_{33}^e = \frac{10C}{3a}, \quad c_{12}^e = -\frac{C}{3}\left(a^2 + \frac{1}{a}\right),$$
$$c_{23}^e = -\frac{2C}{3a}, \quad c_{44}^e = c_{55}^e = 2C\left(a^2 + \frac{1}{a}\right), \quad c_{66}^e = \frac{4C}{a}. \quad (6)$$

Here, the constant C can be determined from the sewing conditions for the interfacial layer and the matrix, i.e., $c_{11}^e(a = 1) = 2\mu^m + \lambda^m$.

The initial distribution of stresses in the composite was determined from the static equations

$$\mathrm{Div}\hat{\sigma}^n = 0, \quad \hat{\sigma}^n = \hat{c}^n \mathrm{def}\boldsymbol{u}^n; \quad n = f, e, m, \qquad (7)$$

where $\hat{\sigma}$ is the stress tensor, $\hat{c}$ is the stiffness tensor, and $\boldsymbol{u}$ is the displacement vector.

The conditions for the equality of the axial strains yield $\varepsilon_{ZZ}^n = \varepsilon_0$. From the continuity condition for displacements and radial stresses on the contact surface between the fiber and the interfacial layer, as well as on the phase boundary and the rest of the matrix, it follows that $R = R_f$ and $R = R_f + h$, respectively. For $R = 0$, the condition is given that $\sigma_{ZZ}^f = Pk_S^f$ (where k_S^f is the yield stress for the fiber material). In the case of $R \longrightarrow \infty$, the conditions $\sigma_{RR}^m = \sigma_{RZ}^m = 0$ are given.

The value of P is chosen within the limits $1 < P < \sqrt{3}$. This guarantees that the fiber, the interfacial layer, and the matrix are in the elastic state, and the solution to the static problem can be found in the analytical form. The solution is obtained from Eqs. (7), which are written out for the axisymmetric case and the contact and boundary conditions mentioned above. This solution is obtained by a rather simple but cumbersome method and is, therefore, omitted here.

Dynamic equations. At $t = 0$, there occurs an instantaneous fiber break in the plane $Z = 0$. The redistribution of stresses caused by the break is axisymmetric and is written out using the dynamical equations for elastoplastic media. These equations are of the form

$$\rho_i \partial_t \mathbf{v}^i = \mathrm{Div}\hat{\sigma}^i,$$
$$\partial_t \hat{\sigma}^i = \hat{c}^i \left[\mathrm{def}\mathbf{v}^i - \langle \Phi^i (S^i - k_S^i) \rangle \frac{\hat{s}^i}{\tau_i S^i} \right], \qquad (8)$$

where $\mathbf{v}^i$ is the velocity vector for particles; $\hat{\sigma}^i$ and $\hat{s}^i$ are the stress tensor and the deviator; $\hat{c}^i$ is the stiffness tensor for the fiber and the matrix; $c_{jklm}^i = \lambda^i \delta_{jk}\delta_{lm} + 2\mu^i \delta_{jl}\delta_{km}$; $i = f, m$ (for the interfacial layer, $i = e$); and c_{jklm}^i are the components of the stiffness tensor for a transversely isotropic body. These components can be determined from Eq. (6). Furthermore, $\partial_t = \dfrac{\partial}{\partial t}$; $\langle \Phi^i (S^i - k_S^i) \rangle$ is the operator function responsible for the effect of the plastic-strain rate: $\langle \Phi^i (S^i - k_S^i) \rangle = \Phi^i (S^i - k_S^i) h(S^i - k_S^i)$, where h is the Heaviside function, while Φ^i is a monotonously increasing function of $S^i - k_S^i$ in the case of $S^i \geq k_S^i$; τ_i is a constant with dimensionality [s], which characterizes the viscosity beyond the elasticity region; and S^i is the stress intensity.

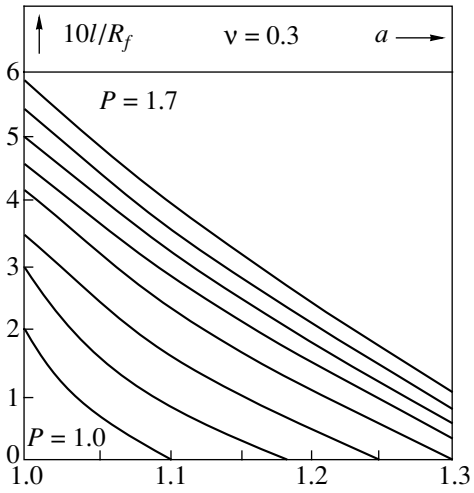

Fig. 2.

The conditions at the contact of an armoring fiber and the interfacial layer are of a complicated nature and can vary in the process solving depending on the fulfillment of criteria for the exfoliation of the fiber from the matrix by means of a break or shear. These criteria are of the form

$$\int_0^t (\sigma^0 - \sigma_{RR}^f) dt > K_\sigma, \quad \int_0^t (\tau^0 - |\sigma_{RZ}^f|) dt > K_\tau, \qquad (9)$$

where four constants σ^0, τ^0, K_σ, and K_τ are chosen experimentally.

At the initial moment, the continuity conditions are satisfied for the break region. After foliation, these conditions are changed by the conditions of a free surface or of Coulomb friction, similarly to as those in [4].

In order to simulate the stress redistribution after the fiber break, the method of spatial characteristics was employed. For points of the interfacial layer, we used intentionally developed algorithms taking into account peculiarities in the structure of the layer and its thinness compared to the fiber radius.

Simulation parameters correspond to the steel fiber and the rubber matrix. They have the form $\nu_f = 0.3$; $\nu_m = 0.495$; $E_{f0} = 19.8 \times 10^5$, $E_m = 9.7 \times 10^2$ t/m^2; $\rho_f = 7.8$, $\rho_m = 1.5$ t/m^3; $k_S^f = 9.8 \times 10^5$, $k_S^m = 20$ t/m^2; $\tau^0 = k_S^f$; $\sigma^0 = \sqrt{3}\, k_S^f$; $K_\sigma = 1.4 k_S^f$; $K_\tau = 1.1 k_S^f$; $R_f = 0.06 l_f$; $\Phi^f = \sqrt{\dfrac{S^f}{k_S^f} - 1}$; and $\Phi^m = \sqrt{\dfrac{S^m}{k_S^m} - 1}$. The length of the fiber is $l_f = 3 \times 10^{-5}$ m; the simulation time is $T = \dfrac{l_f}{c_1}$; the step taken for the simulation is $h_t = 0.005T$; and c_1 is the velocity of longitudinal waves in the fiber.

The results of the simulation are shown in Figs. 2–4. Figure 2 exhibits the plots for the dimensions of the

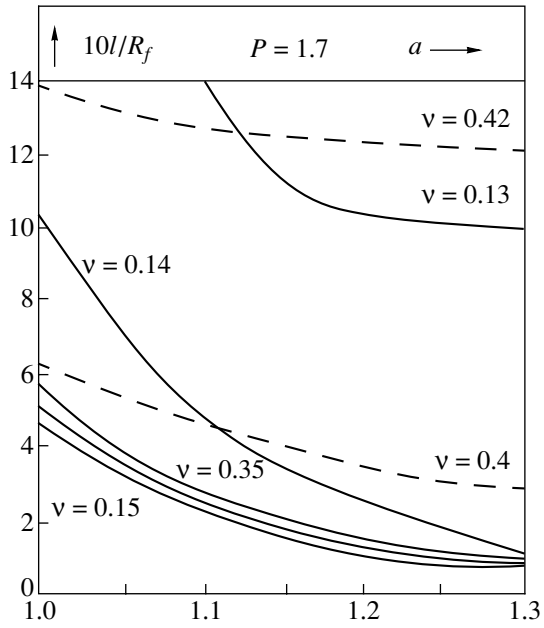

Fig. 3.

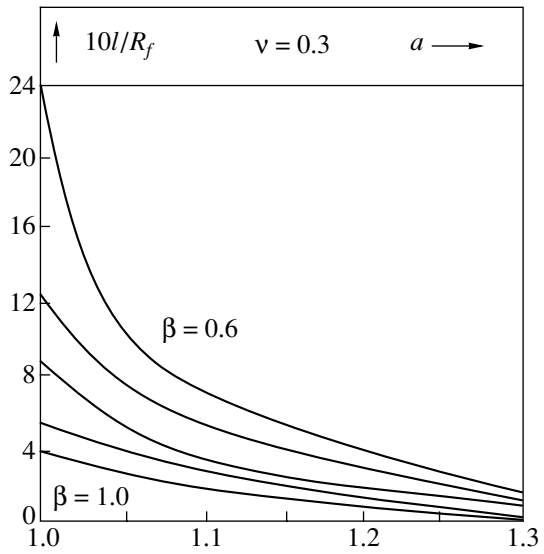

Fig. 4.

region for the exfoliation of the fiber from the matrix as functions of the anisotropy parameter a in the case of different loads $P = 1.0$–1.7 and $\nu_f = 0.3$.

Figure 3 shows the size of the foliation region as a function of a for different Poisson's ratios ν_f of the fiber. In this case, the following values for ν_f are chosen: $\nu_f = 0.13$, 0.14, 0.15, 0.25, 0.35, 0.40, and 0.42.

Analysis of all the plots depicted in the figures shows that with increasing a, the size of the foliation region decreases, and in certain cases ($P = 1.0$ to 1.3, see Fig. 2), the exfoliation ceases altogether. The foliation changes virtually linearly with the load. The dependence of the foliation on the parameter a is also almost linear but slightly descending.

Somewhat more complicated is the dependence of the foliation region on the Poisson's ratio ν_f of the material under a constant load $P = 1.7$. This dependence is rather weak in the region $\nu_f = 0.15$ to $\nu_f = 0.35$. The size of the foliation region sharply increases in the case $\nu_f < 0.15$ and $\nu_f > 0.4$. The dependence disappears in the case of $\nu_f < 0.13$ and $\nu_f > 0.42$.

Figure 4 demonstrates the size of the foliation region as a function of the parameter a for fibers with different Young moduli E_f for $\nu_f = 0.3$ and a constant initial load. A dimensionless parameter $\beta = \dfrac{E_f}{E_{f0}}$ is introduced ($1 \geq \beta \geq 0.6$, where $E_{f0} = 19.8 \times 10^5$ t/m^2 is the fiber Young modulus used in constructing the preceding series of plots). The load is chosen in such a manner that $\dfrac{P}{(E_f)_{\min}} = 1.677$; i.e., the initial loading does not remove the composite materials from the elastic region in the entire variation range of E_f.

Analysis of the plots exhibited in Fig. 4 shows that, first, the foliation region sharply increases with the parameter $\eta = \dfrac{P}{E_f}$. Second, the increase in the anisotropy parameter a is accompanied by a sharp decrease in the foliation, which entirely ceases at $\beta = 0.9$ or 1.0 and $a = 1.3$.

The first tendency may be, apparently, explained by the fact that the Young modulus affects not only the increasing relative load η but (explicitly) the fiber yield stress $k_S^f = \rho_f c_1 v_S^f$ also, which directly participates in all foliation conditions and decreases with a decrease in the Young modulus.

The second tendency shows the positive role of macromolecule additives on the fiber surface in providing the contact between the fiber and the matrix. The effect of the anisotropy parameter a turns out to be more noticeable, the higher the relative load η is.

REFERENCES

1. *Structure and Properties of Polymeric Surface Layers*, Ed. by Yu. S. Lipatov (Naukova Dumka, Kiev, 1972).
2. V. É. Zgaevskiĭ and Yu. G. Yanovskiĭ, Mekh. Kompoz. Mater. Konstr. **3** (1), 105 (1997).
3. G. G. Bulychev, Izv. Akad. Nauk, Mekh. Tverd. Tela, No. 1, 91 (1995).
4. G. G. Bulychev and V. N. Kukudzhanov, Izv. Akad. Nauk, Mekh. Tverd. Tela, No. 3, 169 (1993).
5. G. I. Petrashen', *Propagation of Waves in Anisotropic Elastic Media* (Nauka, Leningrad, 1980).

Translated by G. Merzon

Doklady Physics, Vol. 46, No. 7, 2001, pp. 499–503. Translated from Doklady Akademii Nauk, Vol. 379, No. 1, 2001, pp. 54–58.
Original Russian Text Copyright © 2001 by Grigoryan.

MECHANICS

The Solution to the Painleve Paradox for Dry Friction

Academician S. S. Grigoryan

Received March 2, 2001

The so-called Painleve paradox [1] has been known for more than a hundred years. It implies that, for certain combinations of initial parameters, there is no solution to some problems of theoretical mechanics in which the dry-friction force defined quantitatively by the Coulomb law acts along with other forces. Many attempts have been undertaken to solve this paradox by taking into account a variety of additional factors (elasticity and so on) that are ignored in the classical formulation of the problem; however, no success has been achieved. In this paper, we give a simple and natural explanation of the source of this paradox and its elimination.

The Painleve paradox is routinely analyzed by invoking the following example. A rigid segment of length $2l$ is arranged between two rigid parallel guiding straight lines at a tilt angle α to these guides. The segment rests on by its ends on the guides and bears a localized mass m in its middle. The contact of the guide with one of the supporting points is perfectly smooth (the friction force is absent); at another point, a friction force F_f related to a normal force N by the Coulomb law can arise:

$$F_f = -k|N|\operatorname{sgn} v, \tag{1}$$

where k is the friction coefficient and

$$\operatorname{sgn} v = \begin{cases} 1, & v > 0 \\ -1, & v < 0. \end{cases} \tag{2}$$

An external force F_e parallel to the guides is applied to the segment at a distance a from its middle. The scheme of the problem is shown in Fig. 1. It is necessary to find the law of motion of the segment bearing a mass m along the guides for the given initial conditions and to determine the forces N and F_f.

The equation of motion has the form

$$m\frac{dv}{dt} = F_e + F_f, \tag{3}$$

and the condition of equality to zero for the net moment of forces acting upon the system is reduced to the form

$$F_f = qN - \lambda F_e, \quad q = \frac{2}{\tan\alpha}, \quad \lambda = \frac{a}{l}. \tag{4}$$

The parameters q and λ vary within the range

$$\begin{aligned} -\infty \le q \le \infty \quad (0 \le \alpha \le \pi), \\ -1 \le \lambda \le 1 \quad (-l \le a \le l). \end{aligned} \tag{5}$$

To solve the problem, the forces N and F_f must be found from (1) and (4), whereupon the integration of (3) for $v(0) = v_0$ determines the law of motion. To analyze the process of determining N and F_f, it is convenient to show relationships (1) and (4) on the (N, F_f) plane (Fig. 2). In this figure, the straight lines AA, A_*A_*, and A_0A_0 represent the graphs of relationship (4) for $q > k$, $q = k$, and $0 < q < k$, respectively; the straight lines OQ, $O\bar{Q}$ represent the graph of (1) for $v < 0$; the straight lines OQ_1 and $O\bar{Q}_1$, for $v > 0$. The plots correspond to the case $\lambda F_e > 0$ (point O_1). Similar graphs can also be plotted for $\lambda F_e < 0$ (point O_2) and for $q < 0$.

The formulation of the problem has the sense both for $N \ge 0$ (case I) when the segment with a mass m rests on the guides from inside and can turn inward with a departure of its ends from the guides and for $N \le 0$ (case II) when the segment rests on the guides from outside and can turn outward with its ends being removed from the guides. The second case is realized in the construction scheme, in which a slot extends along each of the guides through which the segment end having a supporting element outside the guide passes; this sup-

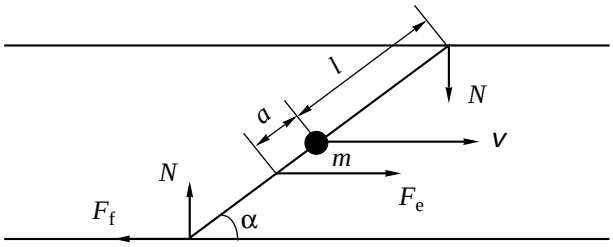

Fig. 1.

Institute of Mechanics, Moscow State University, Michurinskiĭ pr. 1, Moscow, 117192 Russia

1028-3358/01/4607-0499$21.00 © 2001 MAIK “Nauka/Interperiodica”

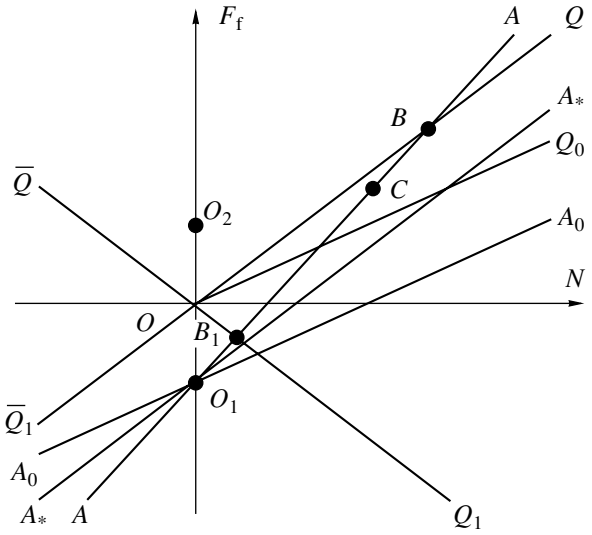

Fig. 2.

port is in contact with the external surface of the guide. Combined support is also possible: either end of the segment bears a ring put on the guide—a rod (an unreleasing constraint). In this scheme, both cases are realized: $N \geq 0$ and $N \leq 0$.

It follows from Fig. 1 that the case $N \geq 0$ is realized for $\lambda q F_e > 0$ and the case II ($N \leq 0$) for $\lambda q F_e < 0$. If the segment rests on the guides from inside but $\lambda q F_e < 0$, an instantaneous turn (the moment of inertia of the system with respect to the point of arrangement of the localized mass is zero) occurs at the initial time instant with α vanishing or being equal to π also for $N = F_f = 0$, after which the problem is reduced to solving Eq. (3) for $F_f = 0$ and $v(0) = v_0$. The same takes place when the segment rests on the guide from outside and the inequality $\lambda q F_e > 0$ is obeyed. These degenerate cases are of no interest. For the combined unreleasing support, no degeneration occurs and the sign of N coincides with the sign of $\lambda q F_e$.

Thus, for the case of internal support, it is necessary to analyze only the right-hand side of Fig. 2 ($N > 0$), while, for the case of external support it is necessary to analyze only the left-hand side ($N < 0$) with the corresponding disposition of analogues of the straight lines, AA, A_*A_*, and A_0A_0. (Note that the lower portions of these lines, AO_1, A_*O_1, and A_0O_1, are of no physical meaning by virtue of the classification of cases I and II according to the sign of $\lambda q F_e$.)

Further, we restrict our consideration to case I, which is shown on the right-hand side of Fig. 2. For $q > k$, the straight line O_1A intersects the straight lines OQ and OQ_1 at points B and B_1, respectively. The solution corresponding to point B relates to the case when the initial velocity of the system is negative: $v_0 < 0$. If $F_e > 0$ is valid, and, thus, $\lambda > 0$ (we recall that $N > 0$; i.e., the condition $\lambda q F_e > 0$ must be fulfilled), while $F_e + F_{fB} > 0$ at point B, the solution to Eq. (3) is determined by the relationship

$$v = v_0 + \frac{1}{m}(F_e + F_{fB})t. \tag{6}$$

Therefore, at first, the braking of the system takes place over a finite time,

$$\tau = -\frac{m v_0}{F_e + F_{fB}}, \tag{7}$$

at which its velocity vanishes and after which the velocity becomes positive. This is possible if the point representing the state of the system at the (N, F_f) plane passes in a jumplike fashion (along O_1A) into point B_1 where $F_f = F_{fB_1} < 0$. However, $|F_{fB_1}| < |F_{fO_1}| = \lambda F_e < F_e$, which means that $F_e + F_{fB_1} > 0$. Actually, according to the solution to Eq. (3) for $t > \tau$ having the form

$$v = \frac{1}{m}(F_e + F_{fB_1})(t - \tau), \quad t \geq \tau, \tag{8}$$

we have $v > 0$, and, for $t > \tau$, an unlimited speed-up of the system with a positive acceleration will take place.

In the case $F_e < 0$ (when λ is also negative to ensure that $\lambda q F_e > 0$), the situation is different. If q is reasonably large, point B is close to point O so that $F_{fB} < |F_e|$; i.e., $F_e + F_{fB} < 0$ and, according to the solution to Eq. (3) having form (6), the system speeds up infinitely to the left with a negative acceleration. For a certain value $q = \tilde{q}$, $\tilde{F}_{fB} = |F_e|$, i.e., $\tilde{F}_{fB} + F_e = 0$, the acceleration vanishes in solution (6) and the initial velocity is retained at all moments of time. For $q < \tilde{q}$, we have $F_{fB} > |F_e|$, $F_e + F_{fB} > 0$, the acceleration is positive in solution (6), and the modulus of velocity reduces and vanishes over a finite time τ determined using formula (7). The extension of the solution into the region $v > 0$ by introducing a jumplike transition from point B to point B_1 along line O_1A becomes impossible in this case because $F_{fB_1} < 0$ at point B_1 and, thus, $F_e + F_{fB_1} < 0$; i.e., the acceleration is negative and the velocity cannot pass into the region $v > 0$. This difficulty is removed by assuming that, at the instant $t = \tau$, the jump is accomplished along O_1A on the (N, F_f) plane not to point B_1 but to a certain intermediate point C, where $F_f = F_{fC} > 0$ and $F_e + F_{fC} = 0$, so that the acceleration vanishes and no further motion takes place. This assumption is plausible because Coulomb law (1) allows all the states to lie in

the straight line O_1A corresponding to segment BB_1 (all the states in the regions between the straight lines OQ and OQ_1 for $N > 0$ in which $v = 0$ and the value of $\operatorname{sgn} v$ can be arbitrary within [–1, 1]).

Point B_1 on the (N, F_f) plane corresponds to the case $v_0 > 0$. In this case, for all the values of $q > 0$ and $F_e > 0$ (and, thus, for $\lambda > 0$), the inequality $F_e + F_{fB_1} > 0$ is satisfied and the solution is given by the relationship

$$v = v_0 + \frac{1}{m}(F_e + F_{fB_1})t, \qquad (9)$$

according to which the system undergoes an indefinite speed-up with a constant acceleration. If $F_e < 0$ (and, thus, $\lambda < 0$), the acceleration is negative (because $F_{fB_1} < 0$ and $F_e + F_{fB_1} < 0$), the system slows down, and, over a finite time τ also determined from (7), its velocity vanishes. The subsequent behavior depends on inequality $F_{fB} < |F_e|$ or $F_{fB} > |F_e|$ being fulfilled on passage from point B_1 to point B. In the first of these events corresponding to reasonably large values of q, we have $F_e + F_{fB} < 0$, the velocity becomes negative, and the system begins to infinitely speed up to the left with a constant acceleration. For $F_{fB} = |F_e|$, i.e., for $q = \tilde{q}$, the state of rest attained at $t = \tau$ is retained also at $t > \tau$. When $F_{fB} > |F_e|$, a jumplike transition takes place at $t > \tau$ into the intermediate point C of segment B_1, where $F_f = F_{fC} = -F_e$, and, further, the state of rest is retained at $t > \tau$.

The principal result of the above analysis is that, for $q > k$ and arbitrary values of other parameters of the problem, its solution exists and is unique, but a discontinuous change in the parameters involved is observed in the mode of motion of the system under certain conditions.

We consider now what happens with the solution when $q \longrightarrow k$ (in the region of $q > k$). From Fig. 2 it can be seen that, in this case, the straight line O_1A takes the position O_1A_* and point B goes to infinity while moving along the straight line OQ; i.e., we obtain $N_B \longrightarrow \infty$, $F_{fB} \longrightarrow \infty$ for $q \longrightarrow k$, whereas point B_1 shifts along the straight line OQ_1 to a certain limiting position. The solution described above and its properties for all sets of other parameters are retained. However, the time τ required to extinguish the initial velocity, when it exists, vanishes. In this case, the moment of force F_f tending to infinity for $q \longrightarrow k$ remains finite: according to (7),

$$\tau(F_e + F_{fB}) = -mv_0 = \text{const}.$$

Finally, for $q < k$, the straight line O_1A occupies the position O_1A_0 and point B ceases to exist. This means that, for those sets of parameters of the problem for which the existence of point B was obligatory in constructing the solution described above, this solution also ceases to exist. The Painleve paradox is made up of this alone. To resolve it, one should assume that it is necessary to introduce infinite initial values of N and F_f for $q < k$ with a finite momentum, which extinguish the "ill" values of the initial velocity v_0 in a jumplike manner, thus improving the situation at hand. However, this is not the case.

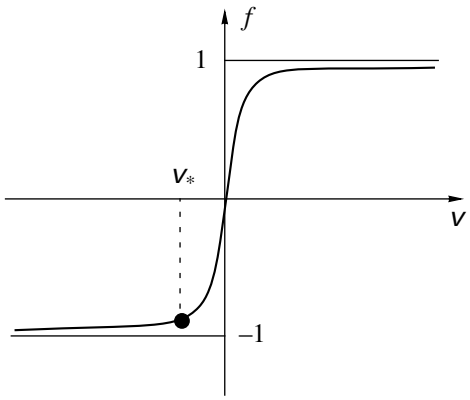

Fig. 3.

In order to be certain of this, we use a more realistic approach to the problem by replacing the discontinuous function $\operatorname{sgn} v$ in (1) with a continuous function $f(v)$ that is, however, very close to it; the $f(v)$ function is shown schematically in Fig. 3. In such a setting of the law of friction, i.e., for

$$F_f = -k|N|\,f(v), \qquad (10)$$

the solution to set (4), (10) for $N > 0$ takes the form

$$N = \frac{\lambda F_e}{q + k f(v)}, \quad F_f = -\frac{k\lambda F_e f(v)}{q + k f(v)}, \qquad (11)$$

and the problem is reduced to integrating the equation

$$\frac{dv}{dt} = \frac{1}{m}(F_e + F_f) = \frac{F_e}{m}\frac{q + k(1-\lambda) f(v)}{q + k f(v)} \qquad (12)$$

for $v(0) = v_0$.

On the (N, F_f) plane, the contours $v = \text{const}$ of the function in (10) are the beams radiating from point O in the region between OQ and OQ_1; the beams with $v < 0$ lie in the region $F_f > 0$, and the beams with $v > 0$ are in the region $F_f < 0$. The assignment of the initial velocity v_0 determines the point of intersection between the beam with $f = f(v_0)$ and the straight line O_1A, while the integration of (12) gives results close to the solution described above but replacing the jumps existing

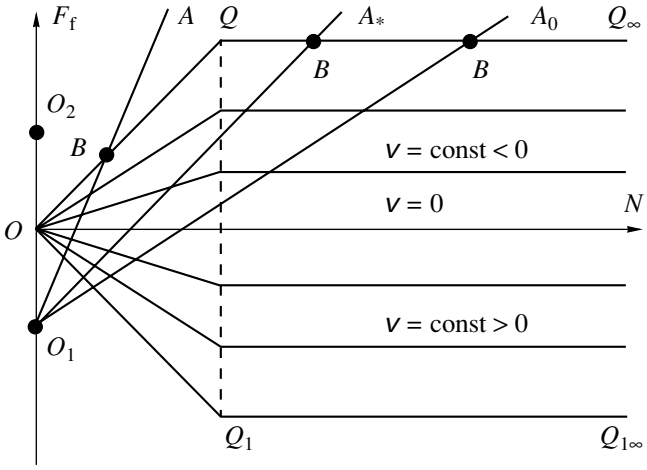

Fig. 4.

therein (from B to B_1, from B_1 to B, or from B or B_1 to C) with continuous transitions.

Addressing the case $q < k$, we can see that the condition $q + kf(v_0) > 0$ is valid and the values of $N(v_0)$ and $F_f(v_0)$ are positive only for a finite set of values of the initial velocity $v_0 > v_*$, $v_* < 0$, while, for $v_0 \longrightarrow v_*$ $N \longrightarrow \infty$ and $F_f \longrightarrow \infty$, according to formulas (11). Otherwise, only the beams with $v_0 > v_*$ intersect the straight line O_1A_0, while the beam $v_0 = v_*$ is parallel to this straight line. Only for the initial values $v_0 > v_*$ does there exist a solution to Eq. (12). For the values v_0 from the interval $-\infty < v_0 < v_*$, there is no solution; in Fig. 2, the angular region QOQ_0 corresponds to this case (OQ_0 is the beam that is parallel to O_1A_0).

Thus, the Painleve paradox—the absence of a solution for the values $q < k$ in considering the problem with a more "realistic" continuous dependence of the friction force on velocity—is retained within the range of initial velocities $-\infty < v_0 < v_*$. From Fig. 3 it can be seen that, when the continuous function $f(v)$ tends to a limiting one, i.e., to the discontinuous function $f(v) = \operatorname{sgn} v$, the value of v_* goes to zero, the entire fan of the beams with $v_0 < 0$ assembles in a limiting beam with $f = -1$, and the entire set of initial velocities $v_0 < 0$ becomes the region of nonexistence of the solution. Therefore, the above hypothetical possibility of removing the paradox by introducing initial jumps with a finite momentum in order to extinguish the initial velocity $v_0 < 0$ turns out to be unacceptable.

To solve the paradox, we return to the fact that the values N and F_f become infinite for $q \longrightarrow k$ from the region $q > k$, where the solution exists. From deformable body mechanics and from solid state physics in general, it is known that, whereas the normal stresses (pressures) can be arbitrarily large in a solid, its tangential stresses, in particular, the dry-friction forces on the surface of contact of these bodies, are restricted by their strength. Therefore, Coulomb law (1), according to which the friction force F_f (the shear stress) can rise infinitely with an increase in the normal force N (a normal stress), cannot be applied for large values of N. For each particular material there exists a finite value of N, the excess of which in its friction with other, stronger material leads to a deviation from the Coulomb law, while, for $N \longrightarrow \infty$, we have $F_f \longrightarrow F_\infty$, where F_∞ is a finite limiting value—a characteristic of the given material. As a simple approximation to the real law of friction, we can use the relationship

$$F_f = \begin{cases} -k|N| \operatorname{sgn} f(v), & |N| < N_* \\ -kN_* \operatorname{sgn} f(v) \equiv -F_\infty \operatorname{sgn} f(v), & |N| > N_*. \end{cases} \quad (13)$$

This modification in the dry-friction law [Coulomb law (1)] was proposed by the author [2] to explain and quantitatively describe the effect of the anomalously high mobility of large-scale landslides arising in mountains during violent earthquakes and powerful explosions deep in the mountain mass and in the case of impacts of large celestial objects on the surface of solid planetary bodies. In the last case, this mobility determines the morphological features of impact craters (central hills, annular rims, and large-scale dammed landslides). Direct confirmation of law (13) in the experiment with homogeneous materials (instead of crushed rock) was also obtained [3].

The use of (13) instead of (1) immediately eliminates the Painleve paradox. This is shown in Fig. 4, similarly to in Fig. 2, where the broken lines OQQ_∞ and $OQ_1Q_{1\infty}$ (the true curves are smooth lines close to these broken lines) are shown instead of the straight lines OQ and OQ_1. It is also seen that, for all $0 \le q \le \infty$ and all values of other parameters, there exist intersections on the graph (4), the straight lines O_1A, O_1A_*, O_1A_0 (points B) with these broken lines. The region between OQQ_∞ and $OQ_1Q_{1\infty}$ in Fig. 4 is filled with lines of the level v = const of the function $F_f = F_f(N, v)$ given by formulas (13), in which the discontinuous $\operatorname{sgn} x$ function is replaced by the continuous function $f(v)$ and which also represent the broken lines. Using them allows one to construct, as for (10), the solution to the problem that is continuous in v.

The above analysis pertains to case (1): $N > 0$, $\lambda F_e > 0$, and $q > 0$. Quite similar results are obtained for the remaining cases: (2) $N > 0$, $\lambda F_e < 0$, and $q < 0$; (3) $N < 0$, $\lambda F_e > 0$, and $q < 0$; and (4) $N < 0$, $\lambda F_e < 0$, and $q > 0$. These cases are obtained in Fig. 2 from the case shown by means of specular reflections with respect to the axes ON, OF_f, and by means of double reflection with respect to axis ON and, then, to axis OF_f, which follows from the invariance of set (3), (4) with respect

to such transformations. In all these cases, the situation is entirely similar: for one set of values of the parameters of the problem, the solution exists and is unique; for the remaining values, there is no solution; i.e., the Painleve paradox arises. The change from one of these situations to another takes place at the boundary $|q| = k$. The paradox is eliminated by replacing the Coulomb law for the dry friction by the physically realistic law proposed in [2] with a limiting value of the friction force attained at large values of the normal force on the friction surfaces.

REFERENCES

1. P. Painleve, *Léçons sur le frottement* (Hermann, Paris, 1895; Gostekhizdat, Moscow, 1954).
2. S. S. Grigoryan, Dokl. Akad. Nauk SSSR **244**, 246 (1979) [Sov. Phys. Dokl. **24**, 110 (1979)].
3. V. A. Ioselevich, N. N. Pilyugin, and S. Yu. Chernyavskiĭ, Prikl. Mekh. Tekh. Fiz., No. 5, 73 (1978).

Translated by V. Bukhanov

Doklady Physics, Vol. 46, No. 7, 2001, pp. 504–507. Translated from Doklady Akademii Nauk, Vol. 379, No. 1, 2001, pp. 59–62.
Original Russian Text Copyright © 2001 by Nemirovskiĭ.

MECHANICS

Lower Bounds of Ultimate Loads for Perfectly Plastic Homogeneous and Inhomogeneous Structures

Yu. V. Nemirovskiĭ

Presented by Academician A.Yu. Ishlinskiĭ February 12, 2001

Received February 22, 2001

The determination of upper and lower bounds for the bearing capacity of perfectly plastic structures is associated with the construction of kinematically admissible velocity fields and statically admissible stress fields, respectively. Whereas it is usually easy to find the upper bound, the determination of the lower bounds presents considerable difficulties. Indeed, the stress fields found in a plastic range must be continuable into an elastic range, while the plasticity condition has to be satisfied everywhere [1]. For structures made of homogeneous materials and subjected to simple or combined-mode loadings, the certain simplest problems of determining statically admissible and exact values for the ultimate loads were considered in [2, 3]. Searching the lower bounds for inhomogeneous structures has not attracted sufficient attention, although a great many of these structures, during their fabrication and use, become essentially inhomogeneous because temperature fields, irradiation, ultrasonic machining, and other external fields significantly influence the yield stress.

In this paper, we propose a simple method of estimating the lower bounds of the bearing capacity for homogeneous and inhomogeneous structures subjected to combined-mode loadings.

Let us consider a perfectly plastic body occupying the domain Ω bounded by the surface $\Gamma = \Gamma_u \cup \Gamma_F$, $\Gamma_u \cap \Gamma_F = \varnothing$. The part Γ_u of the boundary is rigidly fixed, while the remaining part Γ_F can be subjected to the loads $F_k^{(m)}(*)$ [$m = 1, 2, \ldots, M$; $k = 1, 2, 3$; and $(*) \in \Gamma_F$].

We assume that the lower bound of the ultimate-load coefficient $\alpha_m^0 \le \alpha_m$ is determined for each separately applied load $F_k^{(m)}$ (in particular, the exact value of α_m can be known). Then, there exists a statically admissible stress field $\sigma_{kl}^{(m)}$ ($k, l = 1, 2, 3$) such that

$$\sigma_{kl}^{(m)}(*)n_l = \alpha_m^0 F_k^{(m)}(*),$$

$(*) \in \Gamma_F$ (summation over m is not performed),

$$f(\sigma_{kl}^{(m)}(*)) \le Y(*), \quad (*) \in \Omega.$$

Here, $f(\sigma_{kl})$ is a positively homogeneous first-power function determining the yield surface shape, $Y(*)$ is the variable yield stress, and n_l are the direction cosines of the outward normal to the surface Γ_F.

Let a linear combination of the loads $F_k^{(m)}$,

$$F_k = \sum_{m=1}^{M} \gamma_m F_k^{(m)} \text{ with } \gamma_m = \text{const}$$

be applied to Γ_F. Then, introducing the notation $\sigma_{kl} = \sum_{m=1}^{M} \frac{\gamma_m \sigma_{kl}^{(m)}}{\alpha_m^0}$, we have

$$\alpha_* = \alpha_0 \min_{(*) \in \Omega} \frac{Y(*)}{f(\sigma_{kl}(*))} \ge \alpha_0 = \left(\sum_{m=1}^{M} \frac{\gamma_m}{\alpha_m^0} \right)^{-1}. \quad (1)$$

The stress field $\alpha_* \sigma_{kl}$ is statically admissible for the boundary load $\alpha_* F_k(*)$. Consequently, it defines the lower bound of the ultimate coefficient α for the load F_k:

$$\alpha \ge \alpha_* \ge \alpha_0. \quad (2)$$

Thus, being known, the values of the constants α_m^0 and γ_m are sufficient for the lower bound to be determined in the case of combined-mode loadings. To estimate α_* more accurately, the statically admissible stress fields $\sigma_{kl}^{(m)}$ have to be determined also, with the value of α_* being dependent on them. The above-presented results show that if the loads are ultimate and the

Institute of Applied Mechanics, Siberian Division, Russian Academy of Sciences, Novosibirsk, Russia

1028-3358/01/4607-0504$21.00 © 2001 MAIK “Nauka/Interperiodica”

conditions $\gamma_m \geq 0$ and $\sum_{m=1}^{M} \gamma_m \leq 1$ are satisfied, then the load $F_k = \sum_{m=1}^{M} \gamma_m F_k^{(m)}$ is either safe or ultimate.

Let the series $\sum_{m=1}^{\infty} \gamma_m F_k^{(m)}$ $(\gamma_m \geq 0)$ weakly converge to $F_k(*)$ [in the sense of the convergence in $L_2(\Gamma_F)$]. It follows from the virtual-velocity and maximum principles that

$$\alpha \int_{\Gamma_F} F_k u_k d\Gamma_F \geq \alpha^{(M)} \int_{\Gamma_F} \sum_{m=1}^{M} \gamma_m F_k^{(m)} u_k d\Gamma_F. \qquad (3)$$

Here, α and $\alpha^{(M)}$ are the ultimate coefficients for the loads F_k and $\sum_{m=1}^{\infty} \gamma_m F_k^{(m)}$, respectively, and u_k are the velocity fields under the limiting conditions corresponding to the loads αF_k. According to inequalities (1), we have

$$\alpha^{(M)} \geq \left(\sum_{m=1}^{M} \frac{\gamma_m}{\alpha_m^0} \right)^{-1},$$

and, consequently, inequalities (2) lead to the relation

$$\alpha \geq \int_{\Gamma_F} \sum_{m=1}^{M} \gamma_m F_k^{(m)} u_k d\Gamma_F \left(\int_{\Gamma_F} F_k u_k d\Gamma_F \right)^{-1} \left(\sum_{m=1}^{M} \frac{\gamma_m}{\alpha_m^0} \right)^{-1}.$$

Proceeding to the limit as $M \longrightarrow \infty$, we find that

$$\alpha \geq \alpha_0 = \left(\sum_{m=1}^{\infty} \frac{\gamma_m}{\alpha_m^0} \right)^{-1}. \qquad (4)$$

Passing to the limit, we extend this estimate to loads of the form

$$F_k(*) = \int_c^d F_k(\lambda, (*)) d\gamma(\lambda), \quad \lambda \in [c, d], \quad (*) \in \Gamma_F,$$

where the function $F_k(\lambda, (*))$ is assumed to be integrable in the sense of Riemann–Stieltijes over $[c, d]$ at almost all points $(*) \in \Gamma_F$. Then, the corresponding estimate takes the form

$$\alpha \geq \alpha_0 = \left(\int_c^d \frac{1}{\alpha^0(\lambda)} d\gamma(\lambda) \right)^{-1}. \qquad (5)$$

Here, $\alpha^0(\lambda)$ is the lower bound of the ultimate coefficient $\alpha(\lambda)$ for the load $F_k(\lambda, (*))$: $\alpha(\lambda) \geq \alpha^0(\lambda)$, $\lambda \in [c, d]$), while $\sigma_{kl}(\lambda, (*))$ are the corresponding statically admissible stress fields for the load $\alpha^0 F_k(\lambda)$.

As an example, we now determine a lower bound of the ultimate-load coefficient for a homogeneous prismatic bar subjected to the joint action of an axial force $N^{(1)} = N$ and torque $M^{(1)} = M$, both varying proportionally to a parameter. Being applied separately to the bar, with its cross section bounded by the circumference $x_1^2 + x_2^2 = a^2$, these loads lead to the relations [2]

$$\alpha_1^0 = \frac{\pi a^2 Y_0}{|N|}, \quad \alpha_2^0 = \frac{2\pi a^3 Y_0}{|3\sqrt{3}M|},$$

where Y_0 is the yield stress corresponding to axial tension. In the case of the joint action of the axial force and the torque ($\gamma_1 = \gamma_2 = 1$), according to (1) and (2), the ultimate coefficient can be estimated as

$$\alpha \geq \alpha_0 = \frac{2\pi a^3 Y_0}{2a|N| + 3\sqrt{3}|M|}.$$

Under the limiting conditions corresponding to the separate action of the axial force and the torque, the stress fields are

$$\sigma_{33}^{(1)} = Y_0 \operatorname{sgn} N,$$

$$\sigma_{11}^{(1)} = \sigma_{22}^{(1)} = \sigma_{12}^{(1)} = \sigma_{13}^{(1)} = \sigma_{23}^{(1)} = 0,$$

$$\sigma_{13}^{(1)} = \frac{Y_0}{\sqrt{3}} \frac{x_2 \operatorname{sgn} M}{\sqrt{x_1^2 + x_1^2}}, \quad \sigma_{23}^{(1)} = \frac{Y_0}{\sqrt{3}} \frac{x_1 \operatorname{sgn} M}{\sqrt{x_1^2 + x_1^2}},$$

$$\sigma_{11}^{(2)} = \sigma_{22}^{(2)} = \sigma_{12}^{(2)} = \sigma_{33}^{(2)} = 0.$$

They allow the following more accurate estimate to be derived:

$$\alpha \geq \alpha_* = \alpha_0 \min_{\Omega} \left(\frac{Y_0}{\sqrt{\sigma_{33}^2 + 3(\sigma_{13}^2 + \sigma_{23}^2)}} \right),$$

$$\sigma_{kl} = \alpha_0 \left(\frac{\sigma_{kl}^{(1)}}{\alpha_1} + \frac{\sigma_{kl}^{(2)}}{\alpha_2} \right).$$

Thus,

$$\alpha \geq \alpha_* = \frac{2\pi a^3 Y_0}{\sqrt{4a^2 N^2 + 27M^2}}.$$

We can see that this estimate of α_* essentially coincides with the exact solution presented in [2].

For a bar with a rectangular cross section bounded by the straight lines $2|x_1| = b$ and $2|x_2| = a$ $(b \geq a)$, we have [2]

$$\alpha_1^0 = \frac{abY_0}{|N|}, \quad \alpha_2^0 = \frac{a^2(3b - a)Y_0}{|12\sqrt{3}M|}.$$

Then, for the combined action of the axial force N and

the torque M, we derive the estimate

$$\alpha \geq \alpha_0 = \frac{a^2 b(3b-a)Y_0}{a(3b-a)|N| + 12\sqrt{3}|M|}.$$

In this case, the estimate for α_* takes the form

$$\alpha \geq \alpha_* = \frac{a^2(3b-a)Y_0}{\sqrt{a^2(3b-a)^2N^2 + 432b^2M^2}}.$$

As a second example, we consider a simply supported round plate ($0 \leq r \leq b$) of thickness $2h$ subjected to a normal distributed load $F(r)$.

Consider first the auxiliary system of the loads:

$$F(\lambda, r) = \begin{cases} p(\lambda), & r < \lambda \\ 0, & r \geq \lambda, \quad 0 \leq \lambda \leq b, \end{cases}$$

where $p(\lambda)$ is a certain function. Under the Tresca yield condition, the ultimate coefficient for loads of this type is equal to ([2])

$$\alpha(\lambda) = \frac{6bh^2Y_0}{\lambda^2(3b-2\lambda)|p(\lambda)|}.$$

Let $F(r)$ be a piecewise smooth function continuous on the right and having a finite number of jump discontinuities. We present it as the Riemann–Stieltijes integral

$$F(r) = \int_0^b F(\lambda, r)d\gamma(\lambda) = \int_r^b p(\lambda)d\gamma(\lambda).$$

To do this, we introduce the functions $p(\lambda)$ and $\gamma(\lambda)$ in the following way:

$$p(\lambda) = -F'(\lambda), \quad \lambda \neq r_0, r_1, \ldots, r_M;$$

$$p(r_0) = 0, \quad p(r_i) = F(r_i - 0) - F(r_i), \quad i = 1, 2, \ldots, M-1;$$

$$p(r_M) = F(r_M - 0),$$

$$\gamma(r_M) = b + M, \quad \gamma(\lambda) = i + \lambda, \quad \lambda \in [r_i, r_{i+1}].$$

Here, $0 = r_0 < r_1 < \ldots < r_M = b$ are the discontinuity points of either the function $F(r)$ or its derivative.

Then, according to formula (5), the lower bound of the bearing-capacity coefficient takes the form

$$\alpha \geq \alpha_0 = 6bh^2Y_0\left(\int_0^b \lambda^2(3b-2\lambda)|p(\lambda)|d\gamma(\lambda)\right)^{-1}.$$

In particular, if the load $F(r)$ is distributed under the linear law $F(r) = p_1 + \frac{(p_2 - p_1)r}{b}$ ($p_i = \text{const}$, $i = 1, 2$), we assume that

$$p(\lambda) = \frac{p_1 - p_2}{b}, \quad \lambda \in [0, b), \quad p(b) = p_2,$$

$$\gamma(\lambda) = \lambda, \quad \lambda \in [0, b), \quad \gamma(b) = b + 1.$$

In this case, we obtain the estimate $\alpha \geq \alpha_0 = \frac{12h^2Y_0}{b^2(2|p_2| + |p_1 - p_2|)}$.

Now, we consider a rectangular plate $0 \leq x_1 \leq a$, $0 \leq x_2 \leq b$ of constant thickness $2h$ hinged at each point of its contour and subjected to a distributed surface load $q(x_1, x_2)$. The equation of its plastic equilibrium can be written as

$$M_{11,11} + 2M_{12,12} + M_{22,22} = -q(x_1, x_2),$$

where a subscript after a comma denotes a partial derivative with respect to the variable x_k ($k = 1, 2$).

We introduce the following torque distribution in the plate:

$$M_{kk} = \beta c_k \sin\frac{n\pi x_1}{a}\sin\frac{m\pi x_2}{b}, \quad \beta = \pm 1, \quad k = 1, 2,$$
$$M_{12} = \beta c_3 \cos\frac{n\pi x_1}{a}\cos\frac{m\pi x_2}{b}. \tag{6}$$

It corresponds to the load

$$q^0(x_1, x_2) = \beta A_{nm}\sin\frac{n\pi x_1}{a}\sin\frac{m\pi x_2}{b},$$

$$A_{nm} = \pi^2\left(c_1\frac{n^2}{a^2} + c_2\frac{m^2}{b^2} + 2c_3\frac{nm}{ab}\right).$$

The torque field (6) will be statically admissible if the plasticity condition

$$M_{11}^2 - M_{11}M_{22} + M_{22}^2 + 3M_{12}^2 \leq M_0^2 \tag{7}$$

is satisfied everywhere in the plate, where $M_0 = \sigma_0 h^2$ is the ultimate value of the bending moment under cylindrical bending. Substituting (6) into (7) yields

$$(c_1^2 - c_1c_2 + c_2^2)\sin^2\frac{n\pi x_1}{a}\sin^2\frac{m\pi x_2}{b}$$
$$+ 3c_3^2\cos^2\frac{n\pi x_1}{a}\cos^2\frac{m\pi x_2}{b} \leq M_0^2.$$

This inequality will be satisfied everywhere in the plate if

$$c_1^2 - c_1c_2 + c_2^2 \leq M_0^2, \quad 3c_3^2 \leq M_0^2. \tag{8}$$

We find the maximum value of the quantities A_{nm}, considered as functions of the parameters c_1, c_2, and c_3 under the restrictions imposed (8), and then derive the

following estimate for the coefficient α_{nm} of the ultimate load $q_{nm} = \sin\frac{n\pi x_1}{a}\sin\frac{m\pi x_2}{b}$:

$$\alpha_{nm} \geq \alpha_{nm}^0 = \frac{\pi^2 M_0}{\sqrt{3}}\left(\sqrt{3\left(\frac{n^2}{a^2}+\frac{m^2}{b^2}\right)^2+\left(\frac{n^2}{a^2}-\frac{m^2}{b^2}\right)^2}+\frac{2nm}{ab}\right).$$

Now, we represent the load applied to the plate as a double Fourier series

$$q(x_1, x_2) = \sum_{n=1}^{\infty}\sum_{m=1}^{\infty}\gamma_{nm}\sin\frac{n\pi x_1}{a}\sin\frac{m\pi x_2}{b}.$$

To estimate the ultimate-load coefficient for $q(x_1, x_2)$, the numerical series should be summed:

$$\alpha \geq \alpha_0 = \left(\sum_{n=1}^{\infty}\sum_{m=1}^{\infty}\frac{|\gamma_{nm}|}{\alpha_{nm}^0}\right)^{-1}.$$

For bodies with inhomogeneous plastic properties described by an inhomogeneity function fixed beforehand, solutions to the problems of their ultimate equilibrium are, because of the difficulties arising, similar to an accidental spread of the results (which were reviewed in [4]). Therefore, it is difficult to use these solutions in order for the lower bounds of ultimate loads to be obtained for a wide range of structural elements, conditions of their operation, and inhomogeneity types. However, there is another approach to solving the problem, which consists in introducing an artificial inhomogeneity as an auxiliary function. This function allows us to extend the class of the problems of estimating both statically admissible stress fields and the ultimate-load bounds corresponding to them. In this case, it is necessary to find a relation between the bearing-capacity coefficients for bodies with actual and artificial inhomogeneities. Within the framework of this approach, we consider two identically loaded and supported bodies with different inhomogeneity types $Y(*)$ and $Y'(*)$, $(*) \in \Omega$. Let the quantities u_k, u_k', ε_{kl}, ε_{kl}', σ_{kl}, and σ_{kl}' be the fields of the displacement velocities, strain rates, and stresses, which arise in these bodies under the limiting condition, while α_F and α_F' represent their ultimate-load coefficients. Then, according to the virtual-velocity principle, we have

$$\int_\Omega \sigma_{kl}\varepsilon_{kl}d\Omega = \alpha_F\int_{\Gamma_F} F_k u_k d\Gamma_F, \quad (9)$$

$$\int_\Omega \sigma_{kl}'\varepsilon_{kl}d\Omega = \alpha_F'\int_{\Gamma_F} F_k u_k d\Gamma_F. \quad (10)$$

The ratio of these equalities yields the equation

$$\int_\Omega (\alpha_F'\sigma_{kl} - \alpha_F\sigma_{kl}')\varepsilon_{kl}d\Omega = 0.$$

This equation can be written in the following equivalent form:

$$\int_\Omega (\alpha_F'Y - \alpha_F Y')\frac{\sigma_{kl}\varepsilon_{kl}}{Y}d\Omega + \int_\Omega (Y'\sigma_{kl} - Y\sigma_{kl}')\varepsilon_{kl}\frac{\alpha_F}{Y}d\Omega = 0. \quad (11)$$

Since $f(\sigma_{kl})$ is a convex positive definite function, the following inequality is satisfied:

$$(Y'\sigma_{kl} - Y\sigma_{kl}')\varepsilon_{kl} \geq 0.$$

Therefore, Eq. (11) leads to the inequality

$$\int_\Omega (\alpha_F'Y - \alpha_F Y')\frac{\sigma_{kl}\varepsilon_{kl}}{Y}d\Omega \geq 0,$$

which, in turn, yields

$$\alpha_F \geq \alpha_F'\left(\int_\Omega \sigma_{kl}\varepsilon_{kl}d\Omega\right)\left(\int_\Omega \frac{Y'\sigma_{kl}\varepsilon_{kl}}{Y}d\Omega\right)^{-1}. \quad (12)$$

In particular, if the inequality

$$\frac{\sigma_{kl}\varepsilon_{kl}}{Y} = \text{const} > 0 \quad (13)$$

is satisfied everywhere in the volume Ω, the relation $\alpha_F \geq \frac{\alpha_F'\langle Y\rangle}{\langle Y'\rangle}$ follows from (12), where $\langle Y\rangle = (\text{mes}\,\Omega)^{-1}\int_\Omega Y d\Omega$ is the average yield stress.

Thus, an inhomogeneity distribution $Y(*)$ $[(*) \in \Omega]$, such that inequality (13) is satisfied everywhere in Ω, provides the absolute maximum of the bearing-capacity coefficient among all the inhomogeneity distributions $Y'(*)$ $[(*) \in \Omega]$ satisfying the condition $\langle Y'\rangle \leq \langle Y\rangle$.

REFERENCES

1. Yu. N. Rabotnov, *Mechanics of Deformated Solids* (Nauka, Moscow, 1979).
2. V. V. Sokolovskiĭ, *Theory of Plasticity* (Vysshaya Shkola, Moscow, 1969).
3. M. Zyczkowski, *Combined Loadings in the Theory of Plasticity* (PWW–Pol. Sci. Publ., Warsaw, 1981).
4. W. Olszak, J. Rychlewski, *et al.*, *Plasticity under Non-Homogenous Conditions* (New York, 1962; Mir, Moscow, 1964).

Translated by Yu. Verevochkin

Doklady Physics, Vol. 46, No. 7, 2001, pp. 508–512. Translated from Doklady Akademii Nauk, Vol. 379, No. 2, 2001, pp. 191–195.
Original Russian Text Copyright © 2001 by Akulenko, Kumakshev, Markov.

MECHANICS

Modeling of the Pole's Motion for a Deformable Earth

L. D. Akulenko*, S. A. Kumakshev*, and Yu. G. Markov**

Presented by Academician A.Yu. Ishlinskii February 19, 2001

Received February 20, 2001

Based on canonical variables, action-angles, and Routh equations, and with the help of asymptotic methods of separating motions, we have obtained analytical expressions for the frequencies of the Chandler wobble of the Earth's poles and the diurnal rotation in the model of a deformable Earth. Numerical estimates for the period and the amplitude of the Earth's pole wobble, which correspond to free nutation, are given. The significant effect of gravitational disturbances over a one-year period on the pole trajectory is taken into account. As a result of numerical experiments, we succeeded in the mathematical description of the Chandler component, as well as the annual component, in the accepted Earth's pole coordinates. This description is compared with data of high-precision observations obtained by the International Earth-Rotation Service (IERS). The adequacy of the theoretical model constructed for the observed pole trajectory is established. The possibility of describing the complex oscillatory process of pole motion on the basis of the celestial-mechanics model for the motion of a deformable Earth is proved.

1. Analysis of the Earth's pole trajectory is of scientific and practical importance as one of the significant characteristics of the deformable Earth rotation [1–3]. In this complex oscillatory motion, a principal component is distinguished whose amplitude reaches $a = 0.20''$–$0.25''$. The period of this motion is experimentally estimated to be within the limits of 434 ± 2 sidereal days. The discovery of this component in 1892 was associated with observations performed by S. Chandler, and S. Newk, A. Poincaré, A. Love, F.A. Sludskiĭ, M.S. Molodenskiĭ, *et al.* were among those who took part in the explanation of this phenomenon. The motion indicated is usually called free nutation of a deformable Earth or the Chandler wobble of the pole.

The high-precision data from experimental observations, measurements, and treatment that were carried out in the past 20 years testify to complicated dynamic processes occurring in the Earth–Moon–Sun system, which affect the process of the Earth's rotation. A component with an amplitude of about $0.07''$–$0.08''$ and a one-year period (365 sidereal days) is also recognized in the pole motion. In the authors' opinion, this component is stipulated by the complicated motion of the barycenter of the Earth–Moon system around the Sun. This system, due to the uniqueness of its kinematic and dynamic characteristics in the Solar system, can be considered a binary planet. Perturbing factors of a various physical nature, namely, gravitational and geophysical ones, can appreciably affect the Earth's pole motion.

Existing theoretical models incompletely express the essence of the actual celestial-mechanic process and require frequent corrections in accordance with the observation data. It is an urgent and informative problem of theoretical mechanics and celestial mechanics to develop an adequate mathematical model that would make it possible to describe, on a regular basis and for sufficiently long time intervals, the trajectories of the Earth's rotation axis (i.e., the instantaneous position of the angular-velocity vector) in a certain convenient reference system. Based on the viscoelastic model of a deformable Earth, the modified model must more adequately describe the Chandler wobble. This model must also take into account gravitational-force moments caused by complicated motion of the barycenter owing to the attraction of the Sun and, possibly, planets of the Solar system. In this case, the possibility of taking into account geophysical factors that have, as a rule, an irregular nature and their *a posteriori* estimate based on the statistical treatment of measurement data must not be excluded.

2. In order to refine the inertia tensor for a deformable Earth and to describe the Chandler wobble, the authors accepted a two-layer model of the Earth composed of an absolutely solid core and a viscoelastic mantle [4]. It was assumed that there is an absence of relative displacements on the internal boundary between the core and the mantle, while the outer mantle boundary (i.e., the Earth's surface) is free.

Due to the smallness of strains, we can describe the mantle medium using the linear viscoelasticity theory and consider the deformation process to occur quasi-

* *Institute for Problems in Mechanics, Russian Academy of Sciences, pr. Vernadskogo 101, Moscow, 117526 Russia*

** *Moscow Institute of Aviation (Technical University), Volokolamskoe sh. 4, Moscow, 103767 Russia*

1028-3358/01/4607-0508$21.00 © 2001 MAIK "Nauka/Interperiodica"

statically. These assumptions make it possible to employ rigorous methods of theoretical mechanics together with perturbation-theory methods [5, 6], to estimate elastic strains, and to obtain analytical expressions for the principal central inertia tensor J^* of a deformable Earth in the quasistatic approximation [4]. On the basis of this tensor and with the help of the action-angle variables I_i, w_i ($i = 1, 2, 3$) [7], we derive analytical expressions for the Routh functional R^* of the Earth–Moon system, the period T_1, and the amplitudes $a_{x,y}$ of the Chandler wobble. In particular, we have [5, 8]

$$R^* = \frac{1}{2}\frac{I_2^2}{A^*}\left(1 - \frac{C^* - A^*}{C^*}\frac{\kappa^2}{\chi^2}\right),$$

$$J^* = \mathrm{diag}\{A^*, B^*, C^*\}, \quad A^* < B^* < C^*,$$

$$\chi = \sqrt{\kappa^2 + \lambda^2}, \quad \kappa^2 = \frac{C^*}{A^*}\frac{A^* - B^*}{B^* - C^*}, \quad \lambda^2 = \kappa^2\frac{2EC^* - I_2^2}{I_2^2 - 2EA^*}, \tag{1}$$

$$I_i(t) = I_i^0 = \mathrm{const}, \quad w_3(t) = w_3^0,$$

$$w_{1,2}(t) = n_{1,2}t + w_{1,2}^0.$$

Here, κ^2 and λ^2 are the basic dynamic parameters and E is the integral of the rotational kinetic energy. The angles (phases) w_1 and w_2 correspond to the Chandler wobble and diurnal rotation of a deformable Earth with frequencies n_1 and n_2, respectively:

$$n_1 = -\frac{\pi}{2}I_2\frac{C^* - A^*}{A^*C^*\chi\mathbf{K}(\lambda)}\frac{\kappa}{\sqrt{1+\kappa^2}},$$
$$n_2 = \frac{I_2}{C^*}\left(1 + \frac{C^* - A^*}{A^*\mathbf{K}(\lambda)}\Pi\left(\frac{\pi}{2}, \kappa^2, \lambda\right)\right), \tag{2}$$

where $\mathbf{K}(\lambda)$ and $\Pi\left(\frac{\pi}{2}, \kappa^2, \lambda\right)$ are complete elliptic integrals of the first and the third kind. The parameter λ is rather small, $\lambda^2 \sim 1.36 \times 10^{-14}$, which allows us to significantly simplify the expressions obtained. The calculations lead to a value of the period equal to $T_1 = \frac{2\pi}{n_1} \approx$ 430 sidereal days, which is consistent with the observational data of [3].

The Chandler wobble is defined as the angular displacement of the rotation axis with respect to the attached reference system [3, 8]. The angular-velocity components are expressed in terms of phase w_1 in the form of an expansion with respect to a small parameter $\varepsilon = \frac{\lambda}{\kappa} \sim 10^{-6}$. Restricting ourselves to two expansion terms, we arrive at expressions that have a relative error $O(\varepsilon^4) \sim 10^{-24}$:

$$\omega_1 = \frac{\lambda}{\chi}\frac{I_2}{A^*}\mathrm{cn}(u, \lambda) = \varepsilon\frac{I_2}{A^*}\left(\cos w_1 + \frac{\varepsilon^2}{16}[-(\kappa^2 + 8)\cos w_1 + \kappa^2\cos 3w_1]\right) + O(\varepsilon^5),$$

$$\omega_2 = \frac{\lambda}{\chi}\frac{I_2}{B^*}\mathrm{sn}(u, \lambda) = \varepsilon\sqrt{1+\kappa^2}\frac{I_2}{B^*}$$

$$\times\left(\sin w_1 + \frac{\varepsilon^2}{16}[(\kappa^2 - 8)\sin w_1 + \kappa^2\sin 3w_1]\right) + O(\varepsilon^5), \tag{3}$$

$$\omega_3 = \frac{\kappa}{\chi}\frac{I_2}{C^*}\mathrm{dn}(u, \lambda)$$

$$= \frac{I_2}{C^*} + \frac{\varepsilon^2}{4}\frac{I_2}{C^*}(-2 - \kappa^2 + \kappa^2\cos 2w_1) + O(\varepsilon^4),$$

$$u = \frac{2}{\pi}\mathbf{K}(\lambda)w_1.$$

The angular coordinates (x_c, y_c) of the Chandler component for the pole motion, the corresponding angle α between the figure axis and the rotation axis, and the linear coordinates in the plane tangent to the geoid are, in the first approximation over ε, equal to [8]

$$x_c = \frac{\omega_1}{\omega} \approx a_x\cos w_1, \quad a_x = \varepsilon\frac{C^*}{A^*}, \quad \omega = |\boldsymbol{\omega}|,$$

$$y_c = -\frac{\omega_2}{\omega} \approx -a_y\sin w_1, \quad a_y = \varepsilon\frac{C^*}{B^*}\sqrt{1+\kappa^2},$$
$$\cos\alpha = \frac{\omega_3}{\omega} \approx 1 - \frac{1}{2}(a_x^2\cos^2 w_1 + a_y^2\sin^2 w_1), \tag{4}$$

$$\sqrt{x_p^2 + y_p^2} \approx \varepsilon.$$

More accurate analytical expressions are obtained according to formulas (3). It follows from (4) that the pole trajectory on the geoid surface, which is determined only with allowance for the Chandler component, has an approximately elliptic shape:

$$\frac{X_c^2}{D_{cx}^2} + \frac{Y_c^2}{D_{cy}^2} = 1, \quad D_{cx} = a_xR, \quad D_{cy} = a_yR,$$

$$1 - D_{cx}^2D_{cy}^{-2} \approx \kappa^2 \approx 0.93 \times 10^{-2}, \tag{5}$$

$$D_{cx,y} \approx 7.5 \text{ m}, \quad \varepsilon \approx 1.2 \times 10^{-6},$$

where $R = 6.38 \times 10^6$ m is the Earth's radius. According to relationships (5), the relative difference in the ellipse semiaxes is smaller than 0.5%. The theoretical values turn out somewhat larger than the observed values. The IERS data [3] confirm the validity of conclusions (4) and (5) (see below).

3. The pole trajectory and its fragments obtained in recent years (1980–2000) contain, as basic components, the Chandler wobble (x_c, y_c), annual vibrations (x_h, y_h), and the trend (x_t, y_t) (i.e., the motion of the figure center). The numerical measurement data are given in 0.05-year intervals. This time interval corresponds to the most stable and accurate observations and measurements. The trajectories have the shape of a spiral, close to a circle whose angular dimensions vary from the maximum value of 0.55″ to the minimum value of 0.20″. As a result of treating the data, we find that the amplitudes of about 0.2″ and 0.07″–0.08″ correspond to the Chandler component and the annual component, respectively. In a rough approximation, the representative point participates in two-frequency vibratory motion with frequencies n_{w1} and n_h, whereas the combined motion has a beating nature with a six-year period T_{1h}.

The spectral analysis of the measurement results and the thorough investigation of the trajectories observed make it possible to reveal a more complicated character of the pole motion. In scientific literature, doubts in the possibility of the regular description and prognosis of this chaotic motion are expressed. However, we have another opinion concerning the nature of the pole wobble and assume its description, in terms of theoretical and celestial mechanics, to be adequate [4, 8].

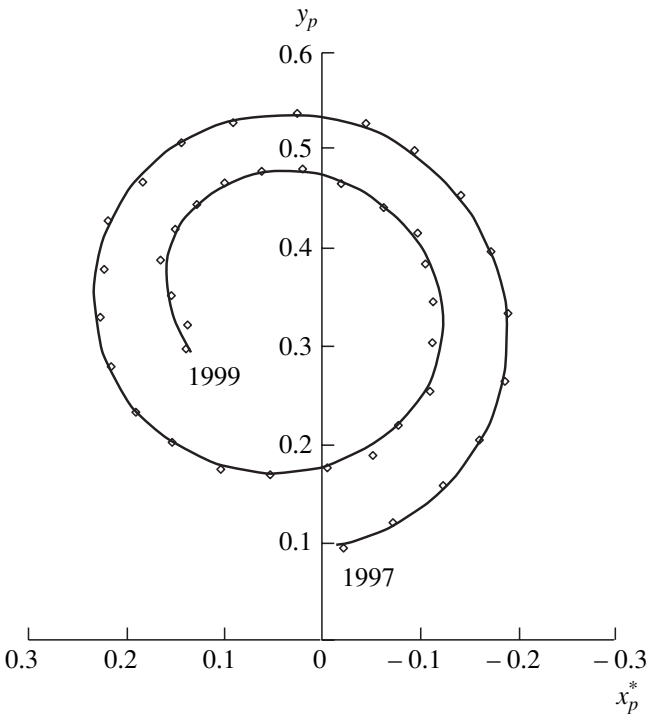

Fig. 1. Theoretical pole trajectory (x_p^*, y_p^*) (solid line) and the IERS measurement data (dots).

The Chandler wobble is considered to be the free nutation (in the theory of solid-body rotation, this phenomenon is called precession) of a deformable Earth. Along with the Chandler wobble, the annual pole motion, in the opinion of specialists, is considered to be basic and stimulated. We assume it possible that the explanation of its origin as caused by the external perturbing moments of gravitational forces, which are stipulated by the complex motion of the barycenter of the Earth–Moon system along a heliocentric orbit, is correct. The annual vibrations exhibit rather regular characteristics, which is difficult to explain through geophysical and other reasons of irregular character. A more thorough study of annual vibrations has allowed us to find their noticeable amplitude modulation with a six-year period.

As was noted above, the resulting pole motion exhibits beats with the period T_{1h}:

$$T_{1h} = \frac{2\pi}{\delta n_{1h}}, \quad \delta n_{1h} = n_h - n_{w1}, \quad \frac{n_{w1}}{n_h} = \nu = 0.84, \quad (6)$$

where T_{1h} is close to a six-year interval. The trajectory's points (x_p, y_p) with the maximum deviation turn out to be very close to the points distant from them by a time period T_{1h}, which is impossible to explain on the basis of seasonal phenomena.

As a result of the observations made in [3], we are able to determine the mean center of the figure. It was also established that during the entire observation period, beginning from the end of the XIX century, the secular shift (drift) along the y_p-axis occurs with an average velocity of approximately 0.005″ per year. This drift has a monotonic character close to linear and has led to the displacement of the center by approximately 15 m towards North America. The drift along the x_p-axis (towards the Greenwich meridian) is insignificant and has no explicitly expressed direction. This phenomenon is a known trend in astrometric literature [3].

For constructing a mathematical model adequate to the astrometric data [3], it is natural to take into account the basic factors indicated above, namely, the center drift $c_x(\theta)$, $c_y(\theta)$, the Chandler wobble with a relative frequency ν (6), and the annual vibration and modulation with a period $T_{1h} = 6$ years. It is convenient to measure the argument θ in years; i.e., $\theta = n_h t$. We restrict ourselves to 8-dimensional approximations over the trigonometric and polynomial system of functions:

$$x_p(\theta) = (\xi, f(\theta)), \quad y_p(\theta) = (\eta, f(\theta)), \tag{7}$$
$$f(\theta) = \left(1, \theta, \cos 2\pi\nu\theta, \sin 2\pi\nu\theta, \sin 2\pi\theta, \cos 2\pi\theta, \cos\frac{\pi}{3}\theta, \sin\frac{\pi}{3}\theta\right)^T,$$
$$\theta = \theta_i, \quad i = 0, 1, 2, \ldots, N = 20\Theta.$$

The unknown eight-dimensional vectors ξ, η, which are assumed to be constant in the given interval $0 \le \theta \le \Theta$, are determined using the least-squares technique on the corresponding set of points [9]. Initially, we test the model through a statistical estimate of the parameters ξ, η of model (7) for a short-term, two-year interval, 1997–1999 (41 points). Rounding off the fourth sign after the point, we obtain the regression curves (7) in which

$$\xi^* = (-0.250, 0.205, 0.030, 0.140, 0.035, 0.079, 0.199, -0.103)^T,$$
$$\eta^* = (0.642, -0.350, -0.159, -0.005, -0.076, -0.053, -0.312, -0.238)^T. \tag{8}$$

The theoretical curve (x_p^*, y_p^*) corresponding to these numerical values and the experimental points of [3] are shown in Fig. 1. There exists a good consistency in the presented data; however, as analysis shows, these curves can be used for prognosis only in the short-term time interval.

We now noticeably increase the set of interpolation points and consider the ten-year interval from 1990 to 2000 (201 points). Similarly to relations (8), with four significant digits after the point, we arrive at

$$\xi^* = (-0.0408, 0.0002, 0.1515, 0.1031, 0.0361, 0.0662, 0.0001, 0.0009)^T,$$
$$\eta^* = (0.3231, 0.0013, -0.1042, 0.1497, -0.0615, 0.0339, 0.0010, -0.0038)^T. \tag{9}$$

Comparing the results of relations (8) and (9), we find that the first curve provides a good local approximation, while the second curve better corresponds to the global pattern of the pole motion [3]. Figures 2 and 3 exhibit the theoretical curve $x^*(\theta)$, $y^*(\theta)$ together with experimental points. The qualitative and quantitative consistency in these data is clearly seen. Assuming a weak correlation and equal accuracy of the measurements, we obtain the mean-square deviations $\sigma_x \approx 0.023''$ and $\sigma_y \approx 0.025''$, which can be considered satisfactory results. The given observational data corresponding to the end of 1999 and the beginning of 2000 have a chaotic character probably caused by gravitational disturbances (parade of planets). Despite this fact, the authors considered it appropriate to present, in Figs. 2 and 3, their prognosis for the pole trajectory in

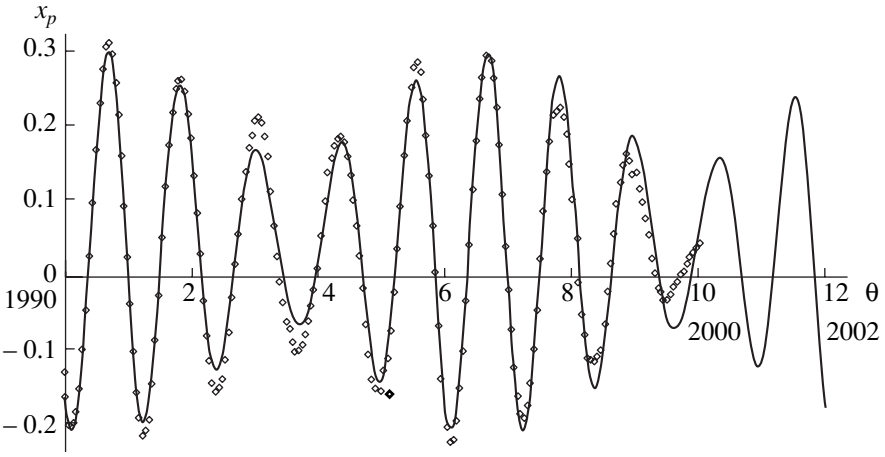

Fig. 2. Theoretical trajectory $x_p^*(\theta)$ of the pole motion to the Greenwich meridian, the prognosis (solid line), and the IERS measurement data (dots).

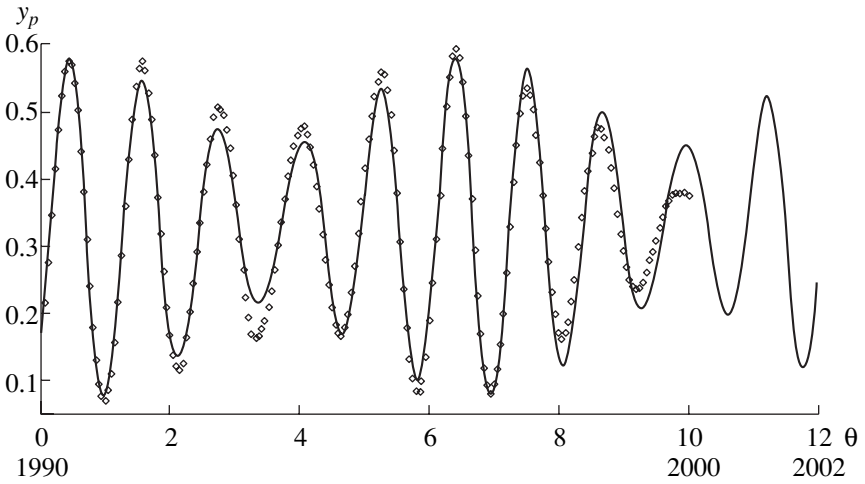

Fig. 3. Theoretical trajectory $y_p^*(\theta)$ of the pole motion to North America, the prognosis (solid line), and the IERS measurement data (dots).

the case of a relatively short-term two-year interval, 2000–2001, for which the IERS observational data are absent in the available literature.

ACKNOWLEDGMENTS

This study was performed under the financial support of the Russian Foundation for Basic Research, projects nos. 99-01-00222, 00-01-00276, 01-02-17250, and 01-01-06306.

REFERENCES

1. H. Moritz and A. Mueller, *Earth Rotation: Theory and Observations* (Ungar, New York, 1987; Naukova Dumka, Kiev, 1992).
2. W. Munk and G. Macdonald, *The Rotation of the Earth* (Cambridge Univ. Press, Cambridge, 1960; Mir, Moscow, 1964).
3. *IERS Annual Reports* (Central Bureau IERS, Observ. Paris, Paris, 1990, July 1991–1999, July 2000).
4. L. I. Konkina, Yu. G. Markov, A. M. Mikisha, and L. V. Rykhlova, Dokl. Akad. Nauk **375**, 619 (2000).
5. F. L. Chernous'ko, Izv. Akad. Nauk SSSR, Mekh. Tverd. Tela, No. 1, 22 (1980).
6. N. N. Bogolyubov and Yu. A. Mitropol'skiĭ, *Asymptotic Methods in the Theory of Nonlinear Oscillations* (Nauka, Moscow, 1974, 4th ed.; Gordon and Breach, New York, 1962).
7. Yu. A. Sadov, Prikl. Mat. Mekh. **34**, 962 (1970).
8. L. D. Akulenko, Yu. G. Markov, and L. V. Rykhlova, Dokl. Akad. Nauk **377**, 618 (2001) [Dokl. Phys. **46**, 261 (2001)].
9. Yu. V. Linnik, *The Method of Least Squares and Principles of the Data-Treatment Theory* (Fizmatgiz, Moscow, 1962; Pergamon, Oxford, 1961).

Translated by G. Merzon

Doklady Physics, Vol. 46, No. 7, 2001, pp. 513–516. Translated from Doklady Akademii Nauk, Vol. 379, No. 2, 2001, pp. 196–199.
Original Russian Text Copyright © 2001 by Ivlev, Maksimova, Nepershin.

MECHANICS

On the Rigid-Die Indentation into a Perfectly Plastic Half-Space with Allowance for Shearing Forces

D. D. Ivlev*, L. A. Maksimova*, and R. I. Nepershin**

Presented by Academician A.Yu. Ishlinskiĭ February 12, 2001

Received February 22, 2001

In this paper, we consider the general plane problem of indenting a rigid die into a perfectly plastic half-space with allowance for shearing forces. The hyperbolic equations of the general plane problem of the perfect-plasticity theory [1] are used under the Tresca–Saint-Venant full-plasticity condition. The condition of full plasticity corresponds to plastic flow due to a shear mechanism. It leads to efficient algorithms for solving boundary value problems, including discontinuities and singularities [2].

1. We assume stresses and spatial coordinates to be dimensionless, taking the tensile–compressive yield stress and the die width as units of the stress and the length, respectively. In the space of the principal stresses, the condition of full plasticity has the form

$$\sigma_1 = \sigma_2, \quad \sigma_3 = \sigma_1 + 1. \tag{1.1}$$

In Cartesian coordinates $\{x, y, z\}$, the stress tensor components satisfying condition (1.1) can be expressed in terms of the average stress σ and the functions θ and φ [1]:

$$\begin{aligned}
\sigma_x &= \sigma - \frac{1}{3} + \frac{1}{2}(1 + \cos\theta)\cos^2\varphi,\\
\sigma_y &= \sigma - \frac{1}{3} + \frac{1}{2}(1 + \cos\theta)\sin^2\varphi,\\
\sigma_z &= \sigma - \frac{1}{3} + \frac{1}{2}(1 - \cos\theta),\\
\sigma &= \frac{1}{3}(\sigma_x + \sigma_y + \sigma_z),
\end{aligned} \tag{1.2}$$

$$\tau_{xy} = \frac{1}{2}(1 + \cos\theta)\sin\varphi\cos\varphi,$$

$$\tau_{xz} = \frac{1}{2}\sin\theta\cos\varphi, \quad \tau_{yz} = \frac{1}{2}\sin\theta\sin\varphi.$$

If the length of a die in the direction of the z-axis considerably exceeds its width along the x-axis, the quantities σ, θ, and φ can be considered independent of the z-coordinate. This is the case of the general plane problem of the perfect-plasticity theory. For it, quasi-linear differential hyperbolic-type equations for the functions σ, θ, and φ, as well as the following three equations for the characteristic curves and differential relations along these functions, were obtained in [1]:

$$\left(\frac{dy}{dx}\right)_{\beta,\alpha} = \tan\left[\varphi \pm \left(\frac{\pi}{4} + \mu\right)\right], \quad \tan 2\mu = \frac{1 - \cos\theta}{2\sqrt{\cos\theta}}, \tag{1.3}$$

$$d\sigma \pm \left[\frac{1 + \cos\theta}{2\sqrt{\cos\theta}}\right]d\varphi = 0 \text{ along } \beta \text{ and } \alpha; \tag{1.4}$$

$$\left(\frac{dy}{dx}\right)_{\gamma} = \tan\varphi, \tag{1.5}$$

$$\left[\frac{2\sin\theta}{1 + \cos\theta}\right]d\sigma + \sin\theta\sin 2\varphi\, d\varphi + d\theta = 0 \text{ along } \gamma. \tag{1.6}$$

At $\theta = 0$, Eqs. (1.3) and (1.4) describe the orthogonal characteristic curves for a plane strain obeying Hencky's relations. At $0 < \theta < \frac{\pi}{2}$, the characteristic curves (1.3) are not orthogonal and the characteristic curve γ described by (1.5) represents the bisector of the angle between the characteristic curves α and β given by (1.3).

2. At the free half-space boundary AC near the die (Fig. 1), the normal stresses, which satisfy the condition of full plasticity (1.1), are $\sigma_x = \sigma_z = -1$ and $\sigma_y = 0$.

* *Yakovlev Chuvash State Pedagogical University, ul. Karla Marksa 38, Cheboksary, 428000 Russia*

** *Moscow State Academy of Instrumentation Engineering and Informatics, ul. Stromynka 20, Moscow, 107846 Russia*

1028-3358/01/4607-0513$21.00 © 2001 MAIK "Nauka/Interperiodica"

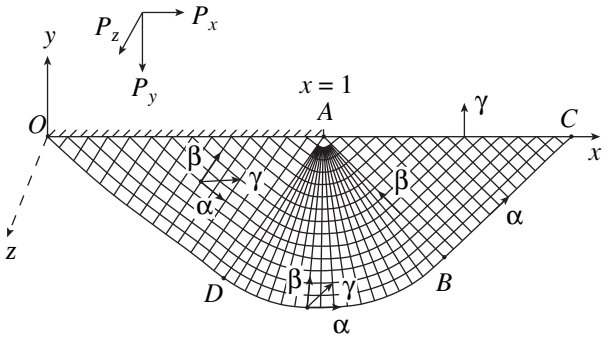

Fig. 1.

Therefore, Eqs. (1.2) yield the following values of the functions σ, φ, and θ on *AC*:

$$\sigma = -\frac{2}{3}, \quad \varphi = \frac{\pi}{2}, \quad \theta = 0 \text{ on } AC. \tag{2.1}$$

At θ = 0, characteristic curves (1.3) are straight lines, i.e., $\left(\frac{dy}{dx}\right)_{\alpha,\beta} = \pm 1$, and there exists a uniform stressed state (2.1) of plane strain in the region *ABC*. Characteristic curves (1.3) are defined only for positive values of cosθ. Therefore, the angle θ on the die boundary *OA* is given as a parameter of the problem in the interval

$$0 \le \theta < \frac{\pi}{2} \text{ on } OA. \tag{2.2}$$

We define the second parameter, the angle φ related to contact tangential stresses by equations (1.2), in the following interval dependent on the angle θ:

$$c\mu \le \varphi < \frac{\pi}{4} + \mu \text{ on } OA, \tag{2.3}$$

$$0 \le c \le 1, \quad \mu = \frac{1}{2}\arctan\left[\frac{1-\cos\theta}{2\sqrt{\cos\theta}}\right]. \tag{2.4}$$

The upper limit in (2.3) is associated with the degeneration of the characteristic-curve field into a line tangential to the die boundary. The lower limit corresponds to the degeneration of the characteristic-curve field, which occurs at large angles θ, when the angle between the directions of the characteristic curves α and β approaches π.

At the singular point *A*, the average stress variation, due to transition from the free boundary *AC* to the die boundary *OA*, is calculated by integrating Eq. (1.4) along the degenerate characteristic curve α:

$$\sigma = -\frac{2}{3} + \int_{\pi/2}^{\varphi}\left[\frac{1+\cos\theta}{2\sqrt{\cos\theta}}\right]d\varphi. \tag{2.5}$$

A similar integral calculated along the degenerate characteristic curve β is used to control the bearing capacity of the rigid wedge, whose vertex is at the point *O*.

3. If the strain is plane, then θ ≡ 0. Orthogonal characteristic curves (1.3) form a centered fan with straight β-lines in the region *ABD*, while integral (2.5) determines the value of σ in the region *OAD* of the uniform stressed state. Both the pressure applied to the die and the contact tangential stresses, equal to shearing forces, are determined from (1.2):

$$P_y = -\sigma_y = 1 + \frac{\pi}{2} - (\varphi + \sin^2\varphi), \tag{3.1}$$

$$P_z = \tau_{yz} = 0, \quad P_x = \tau_{xy} = \frac{1}{2}\sin 2\varphi. \tag{3.2}$$

On the boundary of the half-space, the length *L* of the characteristic curve *AB* and the coordinate x_C of the point *C* are given by

$$L = \sin\left(\frac{\pi}{4} - \varphi\right), \quad x_C = 1 + \sqrt{2}\sin\left(\frac{\pi}{4} - \varphi\right), \tag{3.3}$$

where φ varies in interval (2.3) with μ = 0.

The case φ = 0 corresponds to the pressure applied to the smooth Prandtl die:

$$P_y = 1 + \frac{\pi}{2}, \quad P_x = P_z = 0, \text{ and } x_C = 2. \tag{3.4}$$

In this case, the wedge, with its vertex at the point *O*, is loaded to the plastic state and the field of the characteristic curves is symmetric with respect to the die middle.

If $\varphi = \frac{\pi}{4}$, relations (3.2)–(3.4) yield

$$P_y = \frac{1}{2}\left(1 + \frac{\pi}{2}\right), \quad P_x = \frac{1}{2}, \quad P_z = 0, \quad L = 0, \quad x_C = 1. \tag{3.5}$$

Then, the field of the characteristic curves degenerates into a line of shear which coincides with the die boundary. In addition, the contact tangential stress in the direction of the *x*-axis is equal to the shear yield point and the pressure applied to the die is twice as low as that in the case of the Prandtl die.

4. For θ > 0, the fields of the characteristic curves and the stresses are calculated by numerically integrating Eqs. (1.3)–(1.6) with boundary conditions (2.1)–(2.5).

At the regular nodes which are formed by the mesh of the characteristic curves and do not belong to both the singular point *A* and the die boundary *OA*, we solve the elementary Cauchy problem for the functions σ, φ, and θ given at the points *1* and *2* of the Cauchy contour (Fig. 2). The functions φ and θ are approximated by their average values calculated along the characteristic curves, and finite differences are substituted for the differentials entering into Eqs. (1.3)–(1.6). The coordinates *x*, *y* of the point *P* must satisfy three differential

equations for the characteristic curves, which, in the case of the finite-difference approximation, have the form

$$\frac{y-y_1}{x-x_1} = \tan\left[\varphi - \left(\frac{\pi}{4}+\mu\right)\right] \text{ along } \alpha, \quad (4.1)$$

$$\frac{y-y_2}{x-x_2} = \tan\left[\varphi + \left(\frac{\pi}{4}+\mu\right)\right] \text{ along } \beta, \quad (4.2)$$

$$\frac{y-y_3}{x-x_3} = \tan\varphi \text{ along } \gamma. \quad (4.3)$$

The unknown coordinates of point *3* are determined by the point of the intersection of the characteristic curve γ with the Cauchy contour, which is approximated by the chord that connects points *1* and *2*:

$$\frac{y_3-y_1}{x_3-x_1} = \frac{y_2-y_1}{x_2-x_1}. \quad (4.4)$$

After determining the coordinates of point *3*, the functions σ, φ, and θ at it are calculated by linear interpolation between the points *1* and *2* at which these functions are given

$$\sigma_3 = \sigma_1 + a(\sigma_2-\sigma_1), \quad \varphi_3 = \varphi_1 + a(\varphi_2-\varphi_1), \quad \theta_3 = \theta_1 + a(\theta_2-\theta_1). \quad (4.5)$$

Here, $a = \dfrac{S_{13}}{S_{12}}$ and S_{13} and S_{12} are the distances between points *1–3* and *1–2*, respectively.

As a result, the differential relations along the three characteristic curves take the form

$$\sigma - \sigma_1 = \left[\frac{1+\cos\theta}{2\sqrt{\cos\theta}}\right](\varphi-\varphi_1) \text{ along } \alpha, \quad (4.6)$$

$$\sigma - \sigma_2 = -\left[\frac{1+\cos\theta}{2\sqrt{\cos\theta}}\right](\varphi-\varphi_1) \text{ along } \beta, \quad (4.7)$$

$$\theta_3 - \theta = \left[\frac{2\sin\theta}{1+\cos\theta}\right](\sigma-\sigma_3) + \sin\theta\sin 2\varphi(\varphi-\varphi_3) \text{ along } \gamma, \quad (4.8)$$

where σ_1, σ_2, and σ_3 represent values of σ at points *1*, *2*, and *3*.

Equations (4.1)–(4.8) contain the unknown coordinates *x*, *y* and the functions σ, φ, and θ at point *P*, as well as the unknown coordinates x_3, y_3 of point *3*. For solving these equations, the following iteration procedure is used:

Initial values of the angles $\varphi = \varphi_1$ and $\theta = \theta_1$, $\varphi = \varphi_2$ and $\theta = \theta_2$, and $\varphi = \frac{1}{2}(\varphi_1+\varphi_2)$ and $\theta = \frac{1}{2}(\theta_1+\theta_2)$ are given along the α-, β-, and γ-characteristic curves connecting points *1*, *2*, and *3* to point *P*, respectively.

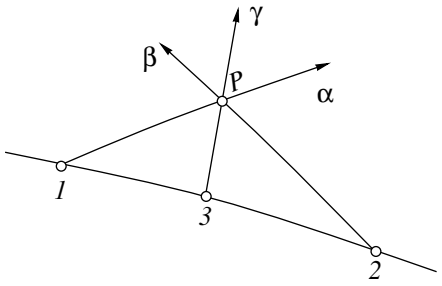

Fig. 2.

(1) The coordinates *x*, *y* and the functions σ, φ at point *P* are calculated using Eqs. (4.1), (4.2) and (4.6), (4.7), respectively.

(2) Equations (4.3), (4.4) and linear interpolation (4.5) are used to determine the coordinates x_3, y_3 of point *3* and the values σ_3, φ_3, θ_3 at this point, respectively.

(3) The angle θ at point *P* is calculated using Eq. (4.8).

(4) Finally, we evaluate the average values φ and θ between points *1 – P*, *2 – P*, and *3 – P* and pass to the next step.

The absolute differences of successive values of φ and θ calculated at point *P* approach values of the order of 10^{-5} after two or three iterations, which can be performed almost instantly using a Pentium-133 PC.

In the region *ABD* (Fig. 1), the field of the characteristic curves is determined by solving the Goursat problem with the functions σ, φ, and θ assumed to be known both along the β-type characteristic curve *AB* and at the singular point *A*. Simultaneously, regular nodes of the mesh of the characteristic curves are calculated using Eqs. (4.1)–(4.8). Then, in the region *OAD*, we solve the mixed problem, with the functions σ, φ, and θ given along the β-type characteristic curve *AD* and the boundary conditions given on *OA*. Since φ and θ are known on the boundary *OA*, the coordinates *x* and the values of σ at the nodes situated there are calculated using linear equations (4.1) and (4.6).

In the region *OABD*, the field of the characteristic curves is determined accurate to an unknown length *L* of the characteristic curve *AB*. This length is calculated from the condition that the coordinate x_0 of the point *O* is equal to zero. The algorithm of constructing the field of the characteristic curves determines x_0 as a continuous function of the parameters *L*, which must satisfy the condition

$$x_0(L) = 0. \quad (4.9)$$

Equation (4.9) is solved using Newton's iteration method:

$$L_{i+1} = L_i - \frac{x_0(L_i)\Delta L}{x_0(L_i+\Delta L) - x_0(L_i)}, \quad \Delta L = 10^{-3}, \quad (4.10)$$

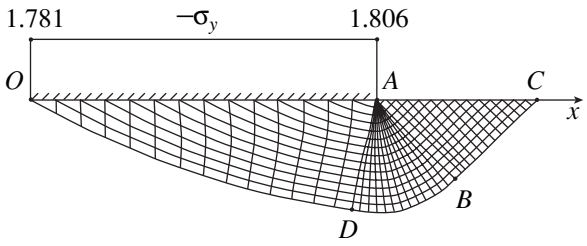

Fig. 3.

where $i = 0, 1, 2, \ldots$ is the iteration number. In (4.10), the derivative is approximated by the finite-difference ratio, and the length L corresponding to the plane strain calculated using (3.3) is taken as an initial approximation.

Iterations (4.10) lead to the value $|x_0| < 10^{-6}$ after two or three steps. For a pair of values φ and θ given on the boundary OA, solving one version of the problem takes about 1 s using a Pentium-133. This fact suggests that the numerical algorithms for solving hyperbolic problems of the perfect-plasticity theory [2] are very efficient.

When the modulus of the contact tangential stress $P_{xz} = \sqrt{P_x^2 + P_z^2}$ approaches its limiting value $\frac{1}{2}$, the field of the characteristic curves degenerates into a line coinciding with the die boundary. The case $\varphi = \frac{\pi}{2}$ and $\theta \longrightarrow \frac{\pi}{2}$ corresponds to the shearing of the longitudinal die along the z-axis, where $P_x = 0$ and $P_z = \frac{1}{2}$. Then, according to Eqs. (2.5) and (1.2), $\sigma = -\frac{2}{3}$ and $\sigma_z = -\frac{1}{2}$. This is the case of pure shear under the minimum pressure applied to the die, with

$$P_y = \frac{1}{2}, \quad P_x = 0, \quad \text{and} \quad P_z = \frac{1}{2} \quad \text{at} \quad \varphi = \theta = \frac{\pi}{2}. \quad (4.11)$$

Thus, when varying shearing forces, the limiting pressure applied to the die changes from its maximum value $1 + \frac{\pi}{2}$, which corresponds to the smooth Prandtl die, to the minimum value $\frac{1}{2}$, which corresponds to purely longitudinal shear of an absolutely rough die.

Figure 3 shows an example of the field of the characteristic curves under increasing contact tangential stresses corresponding to $\theta = 1.25$ and $\varphi = 0.588$ and of the distribution of the normal stress σ_y over the contact surface of the die. The calculations show that, being almost constant, the normal pressure applied to the die slightly increases near the salient point A. Sufficiently far from the singular point A, the α- and β-type characteristic curves are almost orthogonal, because, according to the boundary conditions $\theta \longrightarrow 0$ given on AB. At the same time, these curves become nonorthogonal while approaching the die boundary, because θ increases, tending to its value given on OA.

The developed numerical method of integrating the hyperbolic equations of the general plane problem of the perfect-plasticity theory can be used in engineering problems involved in plasticity theory in the cases of variable contact tangential stresses, curvilinear boundaries of the dies used, and deformable blanks of finite thicknesses [3].

REFERENCES

1. D. D. Ivlev and L. A. Maksimova, Dokl. Akad. Nauk **373**, 39 (2000) [Dokl. Phys. **45**, 330 (2000)].
2. D. D. Ivlev and A. Yu. Ishlinskiĭ, Dokl. Akad. Nauk **368**, 333 (1999) [Dokl. Phys. **44**, 642 (1999)].
3. B. A. Druyanov and R. I. Nepershin, *Theory of Technological Plasticity* (Mashinostroenie, Moscow, 1990).

Translated by Yu. Verevochkin

Doklady Physics, Vol. 46, No. 7, 2001, pp. 517–521. Translated from Doklady Akademii Nauk, Vol. 379, No. 2, 2001, pp. 200–204.
Original Russian Text Copyright © 2001 by Edel'man.

MECHANICS

Waves on Boundaries of Porous Media

I. Ya. Edel'man

Presented by Academician V.N. Strakhov March 5, 2001

Received March 6, 2001

INTRODUCTION

The object of this study is to investigate the existence of surface waves propagating along the interface between an elastically deformable saturated porous medium and either vacuum or a compressible fluid and along the interface between two different porous media. In 1885, Lord Rayleigh [1] theoretically proved that waves can propagate along the plane free boundary of an isotropic elastic half-space, with their amplitude decreasing rapidly with the depth. Because the surface waves can propagate along a boundary without damping or with much less damping than that for bulk waves, such waves attract significant interest in geophysical, geological, and acoustic problems and in oceanology and various engineering applications. A. Love [2] found that the propagation of the Rayleigh surface waves depends on the characteristics of the media. Consequently, the study of surface waves propagating in media with different structures can provide important information on their properties. The surface waves on the boundaries of solids have been studied fairly well [3]. The properties of surface waves on the boundaries of saturated porous media are significantly affected by the presence of a longitudinal wave of the second kind. In this paper, we proved that there exist two or three types of surface waves, respectively, on the free boundary of a saturated porous medium or on the interface between a saturated porous medium and a fluid, and there exist three or four different modes on the interface between two porous media, depending on medium parameters.

Let the two half-spaces Ω^{I} and Ω^{II} have a common boundary Γ and a porous medium occupy the region Ω^{I}. In dimensionless variables, the set of equations describing the porous medium take the following form ($x \in R^3$, $t \in [0, T]$) [4].

Mass conservation laws,

$$\frac{\partial \rho_{\mathrm{f}}}{\partial t} + \mathrm{div}(\rho_{\mathrm{f}}\mathbf{v}_{\mathrm{f}}) = 0, \quad \frac{\partial \rho_{\mathrm{s}}}{\partial t} + \mathrm{div}(\rho_{\mathrm{s}}\mathbf{v}_{\mathrm{s}}) = 0. \quad (1)$$

Here, ρ is the density, $\mathbf{v}$ is the velocity vector, and the subscripts "f" and "s" correspond to the fluid and solid phases, respectively.

Momentum conservation laws,

$$\rho_{\mathrm{f}}\left[\frac{\partial}{\partial t} + \left(v_{\mathrm{f}j}, \frac{\partial}{\partial x_j}\right)\right]v_{\mathrm{f}i} - \frac{\partial T^{\mathrm{f}}_{ij}}{\partial x_j} + \pi(v_{\mathrm{f}i} - v_{\mathrm{s}i}) = 0,$$
$$\rho_{\mathrm{s}}\left[\frac{\partial}{\partial t} + \left(v_{\mathrm{s}j}, \frac{\partial}{\partial x_j}\right)\right]v_{\mathrm{s}i} - \frac{\partial T^{\mathrm{s}}_{ij}}{\partial x_j} - \pi(v_{\mathrm{f}i} - v_{\mathrm{s}i}) = 0. \quad (2)$$

Here, T^{f}_{ij} and T^{s}_{ij} are the stress tensors and π is a positive constant. The stress tensor for the fluid phase has the following linear form:

$$T^{\mathrm{f}}_{ij} = -p_{\mathrm{f}}\delta_{ij} - \beta\Delta_m\delta_{ij}, \quad p_{\mathrm{f}} = p_{\mathrm{f}_0} + \kappa(\rho_{\mathrm{f}} - \rho_{\mathrm{f}_0}), \quad (3)$$

where, p_{f} is the pore pressure; $p_{\mathrm{f}0}$ and $\rho_{\mathrm{f}0}$ are the initial values of the pore pressure and fluid density, respectively; κ is the constant compressibility coefficient for the fluid, which depends only on the equilibrium value m_{E} of the porosity; $\Delta_m = m - m_{\mathrm{E}}$ is the variation of the porosity; and β is the interaction coefficient for the phases. The stress tensor for the skeleton can be written in the form

$$T^{\mathrm{s}}_{ij} = \lambda e_{kk}\delta_{ij} + 2\mu e_{ij} + \beta\Delta_m\delta_{ij}. \quad (4)$$

Here, λ and μ are the Lamé coefficients dependent only on m_{E} and e_{ij} is the strain tensor

$$e_{ij} = \frac{1}{2}\left(\frac{\partial u_{\mathrm{s}i}}{\partial x_j} + \frac{\partial u_{\mathrm{s}j}}{\partial x_i}\right), \quad (5)$$

where $\mathbf{u}_{\mathrm{s}}$ is the displacement vector for the solid phase, with $\mathbf{v}_{\mathrm{s}} = \dfrac{\partial \mathbf{u}_{\mathrm{s}}}{\partial t}$.

Porosity balance equation,

$$\frac{\partial \Delta_m}{\partial t} + \left(v_{\mathrm{s}i}, \frac{\partial}{\partial x_i}\right)\Delta_m + m_{\mathrm{E}}\mathrm{div}(\mathbf{v}_{\mathrm{f}} - \mathbf{v}_{\mathrm{s}}) = -\frac{\Delta_m}{\tau}, \quad (6)$$

where τ is the porosity relaxation time.

Shmidt Joint Institute of Physics of the Earth,
Russian Academy of Sciences,
Bol'shaya Gruzinskaya ul. 10, Moscow, 123810 Russia

1028-3358/01/4607-0517$21.00 © 2001 MAIK "Nauka/Interperiodica"

In the general case when the half-space Ω^{II} is also filled with a saturated porous medium, the following boundary conditions must be fulfilled on the surface Γ:

(1) the continuity of the summary stresses,

$$(T_{ij}^{s} + T_{ij}^{f})n_j\big|^{I} = (T_{ij}^{s} + T_{ij}^{f})n_j\big|^{II}, \quad (7)$$

where $\mathbf{n}$ is the vector normal to the interface;

(2) the continuity of the displacements for the solid phases,

$$\mathbf{u}_s\big|^{I} = \mathbf{u}_s\big|^{II}; \quad (8)$$

(3) the continuity of the mass flux through the boundary,

$$\rho_f(\mathbf{v}_f - \mathbf{v}_s)\mathbf{n}\big|^{I} = \rho_f(\mathbf{v}_f - \mathbf{v}_s)\mathbf{n}\big|^{II}; \quad (9)$$

(4) and the proportionality of the pore pressure jump to the mass flux through the boundary [5],

$$\rho_f(\mathbf{v}_f - \mathbf{v}_s)\mathbf{n}\big|^{I} = \alpha\left(p_f\big|^{I} - \frac{m^{I}}{m^{II}}p_f\big|^{II}\right). \quad (10)$$

The experimental constant α can be considered a surface characteristic similar to porosity. The case $\alpha = 0$ corresponds to completely "closed" surface pores (impenetrable interface), while the case $\alpha = \infty$ corresponds to a completely penetrable interface.

We consider the linearization of set (1)–(6) in the neighborhood of the equilibrium state with the following constant values of the parameters:

$$\rho_f = \rho_{f0}, \quad \rho_s = \rho_{s0}, \quad \mathbf{v}_f = 0, \quad \mathbf{v}_s = 0, \quad \Delta_m = 0.$$

After introducing the displacement vector $\mathbf{u}_f$ for the fluid phase and performing the linearization, the set of equations (1)–(6) takes the form

$$\frac{\partial \rho_f}{\partial t} + \rho_{f0}\frac{\partial^2 u_{fi}}{\partial x_i \partial t} = 0, \quad \frac{\partial \rho_s}{\partial t} + \rho_{s0}\frac{\partial^2 u_{si}}{\partial x_i \partial t} = 0, \quad (11)$$

$$\rho_{f0}\frac{\partial^2 u_{fi}}{\partial t^2} + \frac{\partial(p_f\delta_{ij})}{\partial x_j} + \frac{\partial(\beta\Delta_m\delta_{ij})}{\partial x_j} + \pi\frac{\partial(u_{fi} - u_{si})}{\partial t} = 0, \quad (12)$$

$$\rho_{s0}\frac{\partial^2 u_{si}}{\partial t^2} - \mu\Delta u_{si} - (\lambda + \mu)\nabla \mathrm{div} u_s - \frac{\partial(\beta\Delta_m\delta_{ij})}{\partial x_j} - \pi\frac{\partial(u_{fi} - u_{si})}{\partial t} = 0, \quad (13)$$

$$\frac{\partial \Delta_m}{\partial t} + m_E \mathrm{div}\frac{\partial(\mathbf{u}_f - \mathbf{u}_s)}{\partial t} = -\frac{\Delta_m}{\tau}, \quad (14)$$

where the unknown variables are ρ_f, ρ_s, $\mathbf{u}_f$, $\mathbf{u}_s$, and Δ_m.

SURFACE WAVES ON THE INTERFACE BETWEEN A POROUS MEDIUM AND VACUUM

The general problem on the propagation of elastic waves in a bounded space is rather complicated. We restrict ourselves to the solution of a particular plane problem (in the xy plane, $i, j = 1, 2$) and consider the propagation of elastic waves in a porous medium occupying the half-space $y > 0$ bounded by the half-space $y < 0$ with a vacuum (or fluid, or other porous medium). On the free boundary $y = 0$ of the porous medium, both the summary stresses and the relative velocity vanish:

$$\mu\left(\frac{\partial u_{s1}}{\partial y} + \frac{\partial u_{s2}}{\partial x}\right)\Big|_{y=0} = 0,$$

$$\left(\lambda \mathrm{div}\mathbf{u}_s + 2\mu\frac{\partial u_{s2}}{\partial y} - \kappa(\rho_f - \rho_{f0})\right)\Big|_{y=0} = 0, \quad (15)$$

$$\frac{\partial(u_{f2} - u_{s2})}{\partial t}\Big|_{y=0} = 0.$$

Our purpose is to prove that boundary value problem (11)–(15) has solutions that represent surface waves, i.e., solutions decreasing as $|y| \longrightarrow \infty$. To do this, we consider the propagation of a harmonic wave with the frequency ω, wave number k, and amplitude dependent on y. It should be noted that we consider solutions to problem (1)–(10) in the absence of external forces. Consequently, such solutions are unambiguously defined by the Cauchy boundary conditions. In this case, it is natural to determine the wave frequency ω as a function of a real number $k \in R^1$. Therefore, $\frac{\mathrm{Re}\,\omega}{k}$ and $\mathrm{Im}\,\omega$ define the phase velocity and wave damping, respectively.

We seek the solution to problem (11)–(15) in the form

$$\begin{aligned}
\mathbf{u}_f &= \nabla\varphi_f + ((\psi_f)_y, -(\psi_f)_x),\\
\mathbf{u}_s &= \nabla\varphi_s + ((\psi_s)_y, -(\psi_s)_x),\\
\varphi_f &= A_f(y)\exp(i(kx - \omega t)),\\
\varphi_s &= A_s(y)\exp(i(kx - \omega t)),\\
\psi_f &= B_f(y)\exp(i(kx - \omega t)),\\
\psi_s &= B_s(y)\exp(i(kx - \omega t)),\\
\rho_f - \rho_{f0} &= A_{\rho,f}(y)\exp(i(kx - \omega t)),\\
\rho_s - \rho_{s0} &= A_{\rho,s}(y)\exp(i(kx - \omega t)),\\
\Delta_m &= A_{\Delta_m}(y)\exp(i(kx - \omega t)).
\end{aligned} \quad (16)$$

It is possible to prove [6–8] that the unknown amplitudes $A_{\rho,f}(y)$, $A_{\rho,s}(y)$, $A_{\Delta_m}(y)$, and $B_f(y)$ are related by

algebraic expressions with the amplitudes $A_f(y)$, $A_s(y)$, and $B_s(y)$ for which the following solution is valid:

$$\begin{pmatrix} A_f \\ A_s \end{pmatrix} = C_1(0)\begin{pmatrix} R_{f1} \\ R_{s1} \end{pmatrix}\exp(-\gamma_1 y) + C_2(0)\begin{pmatrix} R_{f2} \\ R_{s2} \end{pmatrix}\exp(-\gamma_2 y), \quad (17)$$

$$B_s = C_s(0)\exp(-\mu_s y).$$

Here, in the case where $|k| \gg 1$ and $\beta = 0$, we have

$$\gamma_j = \tilde{\gamma}_j|k|, \quad \tilde{\gamma}_1 = \sqrt{1-\frac{\tilde{\omega}^2}{\kappa}},$$

$$\tilde{\gamma}_2 = \sqrt{1-\frac{\tilde{\omega}^2}{a_{s1}^2}}, \quad \tilde{\omega} = \frac{\omega}{k}, \quad (18)$$

$$\tilde{\mu}_s = \frac{\mu_s}{|k|} = \sqrt{1-\frac{\tilde{\omega}^2}{a_{s2}^2}},$$

$$(R_{f1}, R_{s1}) = (1, 0), \quad (R_{f2}, R_{s2}) = (0, 1),$$

where a_{s2} and a_{s1} are the velocities of transverse and longitudinal waves in the infinite elastic medium, respectively, and $\sqrt{\kappa}$ is the sound velocity in the fluid.

It is evident that the radicals $\tilde{\gamma}_1$, $\tilde{\gamma}_2$, and $\tilde{\mu}_s$ are multiple-valued functions of $\tilde{\omega}$. In order for these functions to be unambiguous, we will consider the Riemann surface with cuts from the points $\pm\sqrt{\kappa}$, $\pm a_{s2}$, and $\pm a_{s1}$. In this case, the signs of the radicals can be defined unambiguously (depending on the sheet of the Riemann surface [7]) so that the radiation condition [3], i.e., the boundedness condition for the solution, is fulfilled along the real axis.

Substituting solution (17) into boundary conditions (15), we obtain the set of equations for the unknowns $C_1(0)$, $C_2(0)$, and $C_s(0)$. The degeneracy condition for the determinant of this set leads to the dispersion equation for the surface-wave velocity:

$$\mathcal{P}_v(\tilde{\omega}) = \tilde{\gamma}_1\mathcal{P}_R(\tilde{\omega}) + \tilde{\gamma}_2\frac{\rho_{f0}}{\rho_{s0}}\frac{\tilde{\omega}^4}{a_{s2}^4} = 0. \quad (19)$$

Here, $\mathcal{P}_R$ corresponds to the Rayleigh classical equation [3]

$$\mathcal{P}_R(\tilde{\omega}) = \left(2-\frac{\tilde{\omega}^2}{a_{s2}^2}\right)^2 - 4\tilde{\gamma}_2\tilde{\mu}_s. \quad (20)$$

It is of interest to note that Eq. (19) exactly coincides with the dispersion equation for the surface waves on the interface between fluid and solid half-spaces [3] and, consequently, has two roots. The asymptotic expansion for the first root $\tilde{\omega}_1$ takes the form

$$\tilde{\omega}_1 = \sqrt{\kappa}(1 - c_1\kappa^2 + O(\kappa^3)), \quad c_1 = \frac{\rho_{f0}^2}{8\mu^2\left(1-\frac{a_{s2}^2}{a_{s1}^2}\right)^2}. \quad (21)$$

It is evident that $\mathrm{Re}\,\tilde{\omega}_1 \in [0, \sqrt{\kappa})$. This phase velocity corresponds to a very slow surface wave (the Stoneley wave) propagating virtually without damping. Its velocity is of the order of $O(\sqrt{\kappa})$ and lower than the velocities of all the bulk waves in the porous medium.

Dispersion equation (19) also has a complex-valued root $\tilde{\omega}_{R'}$ such that $\mathrm{Re}\,\tilde{\omega}_{R'} \in (\sqrt{\kappa}, a_{s2})$. This root corresponds to the Rayleigh generalized wave whose phase velocity $c_{R'} \longrightarrow c_R$ for $\rho_{f0} \longrightarrow 0$, where c_R is the velocity of the Rayleigh classical wave in an elastic half-space. The asymptotic expansion of this root yields

$$\tilde{\omega}_{R'} = \Omega_0 + \sqrt{\kappa}\Omega_1 + O(\kappa), \quad (22)$$

where $\Omega_0 = c_R$ and Ω_1 are determined from the equation

$$\left[\frac{4}{a_{s2}^4}\Omega_0^3 - 8\frac{1}{a_{s2}^2}\Omega_0 - 4\frac{d}{d\tilde{\omega}}\left(\sqrt{1-\frac{\tilde{\omega}^2}{a_{s2}^2}}\sqrt{1-\frac{\tilde{\omega}^2}{a_{s1}^2}}\right)\Bigg|_{\tilde{\omega}=\Omega_0}\right]\Omega_1 = i\frac{\rho_{f0}}{\rho_{s0}}\frac{\Omega_0^3}{a_{s2}^4}\sqrt{1-\frac{\Omega_0^2}{a_{s1}^2}}. \quad (23)$$

The real part of expansion (22) defines the phase velocity of the Rayleigh generalized wave, whereas $\mathrm{Im}\,\Omega_1$ gives the wave damping. The damping implies that the reemission of wave energy occurs deep in the medium. This is a so-called "leaky" surface wave. Because $\mathrm{Im}\,\Omega_1 > 0$, it can be proved by estimating the surface-wave amplitudes that the energy of this wave is partially converted into the energy of a slow longitudinal wave of the second kind. However, contrary to the case of the Rayleigh generalized wave on the interface between fluid and solid half-spaces, when the energy is reemitted from a solid to a fluid, the leaky wave on the free boundary of a porous medium emits energy into the half-space that contains the wave.

SURFACE WAVES ON THE INTERFACE BETWEEN A POROUS MEDIUM AND A FLUID

Let the region Ω^{II} be filled with a compressible fluid, for which the following laws of conservation of mass

and momentum are valid (the superscript—stands for the region Ω^{II}):

$$\frac{\partial \bar{\rho}_f}{\partial t} + \mathrm{div}(\bar{\rho}_f \bar{\mathbf{v}}_f) = 0,$$
$$\bar{\rho}_f\left[\frac{\partial}{\partial t} + \left(\bar{v}_{fj}, \frac{\partial}{\partial x_j}\right)\right]\bar{v}_{fi} - \frac{\partial \bar{T}_{ij}}{\partial x_j} = 0. \quad (24)$$

Here, $\bar{T}_{ij}$ is the stress tensor

$$\bar{T}_{ij} = -\bar{p}_f \delta_{ij}, \quad \bar{p}_f = \bar{p}_{f0} + \bar{\kappa}(\bar{\rho}_f - \bar{\rho}_{f0}). \quad (25)$$

The fluid is assumed compressible, its compressibility coefficient $\bar{\kappa}$ is constant, and $\bar{p}_{f0}$ and $\bar{\rho}_{f0}$ are initial values of the pressure and density of the fluid.

We consider the two-dimensional problem on the propagation of surface waves along the interface $y = 0$, which separates a porous medium (the half-space $y > 0$) and a fluid (the half-space $y < 0$). On the interface $y = 0$, the following boundary conditions, which are consequences of general boundary conditions (7)–(10), must be fulfilled: (a) the continuity of the total stresses, (b) the continuity of the mass flux, (c) the proportionality of the pore pressure jump to the mass flux. As above, we study the propagation of a harmonic wave with the frequency ω, wave number k, and amplitude dependent on y. In the region Ω^I, bounded solution (17) remains valid. In the region Ω^{II} ($y < 0$), the solution is found in a similar way [7]. The dispersion equation with $\beta = 0$ and $|k| \gg 1$ takes the form

$$\left(-\frac{\mu}{\bar{\gamma}_1\bar{\gamma}_2}\mathcal{P}_\nu + \bar{\rho}_{f0}\frac{\tilde{\omega}^4}{\bar{\gamma}_1 a_{s2}^2}\right)\left(\bar{\gamma}_1 - i\alpha\tilde{\omega}\left(\frac{\bar{\gamma}_1}{\bar{\gamma}_1} + m_E\right)\right)$$
$$-\bar{\rho}_{f0}\left(1 + \frac{\bar{\gamma}_1}{\bar{\gamma}_1}\right)\frac{\tilde{\omega}^4}{a_{s2}^2}\left(1 - \frac{i}{\bar{\gamma}_1}\alpha\tilde{\omega}(1 - m_E)\right) = 0, \quad (26)$$

where $\bar{\gamma}_1 = \sqrt{1 - \frac{\tilde{\omega}^2}{\bar{\kappa}}}$. For the sake of simplicity, we will consider the case when the fluid saturating the porous medium is identical to that occupying the region $y < 0$. In this case, $\bar{\kappa} = \kappa$ and $\bar{\gamma}_1 = \tilde{\gamma}_1$.

Dispersion equation (26) has three roots. The asymptotic expansion of the first of them yields

$$\tilde{\omega}_1 = \sqrt{\kappa}(1 - c_1\kappa^2 + O(\kappa^3)), \quad (27)$$
$$c_1 = \frac{((1 + m_E)\rho_{f0} + (1 - 3m_E)\bar{\rho}_{f0})^2}{2a_{s2}^4\mu^2\left(\frac{1}{a_{s2}^2} - \frac{1}{a_{s1}^2}\right)^2(1 + m_E)^2}.$$

As in the case of the free boundary of a porous medium, $\mathrm{Re}\,\tilde{\omega}_1$ defines the phase velocity of a very slow wave, namely, the Stoneley wave. Its velocity is of the order of $O(\sqrt{\kappa})$. Consequently, this wave is slower than all the bulk waves in the porous medium and in the fluid. As is well known [3], precisely such a wave propagates along the ocean bottom during earthquakes.

Dispersion equation (26) also has two complex roots corresponding to surface waves localized with respect to y, whose phase velocities are close to $\sqrt{\kappa}$ and a_{s2}, respectively. The asymptotic behavior of one of these roots takes the form

$$\tilde{\omega}_2 = \sqrt{\kappa}(1 + c_2\kappa + c_3\kappa^{3/2} + O(\kappa^2)), \quad (28)$$

$$\sqrt{c_2} = \frac{\alpha^2}{2}(1 + m_E)^2, \quad c_3 = -i\frac{2}{a_{s2}^2}\frac{\bar{\rho}_{f0}\alpha m_E}{\mu\left(\frac{1}{a_{s2}^2} - \frac{1}{a_{s1}^2}\right)}. \quad (29)$$

This root defines a weakly damping leaky Stoneley pseudowave whose phase velocity is much higher than $\sqrt{\kappa}$.

Another complex root corresponds to the Rayleigh generalized wave:

$$\tilde{\omega}_{R'} = \Omega_0 + \sqrt{\kappa}\Omega_1 + O(\kappa), \quad (30)$$

where, $\Omega_0 = c_R$ and the following equation for Ω_1 is valid:

$$i\sqrt{1 - \frac{\Omega_0^2}{a_{s1}^2}}\frac{\bar{\rho}_{f0} + \rho_{f0}}{\rho_{s0}}\frac{\Omega_0^3}{a_{s2}^4} - \left[\frac{4}{a_{s2}^4}\Omega_0^3 - \frac{8}{a_{s2}^2}\Omega_0\right.$$
$$\left. - 4\frac{d}{d\tilde{\omega}}\left(\sqrt{1 - \frac{\tilde{\omega}^2}{a_{s1}^2}}\sqrt{1 - \frac{\tilde{\omega}^2}{a_{s2}^2}}\right)\right|_{\tilde{\omega} = \Omega_0}\Omega_1 = 0.$$

SURFACE WAVES ON THE INTERFACE OF TWO DIFFERENT POROUS MEDIA

We consider the two half-spaces Ω^I ($y > 0$) and Ω^{II} ($y < 0$) having the common interface Γ ($y = 0$). Let both regions Ω^I and Ω^{II} be filled with saturated porous media having different structures. Boundary conditions (7)–(10) must be fulfilled on the interface $y = 0$. We consider two typical cases: (1) media with different porosities, but with the Lamé coefficients of their solid phases and the parameters of the saturating fluids both being identical; (2) media with both different porosities and different Lamé coefficients, but with the parameters of the saturating fluids being identical. In the

former case, the dispersion equation is

$$(2\tilde{\gamma}_1\tilde{\mu}_s\rho_{s0} + (\rho_{f0} + \bar{\rho}_{f0})(\tilde{\mu}_s\tilde{\gamma}_2 - 1))$$
$$\times\left(\tilde{\gamma}_1 - i\alpha\tilde{\omega}\left(1 + \frac{m_E}{\bar{m}_E}\right)\right) \qquad (31)$$
$$+ 2\bar{\rho}_{f0}(\tilde{\mu}_s\tilde{\gamma}_2 - 1)\left(\tilde{\gamma}_1 - i\alpha\tilde{\omega}\left(1 - \frac{\rho_{f0}}{\bar{\rho}_{f0}}\right)\right) = 0.$$

In the latter case, we obtain a more complicated dispersion equation,

$$\tilde{\gamma}_1\left(\frac{1}{2}\left(1 - \frac{\bar{\rho}_{s0}}{\rho_{s0}}\right)^2(1 - \tilde{\mu}_s\tilde{\gamma}_2)\mathcal{P}_R - 2\frac{\tilde{\omega}^4}{a_{s2}^4}\frac{\bar{\rho}_{s0}}{\rho_{s0}}\tilde{\mu}_s\tilde{\gamma}_2\right)$$
$$\times\left(\tilde{\gamma}_1 - i\alpha\tilde{\omega}\left(1 + \frac{m_E}{\bar{m}_E}\right)\right) + \tilde{\gamma}_2\frac{\tilde{\omega}^4}{2a_{s2}^4}\left(1 + \frac{\bar{\rho}_{s0}}{\rho_{s0}}\right)$$
$$\times(1 - \tilde{\mu}_s\tilde{\gamma}_2)\frac{\rho_{f0}}{\rho_{s0}}\left(\tilde{\gamma}_1\left(1 + \frac{\bar{\rho}_{f0}}{\rho_{f0}}\right)\right. \qquad (32)$$
$$\left. + i\alpha\tilde{\omega}\left(1 - \frac{m_E}{\bar{m}_E}\right)\left(1 - \frac{\bar{\rho}_{f0}}{\rho_{f0}}\right)\right) = 0.$$

Dispersion equation (31) has three roots. As in the cases described above for the free boundary of a porous medium and the interface of a porous medium and a fluid, the first two roots correspond to a very slow wave and to the Stoneley pseudowave, with their phase velocities slightly lower and slightly higher than $\sqrt{\kappa}$, respectively. The velocity of the Stoneley wave significantly depends on the fluid compressibility coefficient. The velocity of the Stoneley pseudowave also depends on the surface-penetrability coefficient α. The third complex root corresponds to a new surface wave, which exists neither in the case of the free boundary of a porous medium nor in the case of the porous-medium–fluid interface. The phase velocity of this wave is very close to, but slightly higher than, the velocity a_{s2} of a transverse wave in an infinite elastic space. The asymptotic expansion of the root yields

$$\tilde{\omega}_3 = a_{s2}(1 + c_4\kappa + c_5\kappa^{3/2} + O(\kappa^2)), \qquad (33)$$

$$c_4 = \frac{(\rho_{f0} + \bar{\rho}_{f0})^2}{8\rho_{s0}^2 a_{s2}^2},$$

$$c_5 = 2\alpha\rho_{f0}\left(1 + \frac{m_E\bar{\rho}_{f0}}{\bar{m}_E\rho_{f0}}\right)\frac{\rho_{f0} + \bar{\rho}_{f0}}{(2\rho_{s0}a_{s2})^2}$$
$$+ i\frac{(\rho_{f0} + \bar{\rho}_{f0})^3}{(2\rho_{s0}a_{s2})^3}\sqrt{1 - \frac{a_{s2}^2}{a_{s1}^2}}.$$

This root defines the damping leaky surface wave, whose phase velocity is very close, as in the case of the Rayleigh generalized wave, to the velocity a_{s2} of the transverse wave. It is easy to estimate that the energy of this wave is partially transmitted to a slow longitudinal wave. If $\rho_{f0}, \bar{\rho}_{f0} \longrightarrow 0$, this surface mode degenerates to a transverse bulk wave, in contrast to the generalized Rayleigh wave passing into the classical Rayleigh wave. It should be noted that the amplitude of this wave slowly increases with t. This implies that this surface wave exists as an isolated wave only for a short period of time.

Thus, dispersion equation (32) has four roots; they define the Stoneley wave and pseudowave, the Rayleigh wave, and a new surface mode whose phase velocity is slightly higher than the velocity a_{s2} of the transverse wave.

REFERENCES

1. Lord Rayleigh, Proc. London Math. Soc., No. 17, 4 (1885).
2. A. E. H. Love, *Some Problems in Geodynamics* (Cambridge Univ. Press, London, 1926).
3. I. A. Viktorov, *Sound Surface Waves in Solids* (Nauka, Moscow, 1981).
4. K. Wilmanski, *Thermomechanics of Continua* (Springer-Verlag, Berlin, 1998).
5. K. Wilmanski, in *Proceedings of the WASCOM'99, Vulcano, 1999.*
6. I. Edelman, K. Wilmanski, and E. Radkevich, Preprint No. 513, WIAS (Berlin, 1999).
7. I. Edelman and K. Wilmanski, Preprint No. 531, WIAS (Berlin, 1999).
8. I. Edelman and K. Wilmanski, Preprint No. 568, WIAS (Berlin, 2000).

Translated by V. Bukhanov

Doklady Physics, Vol. 46, No. 7, 2001, pp. 522–525. Translated from Doklady Akademii Nauk, Vol. 379, No. 3, 2001, pp. 329–333.
Original Russian Text Copyright © 2001 by Astashev, Krupenin.

MECHANICS

Experimental Investigation of Vibrations of Strings Interacting with Point Obstacles

V. K. Astashev and V. L. Krupenin

Presented by Academician K.V. Frolov June 27, 2000

Received February 13, 2001

This paper presents the results of an experimental study of a distributed system (a string) whose motion is accompanied by its interaction with point obstacles. The study concerns the dynamical effects that occur in such systems and attend the origination of both periodic trapezoidal standing waves and standing waves of other types characterized by wave profiles composed of segments of straight lines.

1. Elements of the theory of distributed vibroimpact systems (strings) with point obstacles are developed in papers [1, 2]. The need for such a theory is associated with designing various elements of machines and various measuring devices, for example, electroacoustic (string) tensometers [2]. Until recently, the models used by designers were incomplete, because possible collisions of strings with rigid elements of structures were not always taken into account.

The theory of vibroimpact systems with distributed impact elements [3–5] is now making its first steps (reviews [6, 7] contain some bibliographical references). Along with long obstacles, this theory considers point obstacles which are introduced into the model on the condition that an obstacle is negligible in length as compared to a vibrating object [1, 2].

Both types of the mentioned systems are related, because, in the first case, the dimensions of impact elements are comparable to the lengths of impact-induced elastic waves, while, in the second, the times of impact interaction and of elastic-wave propagation in a distributed impact element are comparable to each other due to the indispensable dwell of the distributed elements near point obstacles.

To some extent, the theory of systems with distributed impact elements and of related systems with parallel impact pairs has been verified experimentally. It appears that in this paper, we describe and systematize, for the first time, experimental data on dynamical phenomena originating from the interaction of vibrating strings with point obstacles. It is shown that, as with long obstacles, the resulting vibroimpact processes are accompanied by the appearance of both periodic trapezoidal standing waves and standing waves of other types characterized by knees in their wave profiles. The experiments were carried out by using an "Alligator-T" setup (Blagonravov Institute of Engineering Science, Russian Academy of Sciences).

2. Dynamical models of standing waves that arise in distributed systems interacting with point obstacles are constructed in the way discussed below [2]. We consider a model of a linear one-dimensional distributed system. Such a system can be represented, for example, by a stretched string, a beam, or another similar object having length l and can be determined by the dynamic-compliance operator $L(x, y; p)$ [8], where $x, y \in [0, l]$, and $p = d/dt$ represents the differential operator. The form of this operator is determined, in particular, by the geometric and/or dynamical structure of the system and by the boundary conditions.

Let a point obstacle situated at the point (a, Δ) bound the desired displacement $u(x, t)$ so that $u(a, t) \geq \Delta$. Assuming that motion is caused by the T-periodic distributed force, the relation determining the T-periodic vibroimpact processes can be represented as

$$u(x, t) = u_0(x, t) - \int_{\tau}^{\theta} R(s)\chi(x, a, t-s)ds. \qquad (1)$$

Here, $\chi(x, y; t)$ is the T-periodic Green function corresponding to the linear system and is completely determined by the operator L [8]; the T-periodic standing wave $u_0(x, t)$ is determined by solving the corresponding linear problem; and the time instants $\tau, \theta \in [0, T]$ that determine the system dwell $t^* = |\theta - \tau|$ at the obstacle, as well as the reaction $R(t)$, are to be determined from certain additional conditions (see [1, 2]). In these papers, analytic expressions for the desired standing waves with polygonal profiles are derived, in particular, with the help of representations of type (1). Such experimentally obtained waves are considered here.

3. A brief description of the "Alligator-T" setup (Fig. 1) is given below. As a distributed elastic element,

Blagonravov Mechanical Institute of Engineering Science, Russian Academy of Sciences,
ul. Griboedova 4, Moscow, 101830 Russia

1028-3358/01/4607-0522$21.00 © 2001 MAIK "Nauka/Interperiodica"

we use a rubber cord, *1*. One end of this cord is connected rigidly to a force gage, *2*, which is mounted on a frame and measures the component of cord tension in the direction perpendicular to the cord axis. The gage signal, which is proportional to the rotation angle of the cord about its fixed point, is registered by a cathode-ray oscilloscope, *3*. The second end of the cord is connected to the armature of an electrodynamic exciter, *4*, which excites transverse vibrations of the cord. An electric-oscillation generator, *5*, provides a power supply to the exciter. To change the natural frequencies of the cord, the structure of its mounts allows one to make adjustments to the tension. Point obstacles, *6*, having the shape of thin bars are mounted perpendicularly to the plane of cord vibrations on a carriage, *7*, which allows one to vary the clearance between them and the cord. In addition, due to the setup structure, we can change both the number of obstacles and their positions on the cord axis.

Cord shapes and their transformations during vibrations were photographed by a camera, *8*, in the flashing light of a stroboscopic lamp, *9*, powered from a motion analyzer, *10*. The results presented correspond to the case when, in the absence of collisions, the first natural frequency of the 52-cm-long cord is equal to $f = 33$ Hz and the obstacles are mounted with a clearance $\Delta = 12$ mm.

The experiments revealed the frequency zones of excitation of nonlinear waves with profiles that consist of segments of straight lines and have different configurations at different numbers and positions of the point obstacles.

4. The photographs presented in Fig. 2 show the wave configurations formed in different stages of cord motion at different numbers and positions of the obstacles.

The configurations shown in Figs. 2a–2c correspond to the case of cord excitation at a frequency $f = 39$ Hz. The only obstacle is situated in the middle of the cord at a clearance $\Delta = 12$ mm. At the instant of maximum cord deflection from the obstacle, when all cord points are immovable, the wave configuration has the form of an isosceles triangle (Fig. 2a). During motion within the clearance, the wave takes on the shape of an isosceles trapezoid (Fig. 2b). The lateral sides of the trapezoid are immovable, while its small base moves with a constant velocity and increases (decreases) in length during motion to (from) the central position. Note that similar waves were observed experimentally in the study of motions of distributed systems with a long obstacle [9] and discrete multiple-mass systems with multiple parallel impact pairs [10]. When the small base of the trapezoid reaches the obstacle, the contact point stops and the wave configuration changes: the trapezoid splits into two parts as though it were flowing around the obstacle, (Fig. 2c). In the final position, in which all points of the cord are immovable, the cord takes on the shape of triangular prongs (Fig. 2c), the lateral sides of which converge to the obstacle point. In addition, the cord shape is always symmetric with respect to its middle. Such behavior of cord shapes is verified by the oscillogram of the signal received from the force gage (Fig. 3). According to it, when the cord passes through its neutral position, the registered force and, consequently, the angle of rotation of the cord about its fixed point change in a jumplike fashion and remain constant during a vibration half-cycle.

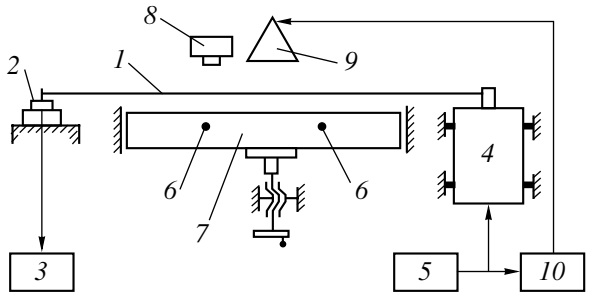

Fig. 1. Schematic diagram of the experimental setup.

In the experiments with one point obstacle, we investigated the effect of obstacle-position asymmetry with respect to the cord middle on a standing-wave profile.

It is established that, as the obstacle shifts its position on the cord, the cord profile containing straight segments with sharp transitions between them becomes more and more asymmetric. The photographs of cord configurations taken in different stages of cord motion excited at the same frequency $f = 39$ Hz illustrate the above-mentioned behavior (Figs. 2d–2f). The distances between the obstacle and the fixed points of the cord are equal to 29 and 23 cm, respectively. Deflecting from the obstacle to the maximum, the cord (Fig. 2d), all points of which are immovable, takes on an almost triangular form, where the triangle vertex is shifted from the cord middle to the side opposite to the obstacle shift. As the wave vertex moves to the obstacle, its smearing with formation of a straight plateau occurs (Fig. 2e). When moving to the obstacle, the plateau expands and, near the obstacle, becomes symmetric with respect to it. Moving further, the cord rounds the obstacle and, in its final position, forms sharp prongs off both sides of the obstacle (Fig. 2f).

5. A series of experiments carried out with a system containing two point obstacles revealed a similar behavior of the wave processes. The photographs presented in Figs. 2g, 2h, and 2i illustrate the transformations of a wave profile in different stages of cord motion, where the cord interacts with two point obstacles situated asymmetrically at distances of 22 and 14 cm from its fixed points. When the cord moves within the clearance, its shape, being triangular in the initial configuration (Fig. 2g), becomes trapezoidal in this case too, where the small base of the trapezoid varies in length during its motion (Fig. 2h). As in the previous cases, after reaching the obstacles, the cord rounds them and forms characteristic sharp prongs off both sides of each obstacle (Fig. 2i). The photographs

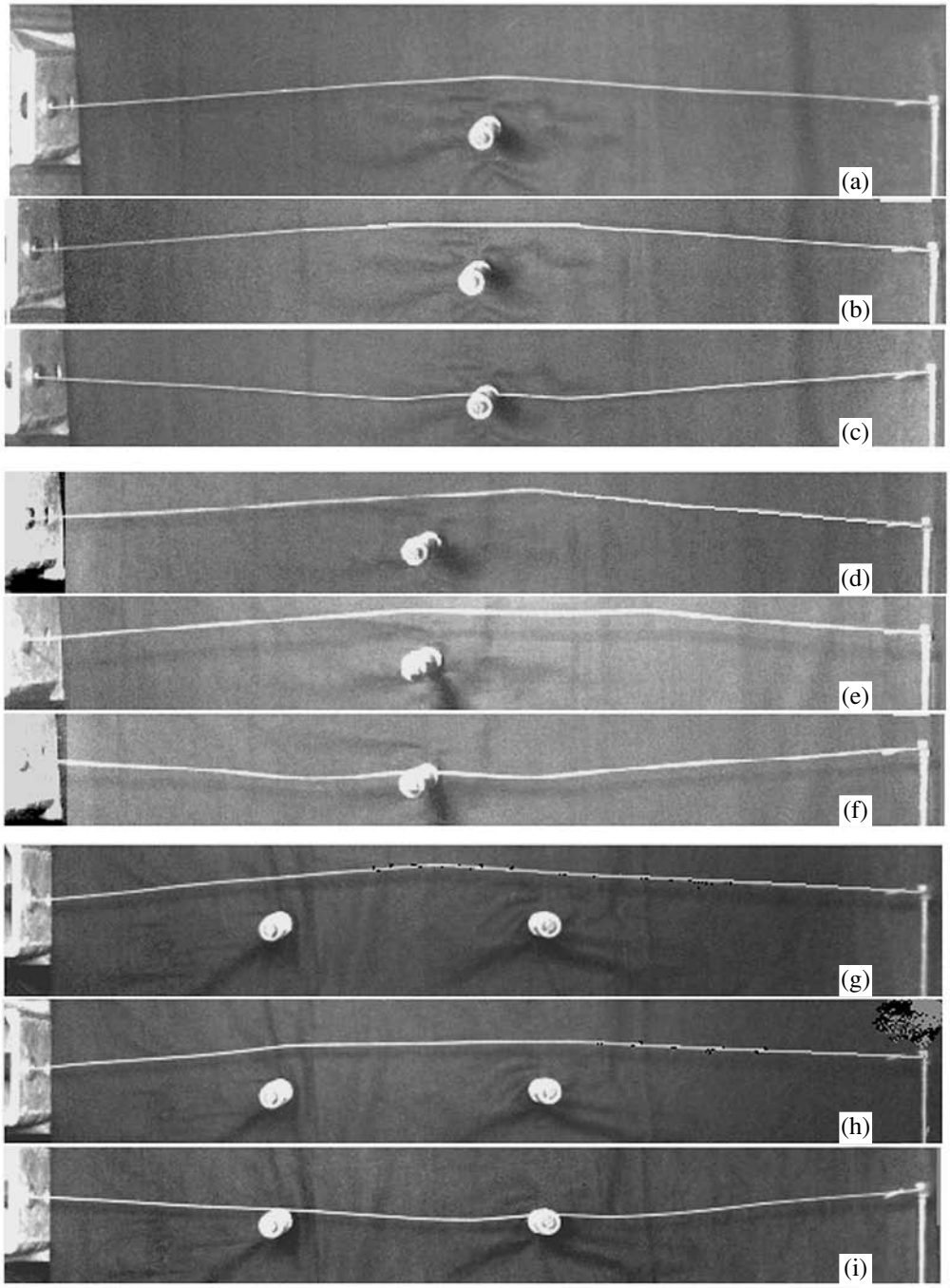

Fig. 2. A cord in different stages of motion in the systems with one or two obstacles.

presented are taken for vibrations excited at a frequency $f = 37$ Hz.

The cord interacting with the two obstacles situated symmetrically to one another behaves in a similar way. The only difference is that its profile is always symmetric with respect to its middle.

6. Dynamical effects. As in other cases of experimental and theoretical study of nonlinear wave processes in distributed vibroimpact systems [2–6], the experiments carried out here have shown that, when the above-described standing waves are formed in the considered systems with point obstacles, the behavior of these systems is similar to the behavior of conventional vibroimpact systems with one lumped impact pair. The experimental results take the form of amplitude–frequency characteristics of the systems, where, we take half of the distance between the wave peaks as the amplitude, which is measured in the direction of vibrations in extreme cord positions.

Figure 4 shows an amplitude–frequency characteristic of the system with one obstacle mounted symmetrically at a clearance $\Delta = 12$ mm. If the amplitude of the vibrations lies within the clearance ($a < \Delta$), the realized branches represent resonance curves for the cord without an obstacle. Branch for $a > \Delta$ corresponds to vibrations accompanied by cord collisions with the obstacle. Amplitude–frequency characteristics for the other above-considered systems with one or two obstacles have a similar form. One can see that the behavior of the systems under consideration is similar to that of conventional vibroimpact systems with one asymmetric impact pair [7, 8]. It reveals the dynamical effects discussed below.

Frequency pulling. All observed types of standing waves can be pulled from the frequency f_1, which is close to the natural frequency f_0 of linear cord vibrations, to the frequency f_3 at which vibration quenching occurs; this frequency is higher than f_0. It is established that, for the same clearance, the range of frequency pulling decreases with increasing both the number of obstacles and asymmetry of their mounting. For example, in the systems with one obstacle mounted symmetrically and with two asymmetric obstacles, the frequencies of vibration quenching are $f_3 = 41$ and 38.5 Hz, respectively.

Two-valuedness of amplitude–frequency characteristics. There is a frequency range in which the amplitude–frequency characteristics are two-valued. Paper [2] shows that skeleton curves exist in the range $f_0 < f < \frac{4}{3} f_0$. All regions observed experimentally fall in this frequency range.

Vibration quenching. When the frequency becomes higher than the cutoff frequency f_3 of the pulling, quenching of each nonlinear standing wave occurs (i.e., the vibroimpact process disappears), and the sinusoidal excitation results in the formation of linear standing waves, the amplitudes of which lie within the clearance. When, while decreasing the excitation frequency passing through the quenching frequency, the linear waves do not disappear down to the frequency f_2 at which the vibrations jump to the upper vibroimpact branch characterized by the formation of trapezoidal waves.

Hard excitation. Being excited under zero initial conditions for vibrations in the frequency range $f_2 < f < f_3$, the waves formed in the system are linear and have an amplitude $a < \Delta$. As in the case of the conventional vibroimpact systems with one impact pair, a possible way of exciting the regimes corresponding to the upper branch of the amplitude–frequency characteristic lies in imparting an additional starting initial energy to the system. Due to this energy, the trapezoidal waves can form at the same excitation frequencies as the linear waves. This two-valuedness is quite similar to the known property of the conventional systems with one impact pair [7, 8]. By using the same analogy, we impart the above-mentioned starting initial conditions to the "hard excitation" system [7, 8].

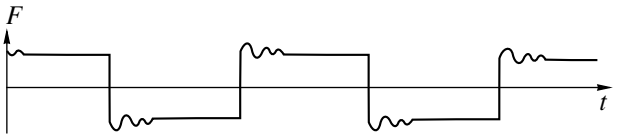

Fig. 3. Oscillogram of the cord-tension component in the direction of vibrations.

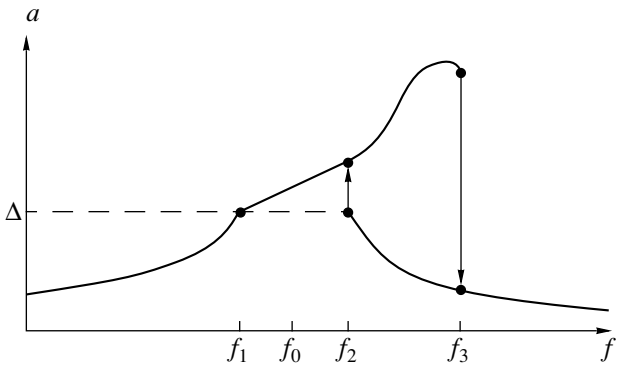

Fig. 4. Amplitude–frequency characteristic of a cord with one point obstacle.

The above-mentioned effects accompany all types of periodic trapezoidal standing waves observed experimentally.

ACKNOWLEDGMENTS

This study was supported by the Russian Foundation for Basic Research, projects no. 98-01-00925 and 01-01-00297.

REFERENCES

1. H. Cabanes and A. Haraus, Int. J. Non-Linear Mech. **55**, 449 (1981).
2. V. L. Krupenin, Probl. Mashinostr. Nadezhnosti Mash., No. 2, 29 (1992).
3. L. Amerio and G. Prouse, Rend. Mat. **6**, 563 (1975).
4. V. L. Krupenin, Izv. Akad. Nauk SSSR, Mekh. Tverd. Tela, No. 1, 25 (1986).
5. V. L. Krupenin, Dokl. Akad. Nauk SSSR **313**, 1394 (1990) [Sov. Phys. Dokl. **35**, 743 (1990)].
6. H. Cabanes, Acustica **55**, 14 (1984).
7. V. K. Astashev and V. L. Krupenin, Probl. Mashinostr. Nadezhnosti Mash., No. 5, 13 (1998).
8. V. I. Babitsky and V. L. Krupenin, *Oscillations in Strongly Nonlinear Systems* (Nauka, Moscow, 1985).
9. A. M. Veprik and V. L. Krupenin, Mashinovedenie, No. 6, 39 (1986).
10. V. K. Astashev, V. L. Krupenin, and A. N. Tresvyatskiĭ, Dokl. Akad. Nauk **351**, 44 (1996) [Phys. Dokl. **41**, 532 (1996)].

Translated by Yu. Verevochkin

Doklady Physics, Vol. 46, No. 7, 2001, pp. 526–531. Translated from Doklady Akademii Nauk, Vol. 379, No. 3, 2001, pp. 334–339.
Original Russian Text Copyright © 2001 by Polyanin.

MECHANICS

Transformations and Exact Solutions Containing Arbitrary Functions for Boundary-Layer Equations

A. D. Polyanin

Presented by Academician F.L. Chernous'ko March 6, 2001

Received March 11, 2001

In this paper, the general transformations that retain the form of the equations for a three-dimensional boundary layer in an arbitrary orthogonal curvilinear coordinate system are found anisothermic and diffusion boundary layers in Newtonian and non-Newtonian fluids are investigated. New exact solutions to the equations of both steady and unsteady boundary layers, which depend on arbitrary functions, are cited. A simple approximate method of solving the boundary layer problems on flows past smooth weakly deformed surfaces is described.

1. Equations for a two-dimensional unsteady boundary layer. The equations for a two-dimensional unsteady laminar boundary layer take the form

$$\frac{\partial u_1}{\partial t} + u_1\frac{\partial u_1}{\partial x} + u_2\frac{\partial u_1}{\partial y} = \nu\frac{\partial^2 u_1}{\partial y^2} + f(x,t), \qquad \frac{\partial u_1}{\partial x} + \frac{\partial u_2}{\partial y} = 0. \tag{1}$$

Here, x and y are the longitudinal and transverse coordinates (the zero value of y corresponds to the flow surface); u_1 and u_2 are the longitudinal and transverse components of the fluid velocity, respectively; ν is the kinematic viscosity of the fluid; and $\nabla_x p = -\rho f(x,t)$ is the pressure gradient.

By introducing the stream function w according to the formulas $u_1 = \dfrac{\partial w}{\partial y}$ and $u_2 = -\dfrac{\partial w}{\partial x}$, we reduce set (1) to a single nonlinear equation of the third order [1, 2]:

$$\frac{\partial^2 w}{\partial t\partial y} + \frac{\partial w}{\partial y}\frac{\partial^2 w}{\partial x\partial y} - \frac{\partial w}{\partial x}\frac{\partial^2 w}{\partial y^2} = \nu\frac{\partial^3 w}{\partial y^3} + f(x,t). \tag{2}$$

Equation (2) is invariant with respect to the transformation

$$w = W(x,\xi,t) + \frac{\partial}{\partial t}\int\varphi(x,t)\,dx, \quad \xi = y + \varphi(x,t), \tag{3}$$

where $\varphi(x,t)$ is an arbitrary function of two variables.

Transformation (3) was derived in [3] in terms of velocity components; the steady cases of $\varphi = \varphi(x)$ were described in [4] (see also [5, 6]). This transformation will be used in Section 6 for constructing exact solutions to the boundary-layer equations.

2. Three-dimensional boundary-layer equations. The three-dimensional equations for an unsteady laminar boundary layer in the Cartesian coordinate system take the form

$$\frac{\partial u_1}{\partial t} + u_1\frac{\partial u_1}{\partial x} + u_2\frac{\partial u_1}{\partial y} + u_3\frac{\partial u_1}{\partial z} = \nu\frac{\partial^2 u_1}{\partial z^2} + f_1(x,y,t), \tag{4}$$

$$\frac{\partial u_2}{\partial t} + u_1\frac{\partial u_2}{\partial x} + u_2\frac{\partial u_2}{\partial y} + u_3\frac{\partial u_2}{\partial z} = \nu\frac{\partial^2 u_2}{\partial z^2} + f_2(x,y,t), \tag{5}$$

$$\frac{\partial u_1}{\partial x} + \frac{\partial u_2}{\partial y} + \frac{\partial u_3}{\partial z} = 0, \tag{6}$$

where $u_k = u_k(x,y,z,t)$ are the components of the fluid velocity ($k = 1, 2, 3$) and z is the coordinate counted along the normal to the flow surface. In the right-hand sides of Eqs. (4) and (5), nonpotential mass forces are involved along with the pressure gradient; i.e., the functions $f_1(x,y,t)$ and $f_2(x,y,t)$ are arbitrary.

The transformation

$$u_1 = v_1, \quad u_2 = v_2, \quad u_3 = v_3 - \varphi_x v_1 - \varphi_y v_2 - \varphi_t,$$
$$u_k = u_k(x,y,z,t), \quad v_k = v_k(x,y,\xi,t), \tag{7}$$
$$\xi = z + \varphi(x,y,t)$$

retains the form of Eqs. (4)–(6) for an unsteady boundary layer. Here, $\varphi = \varphi(x,y,t)$ is an arbitrary function of three variables and φ_x, φ_y, and φ_t are its partial derivatives with respect to x, y, and t, respectively. Transformation (7) with $(f_1)_y = (f_2)_x$ was obtained in [3] using methods of group analysis.

Institute of Problems of Mechanics,
Russian Academy of Sciences,
pr. Vernadskogo 101, Moscow, 117526 Russia

1028-3358/01/4607-0526$21.00 © 2001 MAIK "Nauka/Interperiodica"

Transformation (7) allows more general solutions dependent on an arbitrary function of three variables to be constructed by using any particular solutions to the boundary-layer equations (in particular, every steady solution generates the corresponding unsteady solutions). This transformation admits various generalizations (see Sections 3–5) and will be used in Section 8 to find approximate solutions to the problems of flow past smooth weakly deformed surfaces.

3. Boundary-layer equations for non-Newtonian fluids. The three-dimensional unsteady-state equations

$$\frac{\partial u_1}{\partial t} + u_1\frac{\partial u_1}{\partial x} + u_2\frac{\partial u_1}{\partial y} + u_3\frac{\partial u_1}{\partial z} = F_1\left(x, y, t, u_1, u_2, \frac{\partial u_1}{\partial z}, \frac{\partial u_2}{\partial z}, \frac{\partial^2 u_1}{\partial z^2}, \frac{\partial^2 u_2}{\partial z^2}\right),$$

$$\frac{\partial u_2}{\partial t} + u_1\frac{\partial u_2}{\partial x} + u_2\frac{\partial u_2}{\partial y} + u_3\frac{\partial u_2}{\partial z} = F_2\left(x, y, t, u_1, u_2, \frac{\partial u_1}{\partial z}, \frac{\partial u_2}{\partial z}, \frac{\partial^2 u_1}{\partial z^2}, \frac{\partial^2 u_2}{\partial z^2}\right),$$

and

$$\frac{\partial u_1}{\partial x} + \frac{\partial u_2}{\partial y} + \frac{\partial u_3}{\partial z} = 0$$

are invariant with respect to transformation (7), with the functions F_1 and F_2 being arbitrary. Special cases with similar equations are widely used for describing a boundary layer in non-Newtonian fluids [7, 8].

4. Equations for anisothermic and diffusion boundary layers. We consider now a more complicated set of equations

$$\frac{\partial u_1}{\partial t} + u_1\frac{\partial u_1}{\partial x} + u_2\frac{\partial u_1}{\partial y} + u_3\frac{\partial u_1}{\partial z} = F_1, \quad (8)$$

$$\frac{\partial u_2}{\partial t} + u_1\frac{\partial u_2}{\partial x} + u_2\frac{\partial u_2}{\partial y} + u_3\frac{\partial u_2}{\partial z} = F_2, \quad (9)$$

$$\frac{\partial u_1}{\partial x} + \frac{\partial u_2}{\partial y} + \frac{\partial u_3}{\partial z} = F_3, \quad (10)$$

$$\frac{\partial \theta}{\partial t} + u_1\frac{\partial \theta}{\partial x} + u_2\frac{\partial \theta}{\partial y} + u_3\frac{\partial \theta}{\partial z} = F_4, \quad (11)$$

whose right-hand sides contain the arbitrary functions

$$F_n = F_n\left(x, y, t, u_1, u_2, \theta, \frac{\partial u_1}{\partial z}, \frac{\partial u_2}{\partial z}, \frac{\partial \theta}{\partial z}, \frac{\partial^2 u_1}{\partial z^2}, \frac{\partial^2 u_2}{\partial z^2}, \frac{\partial^2 \theta}{\partial z^2}\right),$$

$$n = 1, 2, 3, 4.$$

Special cases with similar equations are used for describing an anisothermic boundary layer in Newtonian and non-Newtonian fluids [1, 2, 7, 8] (including problems with thermal sources, those with viscous dissipation or with free convection, and problems where the viscosity is dependent on the temperature θ). They can also be encountered in problems on diffusion boundary layers (including problems with chemical reactions [8]).

The transformation

$$u_1 = v_1, \quad u_2 = v_2,$$
$$u_3 = v_3 - \varphi_x v_1 - \varphi_y v_2 - \varphi_t, \quad \theta = \vartheta,$$
$$u_k = u_k(x, y, z, t), \quad \theta = \theta(x, y, z, t),$$
$$v_k = v_k(x, y, \xi, t), \quad \vartheta = \vartheta(x, y, \xi, t),$$
$$\xi = z + \varphi(x, y, t)$$

retains the form of Eqs. (8)–(11). Here, $\varphi = \varphi(x, y, t)$ is an arbitrary function of three variables and φ_x, φ_y and φ_t are its partial derivatives.

Remark 1. These results can be easily extended to a multicomponent case. To do this, several similar equations for θ_m have to be added to Eqs. (8)–(10) instead of one equation (11) (the right-hand sides of these equations can depend on all θ_m and on their first and second derivatives with respect to z).

5. Three-dimensional boundary-layer equations in an arbitrary orthogonal coordinate system. The three-dimensional equations for a laminar unsteady boundary layer in an arbitrary orthogonal curvilinear coordinate system take the form [9]

$$\frac{\partial u_1}{\partial t} + \frac{u_1}{\sqrt{g_{11}}}\frac{\partial u_1}{\partial x_1} + \frac{u_2}{\sqrt{g_{22}}}\frac{\partial u_1}{\partial x_2} + \frac{u_3}{\sqrt{g_{33}}}\frac{\partial u_1}{\partial x_3} + A_1u_2^2 + B_1u_1u_2 = \frac{\nu}{\sqrt{g_{33}}}\frac{\partial^2 u_1}{\partial x_3^2} + f_1(x_1, x_2, t),$$

$$\frac{\partial u_2}{\partial t} + \frac{u_1}{\sqrt{g_{11}}}\frac{\partial u_2}{\partial x_1} + \frac{u_2}{\sqrt{g_{22}}}\frac{\partial u_2}{\partial x_2} + \frac{u_3}{\sqrt{g_{33}}}\frac{\partial u_2}{\partial x_3} + A_2u_1^2 + B_2u_1u_2 = \frac{\nu}{\sqrt{g_{33}}}\frac{\partial^2 u_2}{\partial x_3^2} + f_2(x_1, x_2, t),$$

$$\frac{\partial}{\partial x_1}\left(u_1\sqrt{\frac{g}{g_{11}}}\right) + \frac{\partial}{\partial x_2}\left(u_2\sqrt{\frac{g}{g_{22}}}\right) + \frac{\partial}{\partial x_3}\left(u_3\sqrt{\frac{g}{g_{33}}}\right) = 0.$$

Here, $u_k = u_k(x_1, x_2, x_3, t)$ are the components of the fluid velocity ($k = 1, 2, 3$), x_3 is the coordinate along the normal to the flow surface specified by the value $x_3 = 0$, $g_{kk} = g_{kk}(x_1, x_2)$ are the components of a metric tensor at $x_3 = 0$, and $g = g_{11}g_{22}g_{33}$ is the third invariant of the metric tensor. The functions $A_n = A_n(x_1, x_2)$ and $B_n = B_n(x_1, x_2)$, where $n = 1, 2$, are expressed through the metric-tensor components and their derivatives at $x_3 = 0$. In the right-hand sides of the equations, nonpotential mass forces

are included in addition to the pressure gradient; i.e., the functions $f_1(x_1, x_2, t)$ and $f_2(x_1, x_2, t)$ are arbitrary.

The transformation

$$u_1 = v_1, \quad u_2 = v_2, \quad u_3 = v_3 - \psi_1 v_1 - \psi_2 v_2 - \psi_3,$$
$$u_k = u_k(x_1, x_2, x_3, t), \quad v_k = v_k(y_1, y_2, y_3, t),$$
$$y_1 = x_1, \quad y_2 = x_2, \quad y_3 = x_3 + \varphi(x_1, x_2, t)$$

retains the form of the equations for an unsteady boundary layer in an arbitrary orthogonal curvilinear coordinate system. Here,

$$\psi_1 = \sqrt{\frac{g_{33}}{g_{11}}}\frac{\partial \varphi}{\partial x_1}, \quad \psi_2 = \sqrt{\frac{g_{33}}{g_{22}}}\frac{\partial \varphi}{\partial x_2}, \quad \psi_3 = \sqrt{g_{33}}\frac{\partial \varphi}{\partial t},$$

and $\varphi = \varphi(x_1, x_2, t)$ is an arbitrary function of three variables.

Remark 2. The results of this section are applicable to three-dimensional equations for an unsteady boundary layer in non-Newtonian fluids written in an arbitrary orthogonal curvilinear coordinate system.

Remark 3. The results of this section are also applicable to three-dimensional equations for an unsteady anisothermic (diffusion) boundary layer in incompressible fluids, which are written in an arbitrary orthogonal curvilinear coordinate system.

6. Usage of the transformations for constructing exact solutions to the boundary-layer equations. Transformation (3) allows more general solutions dependent on an arbitrary function of two variables to be constructed by using arbitrary particular solutions to the two-dimensional boundary-layer equation (in particular, every steady solution generates the corresponding unsteady solutions).

Consequence of transformation (3). If $w = w(x, y, t)$ is a solution to Eq. (2) for a hydrodynamical boundary layer, then the function

$$w_1 = w(x, y + \varphi(x, t), t) + \frac{\partial}{\partial t}\int \varphi(x, t)\,dx \qquad (12)$$

is also a solution to this equation.

1°. In particular, the following exact solutions to Eq. (2) with $f \equiv 0$ can be obtained with the help of formula (12):

$$w = \frac{6\nu x + C_1}{y + \varphi(x)} + \frac{C_2}{[y + \varphi(x)]^2} + C_3,$$

$$w = \varphi(x)\exp(-C_1 y) + \nu C_1 x + C_2,$$

$$w = C_1 \exp[-C_2 y - C_2 \varphi(x)] + C_3 y + C_3 \varphi(x) + \nu C_2 x + C_4,$$

$$w = 6\nu C_1 x^{1/3}\tanh\xi + C_2, \quad \xi = C_1\frac{y}{x^{2/3}} + \varphi(x),$$

$$w = -6\nu C_1 x^{1/3}\tan\xi + C_2, \quad \xi = C_1\frac{y}{x^{2/3}} + \varphi(x).$$

Here, $\varphi(x)$ is an arbitrary function and C_1, C_2, C_3, and C_4 are arbitrary constants. For constructing the second, third, and fourth solutions, we use the simpler solutions given in [1, 2, 4, 6] as a basis. For the sake of simplicity, we here present the solutions to the steady-state equation corresponding to the case of $\varphi(x, t) = \varphi(x)$ in (12).

2°. As an example of general solution (12), we now present the following exact solution to the unsteady-state equation with $f \equiv 0$ (which generalizes the second solution cited above):

$$w(x, y, t) = \psi(x)\exp[-\lambda y + \lambda\varphi(x, t)] - \frac{\partial}{\partial t}\int \varphi(x, t)\,dx + \nu\lambda x,$$

where $\varphi(x, t)$ and $\psi(x)$ are arbitrary functions and λ is an arbitrary parameter.

We also cite the inviscid solution to Eq. (2) with an arbitrary function $f(x, t)$:

$$w(x, y, t) = ay^2 + \varphi(x, t)y + \frac{1}{4a}\varphi^2(x, t) + \frac{1}{2a}\int\left[\frac{\partial \varphi}{\partial t} - f(x, t)\right]dx,$$

where $\varphi(x, t)$ is an arbitrary function and a is an arbitrary constant.

7. Exact solutions to the boundary-layer equations with the incomplete separation of variables. In this section, we describe new exact solutions to the two-dimensional unsteady boundary-layer equations with incomplete (generalized) separation of the variables. A series of exact solutions to the heat conduction equations and to other nonlinear second-order equations of mathematical physics with incomplete separation of the variables was cited in [10–12].

1°. Exact solutions to Eq. (2) in the case of $f(x, t) = f_1(t)x + f_2(t)$ take the form

$$w(x, y, t) = xF(y, t) + G(y, t), \qquad (13)$$

where the functions $F = F(y, t)$ and $G = G(y, t)$ are determined by the following simpler equations in two variables:

$$\frac{\partial^2 F}{\partial t \partial y} + \left(\frac{\partial F}{\partial y}\right)^2 - F\frac{\partial^2 F}{\partial y^2} = \nu\frac{\partial^3 F}{\partial y^3} + f_1(t), \qquad (14)$$

$$\frac{\partial^2 G}{\partial t \partial y} + \frac{\partial F}{\partial y}\frac{\partial G}{\partial y} - F\frac{\partial^2 G}{\partial y^2} = \nu\frac{\partial^3 G}{\partial y^3} + f_2(t). \qquad (15)$$

If $F = F(y, t)$ is a solution to Eq. (14), then the function

$$F_1 = F(y + \psi(t), t) + \psi_t'(t)$$

is also a solution to this equation, with $\psi(t)$ being an arbitrary function.

If a particular solution to Eq. (14) is known, the corresponding equation (15) can be reduced by substituting $U = \dfrac{\partial G}{\partial y}$ into the following linear equation of the second order:

$$\frac{\partial U}{\partial t} - F\frac{\partial U}{\partial y} = \nu\frac{\partial^2 U}{\partial y^2} - \frac{\partial F}{\partial y}U + f_2(t). \qquad (16)$$

Equation (14) has the exact solution

$$F(y, t) = a(t)y + b(t), \qquad (17)$$

where $a_t' + a^2 = f_1(t)$ and $b(t)$ is an arbitrary function.

Substituting solution (17) into Eq. (16), we have

$$\frac{\partial U}{\partial t} = \nu\frac{\partial^2 U}{\partial y^2} + [a(t)y + b(t)]\frac{\partial U}{\partial y} - a(t)U + f_2(t).$$

Performing the transformation

$$U = \frac{1}{\Phi(t)}[u(z, \tau) + \int f_2(t)\Phi(t)dt],$$

$$\tau = \int \Phi^2(t)dt + C_1, \quad z = y\Phi(t) + \int b(t)\Phi(t)dt + C_2,$$

where $\Phi(t) = \exp\left[\int a(t)dt\right]$, we reduce this equation to the conventional heat conduction equation with constant coefficients [12]:

$$\frac{\partial u}{\partial \tau} = \nu\frac{\partial^2 u}{\partial z^2}.$$

For $f_1(t) = 0$, Eq. (14) has two simple exact solutions:

$$F(y, t) = 6\nu[y + \psi(t)]^{-1} + \psi_t'(t),$$

$$F(y, t) = C\exp[-\lambda y + \lambda\psi(t)] - \psi_t'(t) + \nu\lambda,$$

where $\psi(t)$ is an arbitrary function, with C and λ being arbitrary constants.

2°. Exact solutions to Eq. (2) in the case of $f(x, t) = f(t)$ take the form

$$w(x, y, t) = \int u(z, t)dz + \varphi(t)y + \psi(t)x, \quad z = kx + \lambda y. \qquad (18)$$

Here, $\varphi(t)$ and $\psi(t)$ are arbitrary functions, k and λ are arbitrary parameters, and the function $u(z, t)$ is described by a linear parabolic equation of the second order:

$$\frac{\partial u}{\partial t} + [k\varphi(t) - \lambda\psi(t)]\frac{\partial u}{\partial z} = \nu\lambda^2\frac{\partial^2 u}{\partial z^2} - \frac{1}{\lambda}\varphi_t'(t) + \frac{1}{\lambda}f(t).$$

The transformation

$$u = U(\xi, t) - \frac{1}{\lambda}\varphi(t) + \frac{1}{\lambda}\int f(t)dt$$

and

$$\xi = z - \int[k\varphi(t) - \lambda\psi(t)]dt$$

reduces this equation to the ordinary heat conduction equation

$$\frac{\partial U}{\partial t} = \nu\lambda^2\frac{\partial^2 U}{\partial \xi^2}.$$

3°. Exact solutions to Eq. (2) in the case of $f(x, t) = 0$ take the form

$$w(x, y, t) = A(t)\exp(kx - \lambda y) + B(t)\exp(\beta kx - \beta\lambda y) + \psi_t'(t)x + ay, \qquad (19)$$

$$A(t) = C_1\exp[(\nu\lambda^2 - ak)t - \lambda\psi(t)],$$

$$B(t) = C_2\exp[(\nu\beta^2\lambda^2 - ak\beta)t - \beta\lambda\psi(t)],$$

where $\psi(t)$ is an arbitrary function, with C_1, C_2, a, k, β, and λ being arbitrary parameters.

Remark 4. Solutions (13), (18), and (19) can be generalized by using formula (12).

4°. Exact solutions to Eq. (2) in the case of $f(x, t) = 0$ take the form

$$w(x, y, t) = [C_1 e^{k_1(x - at)} + C_2 e^{k_2(x - at)}]E(x, t)e^{-\lambda y} + \frac{\partial}{\partial t}\int\varphi(x, t)dx + ay,$$

$$E(x, t) = \exp[\nu\lambda^2 t - \lambda\varphi(x, t)],$$

where $\varphi(x, t)$ is an arbitrary function, with C_1, C_2, a, k_1, k_2, and λ being arbitrary parameters.

5°. Exact solutions to Eq. (2) in the case of $f(x, t) = g(x)e^{\beta t}$ take the form

$$w(x, y, t) = \varphi(x, t)e^{\lambda y} + \psi(x, t)e^{-\lambda y} + \frac{1}{\lambda}\frac{\partial}{\partial t}\int\ln|\varphi(x, t)|dx - \nu\lambda x,$$

$$\psi(x, t) = -\frac{e^{\beta t}}{2\lambda^2\varphi(x, t)}\int g(x)dx, \quad \lambda = \pm\sqrt{\frac{\beta}{2\nu}},$$

where $\varphi(x, t)$ is an arbitrary function of two variables.

6°. Exact solutions to Eq. (2) in the case of $f(x, t) = ae^{\beta x - \gamma t}$ take the form

$$w(x, y, t) = \varphi(x, t)e^{\lambda y} + \psi(x, t)e^{\beta x - \lambda y} + \frac{1}{\lambda}\frac{\partial}{\partial t}\int \ln|\varphi(x, t)|\,dx - \nu\lambda x + \frac{2\nu\lambda^2 + \gamma}{\beta}\left[y + \frac{1}{\lambda}\ln|\varphi(x, t)|\right],$$

$$\psi(x, t) = -\frac{ae^{-\gamma t}}{2\beta\lambda^2\varphi(x, t)},$$

where $\varphi(x, t)$ is an arbitrary function of two variables and λ is an arbitrary constant.

8. Construction of approximate solutions to the boundary layer problems. Transformation (7) can be used for finding approximate solutions to problems of flows around smooth weakly deformed surfaces (differing only slightly from a plane). We consider steady-state problems. We assume that in the case of a flow around a surface, the following equation can be used

$$z = \psi(x, y).$$

We assume that a solution to the simpler problem with $\psi \equiv 0$ can be found and takes the form

$$u_k^\circ = u_k^\circ(x, y, z), \quad k = 1, 2, 3.$$

In this case, an approximate solution to the problem with $\psi \not\equiv 0$ can be constructed using the formulas

$$u_1 = u_1^\circ(x, y, z - \psi(x, y)), \quad u_2 = u_2^\circ(x, y, z - \psi(x, y)),$$

$$u_3 = u_3^\circ(x, y, z - \psi(x, y)) + u_1^\circ(x, y, z - \psi(x, y))\frac{\partial\psi}{\partial x} + u_2^\circ(x, y, z - \psi(x, y))\frac{\partial\psi}{\partial y}, \tag{20}$$

which are derived from (7) for $\varphi = -\varphi$. Because the equalities $u_k^\circ\big|_{z=0} = 0$ are fulfilled, approximate solution (20) satisfies the adhesion conditions on the flow around the surface, $u_k|_{z=\varphi(x,y)} = 0$. The functions u_k and u_k° have an identical asymptotic behavior as $z \longrightarrow \infty$ (i.e., the approximate solution is sewn to an inviscid solution in the flow core). If the function ψ and its partial derivatives ψ_x and ψ_y are zero for $x = 0$ and $y = 0$, then both the approximate solution u_k and the solution u_k° satisfy identical boundary conditions at $x = 0$ and $y = 0$.

Because the functions u_k exactly satisfy the boundary conditions at $z = \psi(x, y)$, it should be expected that they describe the flow near a surface better than the functions u_k° (because the functions u_k° do not satisfy any adhesion conditions on the surface) and lead to more exact values for the calculated drag coefficient.

It is convenient to choose solution (20) as the first approximation in using the iteration methods of solving the boundary layer problems [9]. Solution (20) can be used for testing the finite difference and other numerical methods of solving the boundary layer problems in flows past deformed surfaces [it is of importance that solution (20) is an exact solution to Eqs. (4)–(6) with an arbitrary function $\varphi = \varphi(x, y)$].

Remark 5. Although solution (20) is an exact solution to Eqs. (4)–(6), these equations themselves, in the case of a deformed surface, become approximate.

Example. The solution to the Blasius problem on a two-dimensional flow past a flat plate is described by formulas [1, 2]:

$$u_1^\circ = U_\infty\Phi'_\eta(\eta),$$
$$u_3^\circ = \frac{1}{2}\sqrt{\frac{\nu U_\infty}{x}}[\eta\Phi'_\eta(\eta) - \Phi(\eta)], \quad \eta = z\sqrt{\frac{U_\infty}{\nu x}}. \tag{21}$$

Here, respectively, x and z are the longitudinal and transverse coordinates, u_1° and u_3° are the longitudinal and transverse components of the fluid velocity, U_∞ is the fluid velocity far from the plate, and the function $\Phi = \Phi(\eta)$ is determined by solving the boundary value problem for the ordinary differential equation

$$\Phi'''_{\eta\eta\eta} + \frac{1}{2}\Phi\Phi''_{\eta\eta} = 0;$$

$$\Phi = \Phi'_\eta = 0 \quad \text{for} \quad \eta = 0;$$
$$\Phi \longrightarrow 1 \ \text{ as } \ \eta \longrightarrow \infty.$$

We construct an approximate solution to the problem on the two-dimensional flow past a weakly deformed plate with a surface $z = \psi(x)$ by using formulas (20) and (21) with $u_2 = u_2^\circ = 0$. As a result, we obtain

$$u_1 = U_\infty\Phi'_\zeta(\zeta), \quad \zeta = [z - \psi(x)]\sqrt{\frac{U_\infty}{\nu x}},$$

$$u_3 = \frac{1}{2}\sqrt{\frac{\nu U_\infty}{x}}[\zeta\Phi'_\zeta(\zeta) - \Phi(\zeta)] + U_\infty\Phi'_\zeta(\zeta)\psi'_x(x),$$

where the function $\Phi = \Phi(\zeta)$ is taken from the solution to the Blasius problem.

Remark 6. The method described can also be used for finding an approximate solution to the unsteady boundary layer problems on flows past weakly deformed surfaces with the initial conditions

$$u_1^\circ\big|_{t=0} = u_2^\circ\big|_{t=0} = 0, \quad u_3^\circ\big|_{t=0} = \omega(x, y)$$

and the geometrical conditions for the function φ used before.

ACKNOWLEDGMENTS

This study was carried out under the financial support of the Russian Foundation for Basic Research, projects no. 00-02-18033 and 00-03-32055.

REFERENCES

1. L. G. Loĭtsyanskiĭ, *Mechanics of Liquid and Gas* (Nauka, Moscow, 1973).
2. H. Schlichting, *Boundary Layer Theory* (McGraw-Hill, New York, 1968, 6th ed.; Nauka, Moscow, 1974).
3. L. I. Vereshchagina, Vestn. Leningr. Univ. **13** (3), 82 (1973).
4. Yu. N. Pavlovskiĭ, Zh. Vychisl. Mat. Mat. Fiz. **1**, 280 (1961).
5. L. V. Ovsiannikov, *Group Analysis of Differential Equations* (Nauka, Moscow, 1978; Academic, New York, 1982).
6. *CRC Handbook of Lie Group to Differential Equations*, Ed. by N. H. Ibragimov (CRC Press, Boca Raton, 1995), Vol. 2.
7. Z. P. Shul'man and B. M. Berkovskiĭ, *Boundary Layer of Non-Newtonian Liquids* (Nauka i Tekhnika, Minsk, 1966).
8. A. M. Kutepov, A. D. Polyanin, Z. D. Zapryanov, *et al.*, *Chemical Hydrodynamics* (Kvantum, Moscow, 1996).
9. Yu. D. Shevelev, *Three-Dimensional Problems of Laminar Boundary Layer Theory* (Nauka, Moscow, 1977).
10. V. A. Galaktionov and S. A. Posashkov, Zh. Vychisl. Mat. Mat. Fiz. **29**, 497 (1989).
11. A. D. Polyanin, A. I. Zhurov, and A. V. Vyaz'min, Teor. Osn. Khim. Tekn. **34**, 451 (2000).
12. V. F. Zaĭtsev and A. D. Polyanin, *Handbook on Partial Differential Equations: Exact Solutions* (Moscow, 1996).

Translated by V. Bukhanov